ESPOO 2004
VTT PUBLICATIONS 536

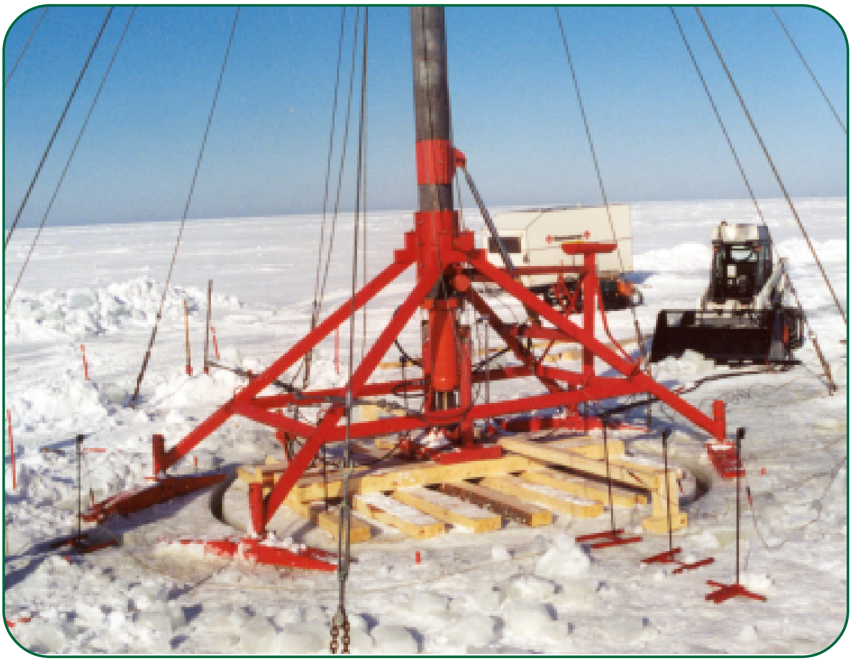

Jaakko Heinonen

Constitutive Modeling of Ice Rubble in First-Year Ridge Keel

VTT PUBLICATIONS 536

Constitutive Modeling of Ice Rubble in First-Year Ridge Keel

Jaakko Heinonen
VTT Building and Transport

*Dissertation for the degree of Doctor of Technology
to be presented with due permission for public examination and debate
in Auditorium E at Helsinki University of Technology (Espoo, Finland)
on the 28th of June, 2004, at 12 o´clock noon.*

ISBN 951–38–6390–5 (soft back ed.)
ISSN 1235–0621 (soft back ed.)

ISBN 951–38–6391–3 (URL: http://www.vtt.fi/inf/pdf/)
ISSN 1455–0849 (URL: http://www.vtt.fi/inf/pdf/)

JULKAISIJA – UTGIVARE – PUBLISHER

VTT, Vuorimiehentie 5, PL 2000, 02044 VTT
puh. vaihde (09) 4561, faksi (09) 456 4374

VTT, Bergsmansvägen 5, PB 2000, 02044 VTT
tel. växel (09) 4561, fax (09) 456 4374

VTT Technical Research Centre of Finland, Vuorimiehentie 5, P.O.Box 2000, FIN–02044 VTT, Finland
phone internat. + 358 9 4561, fax + 358 9 456 4374

VTT Rakennus- ja yhdyskuntatekniikka, Kemistintie 3, PL 1805, 02044 VTT
puh. vaihde (09) 4561, faksi (09) 456 7007

VTT Bygg och transport, Kemistvägen 3, PB 1805, 02044 VTT
tel. växel (09) 4561, fax (09) 456 7007

VTT Building and Transport, Kemistintie 3, P.O.Box 1805, FIN–02044 VTT, Finland
phone internat. + 358 9 4561, fax + 358 9 456 7007

Otamedia Oy, Espoo 2004

Heinonen, Jaakko. Constitutive Modeling of Ice Rubble in First-Year Ridge Keel. Espoo 2004. VTT Publications 536. 142 p.

Keywords sea ice, ice ridges, ice rubbles, ridge keels, loading tests, punch shear tests, modeling, material models

Abstract

In-situ full-scale loading tests were conducted in the Northern Gulf of Bothnia in order to measure the ridge keel mechanical properties. Altogether 33 loading tests in full-scale were conducted during five winters (1998–2003). 12 of them were punch shear tests, in which a circular plate of the consolidated layer was punched downwards to break the rubble underneath. In all ridge loading tests, the sail was first removed and the consolidated layer was cut free from the surrounding solid ice field to allow well-defined boundary conditions. Maximum loads in the punch shear tests varied from 74 kN to 1.1 MN. The diameter of the platen varied between 2.5 and 4.7 m. The average keel depth varied from 3.0 to 6.4 m while the corresponding effective thickness of rubble under the platen varied from 2.2 to 5.0 m.

A continuum material model for ice rubble was developed and implemented into commercial finite element software ABAQUS/Standard. The constitutive law was written in similar form to that used in the plasticity theory based on the strain decomposition into elastic and plastic parts. The shear-cap yield surface with evolution laws both for cap hardening and cohesive softening describe also the compaction phenomenon in addition to shear failure.

An axisymmetric finite element model was created to simulate punch shear tests. Time history analysis in finite element method observes progressive failure through the keel occurring non-simultaneous global keel failure. Good agreement in the load-displacement relationship was achieved by calibrating the material parameters to fit the full-scale measurements. The admissible combination of cohesion and the friction angle was evaluated by parametric studies to simulate the measured maximum force correctly. The failure progression in the keel and the relation between the failure modes (compaction and shear) depended strongly on the friction angle. Increased friction resulted in more dilatation at the region of shear failure and more compaction at the region of cap failure. Due to the volumetric expansion during shear failure, a slightly inclined shear failure zone created finally a conical plug punched through the keel.

Preface

The research reported in this thesis has been carried out at Laboratory for Mechanics of Materials in Helsinki University of Technology within two EU-sponsored projects. The first one, Validation on Low Level Ice Forces on Coastal Structures (LOLEIF) was carried through from 1997 to 2000 in the framework of the EU-sponsored Marine Science and Technology (MAST-III) Programme under contract no. MAS3-CT97-0078. The second one, Measurements on Structures in Ice (STRICE) was undertaken from 2001 to 2003 within the Workprogramme of the 5th FP in the Area "Energy, Environment and Sustainable Development" under Project No. EVG1-2000-22019.

I would like to acknowledge my supervisor Prof. Mauri Määttänen. It has been a pleasure to study icemechanics encouraged by his great experience.

I would also like to express my gratitude to all my colleagues in VTT Building and Transport for their support. Especially, I would like to thank Dr. Matti Kokkala, Dr. Alpo Ranta-Maunus and Lic.Sc. Heli Koukkari for supporting the finalization of thesis and Dr. Tuomo Kärnä and Mr. Kari Kolari for all helpful comments and support.

I am also thankful to all my colleagues in the Laboratory for Mechanics of Materials in Helsinki University of Technology for supporting me in my work. Especially the experimental tests would not have been possible to accomplish without their extensive amount of work. I would like to acknowledge Prof. Jukka Tuhkuri and Dr. Kari Santaoja for their constructive comments on my thesis.

I am grateful to the preliminary reviewers of the thesis, Prof. (emeritus) Martti Mikkola from Helsinki University of Technology and Dr. Ahmed Derradji-Aouat from National Research Council in Canada, for their productive comments.

I would like to thank all colleagues in LOLEIF and STRICE group including advisors for fruitful co-operation. A special thanks to co-ordinators Dr. Joachim Schwarz and Dr. Walter L. Kühnlein from Hamburg Ship Model Basin (HSVA) as

well as to all companies attending to LOLEIF and STRICE who admitted to publish the experimental data.

I would like to thank Dr. Knut V. Høyland for his help in field tests and his comments on my work.

Finnish Academy is acknowledged for funding my studies in the graduate school.

Mrs. Adelaide Lönnberg is acknowledged for reviewing the English language.

Finally, I would like to express my gratitude to my wife Tove and sons Eelis and Oskar encouraging me during my work.

Table of contents

Nomenclature

Scalar quantities

a	platen radius
a	fitting parameter
a, b	coefficients in ridge load model
a_T, b, c_1, s	constant in Sinha’s model
c	cohesion
d	average grain diameter
d_1	dimension of the average grain diameter
d	platen diameter
d	cohesion
d_0	initial cohesion
$\tilde{d}$	physical value for cohesion
e	void ratio
e_0	initial void ratio
f	yield function
f_s, f_c	shear and cap yield function
g	gravitation acceleration
g	plastic flow potential function
h	effective keel thickness
h_{cl}	consolidated layer thickness
h_{cut}	cut depth
h_i	ice thickness
h_k	keel thickness
h_s	sail thickness
h_{total}	total keel thickness
k	fraction of submerged volume
n	stress exponent in Norton’s law
p	hydrostatic pressure, first stress invariant
p_a	limit pressure between cap and shear failure part
p_b	hydrostatic pressure strength
p_0	initial hydrostatic pressure strength

q	nominal pressure
q	von Mises equivalent stress, second deviatoric stress invariant
r	third deviatoric stress invariant
r, θ	co-ordinate
t	time
u	pore pressure
u_z	platen displacement in vertical direction
x	variable in least square fitting
x, y and z	co-ordinate

D_e	effective structure width
E	elastic modulus (Young's modulus)
$F_{\max}$	maximum force
$F_{\max}^{\mathrm{c}}$	maximum force in coarse mesh
FB	freeboard
G	shearing modulus
J	relative volume
K	bulk modulus
L_0, L_1	transducer location in keel
R	ratio of consolidation
R	cap shape parameter
S	surface area
V	volume (at current state)
V_0	volume at original state
V_c	volume of cavities
V_s	volume of solid material
W^{p}	mechanical dissipation work
$W_{\mathrm{dev}}^{\mathrm{p}}$	deviatoric part of mechanical dissipation work
$W_{\mathrm{vol}}^{\mathrm{p}}$	volumetric part of mechanical dissipation work

α	algorithm parameter
α	angle for conical failure mode
β	friction angle

$\tilde{\beta}$	physical value for friction angle
Δu	rubble compaction
ε_e	elastic strain
ε_d	delayed elastic strain
ε_v	viscoplastic strain
ε_∞	softening parameter
$\dot{\varepsilon}_0$	viscoplastic strain rate parameter
ε^{p}_{dev}	equivalent deviatoric plastic strain
ε^{p}_{vol}	volumetric plastic strain
ε_{vol}	volumetric strain (dilatation)
φ	friction angle
κ	hardening parameter
λ	plastic multiplier
λ	material parameter
η	macro porosity of rubble
η_k	keel porosity
η_r	rubble porosity
η_s	sail porosity
ρ_i	ice density
ρ_w	water density
ρ_r	apparent rubble density
θ	angle
σ_n	normal stress on failure plane
σ_p	compressive strength of ice rubble in plain strain
σ_1	unit stress in Norton's law
σ_1, σ_2, σ_3	principal stresses
τ	shear stress or strength
ν	Poisson value

Tensor quantities

b_i	body force
C_{ijkl}	constitutive tensor (generally)
C_{ijkl}	elastic constitutive tensor

C_{ijkl}^{ep}	elastic-plastic constitutive tensor
D_{ij}	rate of deformation tensor
e_{ij}	deviatoric strain tensor
q_i	internal forces
h_i	hardening function
s_{ij}	deviatoric stress tensor
t_i	traction force
u_i	displacement
v_i	velocity

α_i	internal state variables
δ_{ij}	kronecker delta
ε_{ij}	strain tensor
$\varepsilon_{ij}^{\mathrm{e}}$	elastic strain tensor
$\varepsilon_{ij}^{\mathrm{ie}}$	inelastic strain tensor
$\varepsilon_{ij}^{\mathrm{d}}$	damage strain tensor
$\varepsilon_{ij}^{\mathrm{p}}$	plastic strain tensor
γ_i	buoyant volume force
σ_{ij}	stress tensor
σ'_{ij}	effective stress tensor
τ_{ij}	Kirchhoff's stress tensor

Vector and matrix notations

$\mathbf{C}$	constitutive matrix
$\mathbf{F}$	nodal force vector
$\mathbf{f}^{\mathrm{ext}}$, $\mathbf{f}^{\mathrm{int}}$	external and internal part of nodal force vector
$\mathbf{B}$	kinematic matrix
$\mathbf{K}$	stiffness matrix
$\mathbf{N}$	shape function matrix
$\mathbf{u}$	nodal displacement vector
$\tilde{\mathbf{u}}$	approximation of nodal displacement vector

1 Introduction

1.1 Problem description

Ridges are common ice features in Northern seas. They are formed when sea ice is compressed or sheared under the action of wind and currents. Ridges are constantly shifting due to wind and sea currents, causing remarkable loads against off-shore structures during interaction. A ridge contains a large number of ice pieces of varying sizes and shapes that are piled arbitrarily. Rubble above the water line is called a sail and the rubble below the water line is called a keel. Between them, close to the waterline, is the re-frozen solid ice zone called a consolidated layer.

First-year ridges play an important role in many ice-related processes. First-year ridges are often a key consideration from an engineering perspective. For example, in the Gulf of Bothnia and Northumberland Strait, first-year ridges control the design load levels for offshore structures. Also, ridges impede significantly the navigation in ice-covered regions and first-year ridges can also scour the sea floor in shallow waters, which has significant consequences for the design of pipelines and other sub-sea facilities.

Ice rubble together with the consolidated ice layer is a complicated structure and its mechanical behavior is not well understood. The ridge loads cannot be predicted reliably because general constitutive laws are not developed. Also, the mechanical properties of the ridge keel and the consolidated layer have been estimated according to laboratory scale-model test results, because full-scale data has not been available. Existing theoretical models to predict ridge ice loads are based on soil mechanics and assume simultaneous failure surface activation. Usually those models, like the Mohr-Coulomb failure criterion, assume that particles in rubble are rigid and that the rubble fails only by shearing. However, for instance in ridge-structure interaction, rubble fails by compacting at the front of the structure in addition to shear failure close to the edge.

1.2 Objectives and scope of the work

The objectives were first to measure mechanical properties in full-scale for ridge keel and consolidated layer . A new test set-up was designed and manufactured for testing ridges at Hailuoto in the Gulf of Bothnia, Finland. Testing method and test results are described in Ch. 3 and 4.

The second target was to develop a numerical model capable of observing the progressive development of failure surfaces in the ridge keel. Submerged ice rubble in the ridge keel was modeled by a nonlinear continuum model described in Ch 5.

The finite element method with a new material model was used to simulate the punch shear test. The model implementation into finite element software ABAQUS/Standard is described in Ch. 6.

Full-scale test data was used to calibrate the model. Material parameters were evaluated by parametric studies by adjusting the load-displacement curves in the punch tests. Numerical simulations, documented in Ch. 7, included also studies of keel failure mechanisms.

Taken into account the restrictions of a continuum model, the developed material model can be used in a finite element simulation of a ridge-structure interaction by applying true geometry for both the ridge and the structure, which is the final target of the development work.

This work has been undertaken within the EU-sponsored projects LOLEIF from 1997 to 2000 and STRICE from 2001 to 2003.

2 Review of ice properties and ridges

2.1 Mechanical behavior of sea ice

Sea ice, which is composed mostly of secondary ice, is not isotropic due to its columnar crystal structure. However, it is interpreted in many engineering approaches as transversely isotropic (orthotropic), having the same properties in all directions in the horizontal plane because the c-axes are randomly distributed in that plane. The mechanical behavior in the horizontal plane differs from that in the vertical orientation. Due to the different crystallographic layers and the temperature gradient in the vertical direction, there exists also a spatial dependency on properties.

The mechanical properties of sea ice depend on several factors. The most important are

- grain size and crystallographic orientation
- salinity and porosity
- loading rate
- temperature

One could also pay attention to the geometric scale effect and boundary conditions, such as confinement applied during loading.

The deformation, failure mechanisms and strength of ice are considerably affected by the strain rate. Typically, the strain rate is classified into the following ranges: ductile, transitional or brittle. Depending on the loading conditions, the ice can be interpreted either by continuum behavior describing elastic and ductile deformations or by fracture behavior characterizing brittle processes in crack formation.

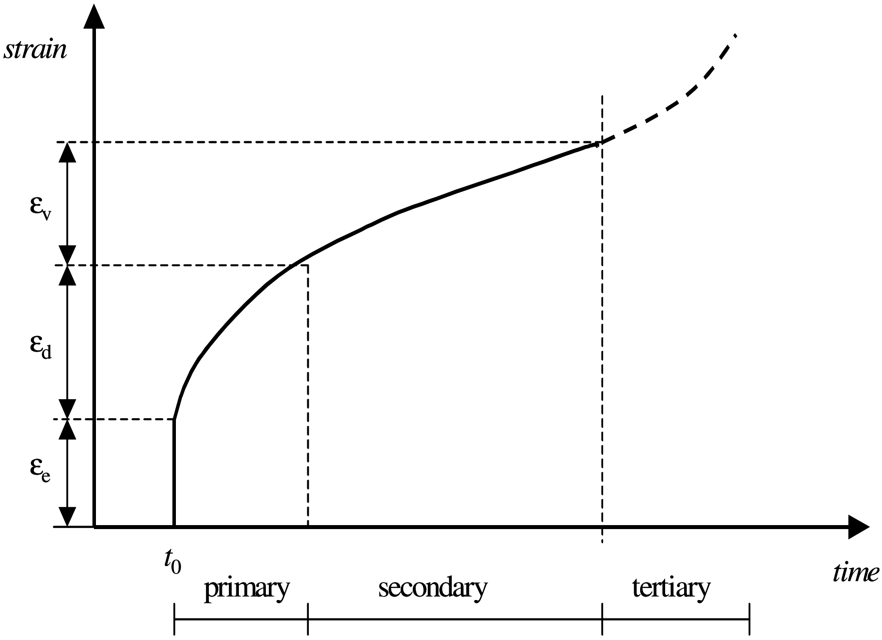

Figure 2.1. A typical strain history curve for ice in uniaxial loading. A constant stress is applied at time t_0.

Time-dependent deformation is divided into four stages: instantaneous deformation, primary creep deformation (transient), secondary creep deformation (steady state) and a tertiary stage resulting rapidly in failure (Fig. 2.1). The deformations in continuum models are often modeled by Sinha's model (1979) based on the strain decomposition. The model represents time-dependent deformation mechanisms containing both viscoelastic (primary creep) and viscoplastic (secondary creep) strain terms in addition to the elastic deformation. The model is developed from studies in uniaxial loading.

$$\varepsilon = \varepsilon_e + \varepsilon_d + \varepsilon_v \tag{2.1}$$

The elastic strain is described by Hooke´s law $\varepsilon_e = \sigma / E$. The other terms are time-dependent. The delayed elastic strain ε_d describes viscoelastic deformation for pure randomly oriented ice that has no brine inclusions or cracks. It is expressed by the stress σ and time t.

$$\varepsilon_{\mathrm{d}} = c_1 \frac{d_1}{d}\left(\frac{\sigma}{E}\right)^s \left\{1 - \exp[-(a_{\mathrm{T}}t)^b]\right\} \quad \textbf{(2.2)}$$

where a_{T}, b, c_1 and s are constants, d is the average grain diameter, and d_1 is the unit of the grain diameter. E is the elastic modulus. The delayed elastic deformation is recoverable. The visco-plastic strain describing the secondary creep is given in the rate form by Norton´s law

$$\dot{\varepsilon}_{\mathrm{v}} = \dot{\varepsilon}_0 \left(\frac{\sigma}{\sigma_1}\right)^n \quad \textbf{(2.3)}$$

where $\dot{\varepsilon}_0$ is the viscoplastic strain rate for the unit stress σ_1. The stress exponent n is normally equal to 3. The viscoplastic strain describes permanent deformation. The parameters a_{T}, $\dot{\varepsilon}_0$ and E in the equations above are temperature dependent. The same models are valid for sea ice with brine inclusions, but the parameters need to be modified (Sanderson, 1988).

Fig. 2.2 demonstrates the relation between the stress and strain according to Sinha's model in uniaxial loading. Linearly increasing stress up to 5 MPa is applied with different loading rates. The model parameters are taken from Sinha (1979), but the elastic modulus was reduced to 1.0 GPa to correspond better with field conditions (Heinonen et al. 2000b). The effect of the time dependent deformation in the total strain is approximately 10% while the load build-up time is 10 s. The stress-strain relationship is still rather linear. If the load build-up time is 60 s, the total strain is 20% higher than the elastic strain. Therefore, when studying the mechanical behavior of ice rubble the load build-up time should be below 60 s to avoid significant time dependent deformations. These results depend strongly on the grain size (diameter), which was chosen to be 3 mm as this corresponds to granular ice. If the grain size is larger, the effect of viscous deformations becomes smaller. This corresponds better to sea ice conditions, which comprise mostly columnar ice with larger grains.

Beltaos (2002) evaluated with Sinha's model that the creep strain for solid ice would be about 10% of the elastic strain during uniaxial loading for 5 seconds. The corresponding percentage of creep strain for 8 min loading is 40%.

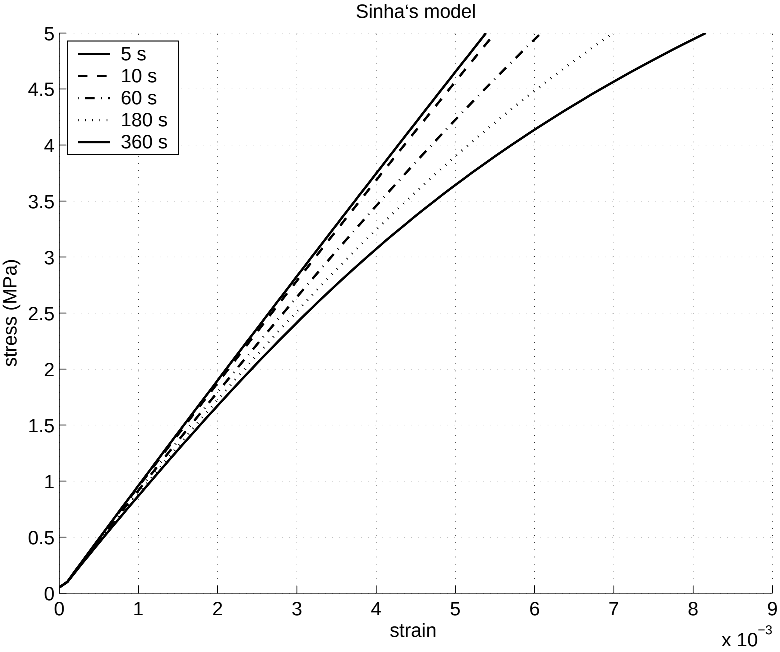

Figure 2.2. Stress-strain curves in uniaxial loading with different load build-up times according to Sinha's model.

Ice behaves as a brittle material if the applied stress is high enough or is applied for long enough. Formation of the first cracks depends mainly on the delayed elastic strain. The critical value of ε_d has been studied in the laboratory and can be used to define the loading conditions resulting in crack formation. Transition to brittle behavior is demonstrated in Fig. 2.3 characterizing typical columnar grained ice (S2) (Sanderson, 1988). Similar plots for crack formation can also be achieved for different sea ice conditions (salinity, grain size, temperature).

Although, the mechanical properties of solid ice depend strongly on several factors, it is not clear how strongly these factors come into play when ice blocks are piled into rubble.

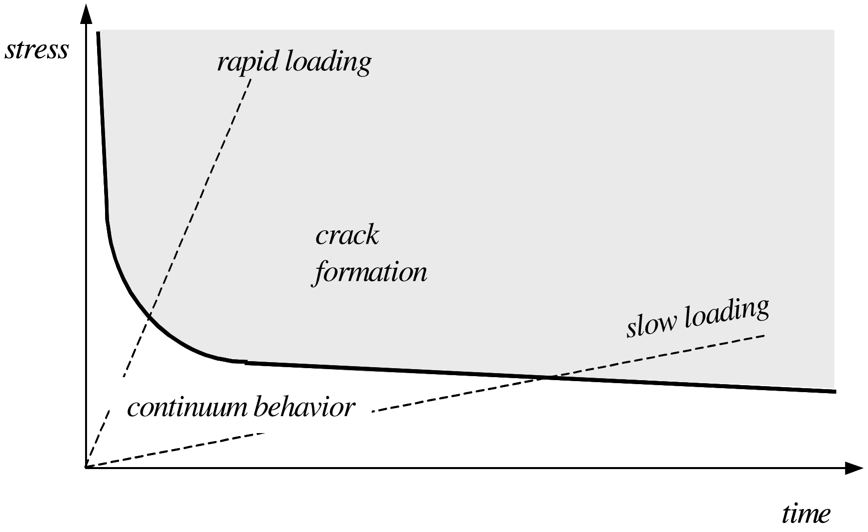

Figure 2.3. Stress-time map indicating regions for continuum behavior and crack formation according to Sanderson (1988).

2.2 First-year ice ridge

2.2.1 Ridge formation

First-year ice ridges are common ice features in Northern seas, for example in the Baltic Sea and the Gulf of Bothnia. Ridges are formed when level ice areas are compressed and sheared against each other due to environmental driving forces such sea currents and wind. A compression ridge is formed when two large ice floes or ice fields collide to each other. The ice field might split into two parts before or during the compression process. Rubble is a result of crushing and flexural failure during the ridge formation process. A compression ridge is often highly irregular, both in direction and in vertical height. A shear ridge is normally very straight, because separate ice fields move laterally in opposite directions. Rubble formed this way contains smaller ice blocks than in the compression ridge. Rafting is a process during which an ice plate overrides or underrides another ice plate. Finger-rafting with alternating upthrust and downthrust is also commonly observed. (Sanderson, 1988).

Usually the first-year ice ridge is formed by a combination of these modes. In the Gulf of Bothnia, the ice ridge usually contains some layers of rafted ice with rubble. Ice ridge formation is, however, quite poorly known. Laboratory tests support field observations that a ridge is first formed by rafting, which turns to ridging when the ice fields are rafted over a long enough distance (Tuhkuri et al., 1999). Hopkins et al. (1999) simulated with a discrete element method possible ridging and rafting processes when two ice sheets were pushed together. The ice sheet thickness and the thickness inhomogeneity are important factors controlling which process is predominating, whether ridging or rafting. Increasing the thickness inhomogeneity raises the probability of ridging, while homogenous sheets have a high probability of rafting.

Ridges are often found in the zone between land fast ice and drift ice. Ridges or rubble piles are also found in front of large structures like lighthouses or bridge piers. Generally, ridges are clearly observed from the ice field, because they are usually long and curvilinear (Fig. 2.4). However, large partially grounded ridge fields near the shore can also exist. In that case the field can be several hundred meters or several kilometers wide and it is impossible to say where the ridge line goes.

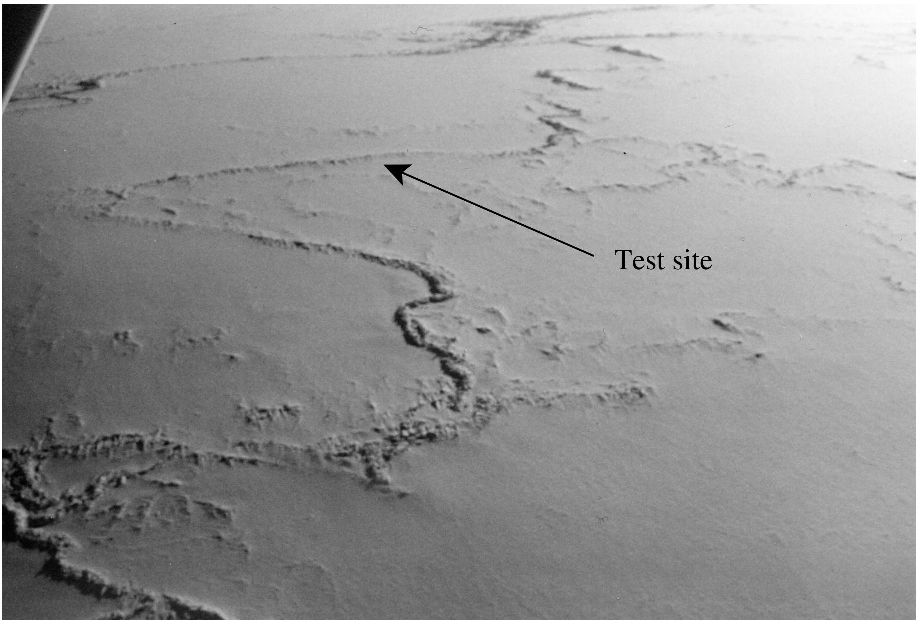

Figure 2.4. Aerial photograph of a ridge field with one test site outside Marjaniemi, Gulf of Bothnia (Feb. 2000).

2.2.2 Internal structure of ice ridge

The ridge contains a large number of ice pieces of varying sizes and shapes that are piled arbitrarily. Due to the hydrostatic equilibrium, the rubble above the water line (the sail) has a volume of about one tenth of the rubble below the water line (the keel). Between the sail and keel, close to the waterline, is the re-frozen solid ice zone called the consolidated layer as shown in Fig. 2.5.

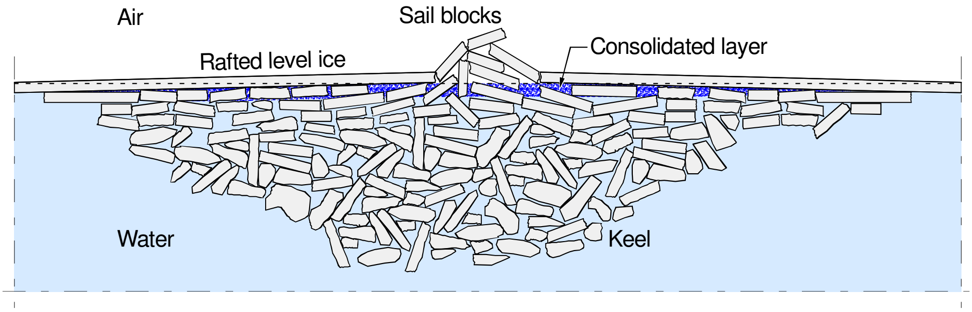

Figure 2.5. Principal cross section sketch of an ice ridge (Jensen et al., 2001)

Cavities in the rubble of the keel are filled with water and slush, but in the sail they contain snow and air. Hence the ridge is a porous feature. Once a ridge is formed it starts to freeze, because the average air temperature in winter is well below the freezing point of water. The freezing zone expands downwards and ice blocks freeze together with the level ice layer or rafted layers, creating the consolidated layer which also is porous. The voids contain mainly air in the fully consolidated part. Beneath the fully consolidated layer in the freezing zone the rubble is partially consolidated. Due to incomplete freezing, voids in the partially consolidated region contain water.

The dimensions, shapes and size distribution of the ice blocks determine the texture of the rubble. The initial ice condition, before the ridge was formed, is an important indicator. The ice block thickness is about the same as the level ice thickness when the ridge was formed. The dimensions in the two other directions are determined by the failure process (bending, crushing, shearing etc.). The snow thickness above the ice indicates how much slush is present in the pores. Environmental conditions around the ridge such as the ambient temperature and the wind, as well as the snow cover, play a major role in heat transfer and consolidation. In the underwater part, the presence of currents causes shape modification of the ice blocks, deteriorating the rubble through thermal and mechanical erosion.

The main dimensions of a ridge are defined in Fig. 2.6 in which h_k is the thickness of the keel and h_s is the thickness of the sail. Both of them are measured from the water-level. h_i is the level ice thickness and and h_{cl} is the consolidated layer thickness. *FB* is the freeboard.

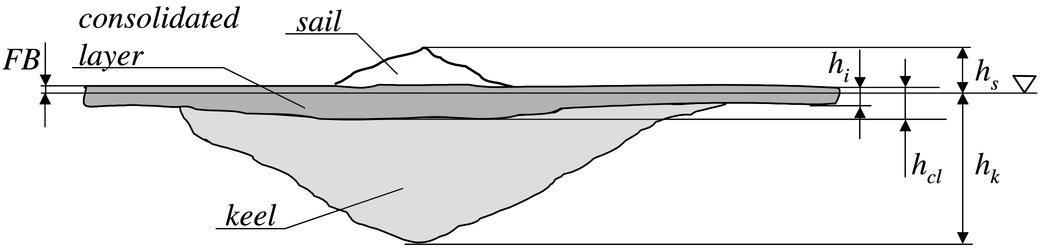

Figure 2.6. Main dimensions of a ridge.

The thickness of the keel can be predicted when the ratio between the keel depth h_k and the sail height h_s as well as the sail height is known. Timco and Burden (1997) presented the following ratio for first-year ridges in which the cross-section was approximated with an ideal triangular shape.

$$\frac{h_k}{h_s} = 4.4 \tag{2.4}$$

According to investigations in the Baltic Sea (Kankaanpää, 1998), the keel depth is

$$h_k = 6.35 h_s - 0.02 \text{ m} \tag{2.5}$$

Characterizing the consolidated layer, one can define the ratio *R* between the consolidated layer thickness and the level ice thickness as

$$R = \frac{h_{cl}}{h_i} \tag{2.6}$$

Høyland (2002) observed that the consolidated layer thickness measured by thermistor strings was lower than found by drilling. Temperature measurements in Spitsbergen and Marjaniemi in the Gulf of Bothnia indicated $R = 1.39 - 1.61$ while the drillings gave $R = 1.68 - 1.85$. The most important reason for the difference was that the partially consolidated ice was interpreted as solid ice in the drilling measurements. However, the growth of the consolidated layer did not depend on the investigation method. Høyland (2002) also summarized several results from the literature and concluded that the ratio R is between 1.2 - 1.9.

2.2.3 Porosity

The macroporosity of ice rubble η is defined as a volume of cavities V_c between the solid ice blocks compared with the total volume of rubble V. The cavities contain non-solid materials, like water, slush, snow and air. Another similar quantity is the void ratio e defining the ratio between the volume of voids and the volume of solid material V_s.

$$\eta = \frac{V_c}{V} \quad ; \qquad e = \frac{V_c}{V_s} \tag{2.7}$$

The following relationships exist between porosity and the void ratio:

$$\eta = \frac{e}{1+e} \quad ; \qquad e = \frac{\eta}{1-\eta} \tag{2.8}$$

The average keel porosity η_k is measured for the whole keel volume corresponding to the keel thickness h_k. Also, the average sail porosity η_s corresponds to the sail thickness h_s. Porosity of the unconsolidated rubble η_r is measured for the volume of the keel which is below the consolidated layer.

Porosity depends on several variables, like the internal structure of the material and the stress state. Some basic observations can be made by studying particulate media assembled by spherical particles. Porosity is independent of particle size when the individual particles are uniform. The porosity of the most open packing - cubic packing - is 47.64%, in which all particles have six contact points. The closest packing of spherical particles has a porosity of 25.95% and 12 contact points. The product of the number of contact points and the porosity is approximately equal to 3. If the particle size varies, the finer components can fill up interstices between the larger particles. Therefore, a multi-component mixture usually has a smaller porosity compared to one component media. (Harr, 1977).

Similar observations are made for ice rubble. The shape of an individual ice block is arbitrary, but the block thickness (thickness of original level ice) is usually much less than the width. Therefore, both the shape and size of ice blocks in rubble vary. Due to the complicated ridge formation process, the blocks are not necessarily oriented randomly.

Porosity also depends on the internal stress state. The weight of the sail is balanced by hydrostatic forces in the consolidated layer with the keel underneath. The buoyancy in the keel causes hydrostatic pressure, compressing the rubble and resulting in denser packing. Theoretically the rubble porosity is not constant in the vertical direction, because the total force distribution due to gravitation in the sail and buoyancy in the keel are not constant.

Porosity measurements are usually made by drilling, which is also used to determine the consolidated layer thickness. To get a general figure of the line-like ridge, several drills for each cross section must be done close to each other. During manual drilling each drop is registered as void. Average porosity is usually around 30 - 35% in the keel, while sail porosity is a bit less, around 20 - 27% (values from the Baltic Sea by Kankaanpää, 1998). Similar values for keel porosity are presented by Leppäranta and Hakala (1992): average 29% and Høyland et. al. (2000): average 38%. A relationship between the sail porosity and the keel porosity was presented by Timco and Burden (1997).

$$\eta_k = 0.14 + 0.73\eta_s \qquad \textbf{(2.9)}$$

It should be noted that the average porosity in the keel having a contribution from both consolidated and unconsolidated rubble is less than in the rubble, because the consolidated layer has much lower porosity. Høyland measured the following relation between rubble porosity and average keel porosity (Heinonen et al. 2000(a)).

$$\eta_r \approx \eta_k + 0.04 \qquad \textbf{(2.10)}$$

Kankaanpää (1998) observed that the blocks are generally larger in the keel than in the sail. This might be one reason for the difference in the porosity values. In the keel Määttänen (1999) observed during diving that the largest floes are lowermost. During the ridging process small ice floes are easier to dodge upwards.

2.2.4 Consolidation

Once the ridge has been formed, the consolidation of rubble proceeds. Ice blocks freeze together with the level ice (if it exists in the ridge) or with rafted ice layers. The internal texture of re-frozen ice is different to that of level ice. The internal structure (basal planes and c-axes) of the ice is usually different than before the ridge was formed, because broken ice blocks have been reoriented during the ridge building process. In addition, macro-scale voids are initiated during freezing. The voids contain mainly water and slush in the partially re-frozen zone. When the freezing continues, the water in the voids freezes, reducing the porosity. As the voids freeze solid, volume expansion causes cracking and further increases the inhomogeneity. Voids in the fully re-frozen part contain mainly air. Due to the variation of environmental conditions during winter, the consolidated layer thickness, as well as the internal structure, has a strong seasonal dependency.

Rogachko and Kärnä (1999) observed in experiments on a freshwater lake that the compressive strength of artificially built re-frozen ice in small-scale tests with equal porosity was approximately the same as in natural level ice. Increase of porosity decreased the compressive strength. However, they observed that in medium scale indentation tests, the strength of re-frozen ice with zero porosity was 19% lower than in the corresponding level ice. Some variations in results were explained by the difference in ice temperature. Rogachko et al. (1997) studied the effect of void shape and observed in uniaxial compression tests that strength decreased by 30% while porosity increased from 2% to 16% in the case of spherical voids. The corresponding strength reduction was 64% in the case of irregular voids.

Yasunaga et al. (2001) also performed uniaxial compression tests for a consolidated layer prepared in an ice tank from saline water. They observed that ice blocks in artificially constructed re-frozen ice were randomly oriented and that the crystallographic axes had no clear direction resulting in lower macroscopic anisotropy, which was defined as a ratio between the strengths in the vertical and horizontal directions (σ_v/σ_h). However, how voids affect the failure mechanism is not well studied for ice. Constitutive models for sea ice could be applied also for re-frozen ice to get an approximate ice load against a structure.

2.2.5 Mechanical properties of ice rubble

Several scale-model tests for ice rubble mechanical properties have been conducted in laboratory conditions. Both naturally broken ice and ice-machine ice have been used as a source for the rubble. However, the texture of the rubble has been artificial. None of the reported scale model test data has rubble that was formed the same way as in nature. Only recently have Tuhkuri et al. (1999) succeeded in produce rubble in an ice tank with a natural compression/shear mechanism. However, in that context no rubble mechanical properties were measured.

In all published small-scale experiments, cohesive-frictional material behavior describing the shear strength τ is modeled by a Mohr-Coulomb failure criterion ($|\tau| = c - \sigma\tan\varphi$, in which c is the cohesion and φ is the friction angle. σ is the normal stress affecting on the shear failure plane).

Prodanovic (1979) measured saline unconsolidated ice rubble properties with direct shear tests. He reported values of 0.25 and 0.56 kPa for cohesion as well as 47° and 53° for the friction angle corresponding to ice rubble piece thicknesses of 19 mm and 38 mm. The larger confinement pressure indicated an increase of the effective shear modulus due to densely packed ice rubble. Also, with high confinement the rubble collapsed, represented by a sudden drop in shear stress after the peak value, which could be interpreted as a strain-softening feature.

Ettema and Urroz (1989) described the significance of internal friction consisting of contact friction between ice blocks and interlocking phenomena under rubble deformations. They studied the reasons for why earlier reported values for internal friction are as high, for example, as those reported by Prodanovic (1979). Their observation was that the internal stress state due to the buoyancy load causes confinement, which increases the frictional part of the strength even if the external confinement force is zero. This results in lower friction angles. They also proposed that the cohesion of ice rubble depends on the stress state (confinement) resulting in an effective friction angle, which is less than the friction angle associated with an apparent Mohr-Coulomb criterion.

Weiss et al. (1981) measured unconsolidated rubble mechanical properties on a scale of 1:10 with a shear box. Ice was formed from highly saline water (5 - 6%). They reported cohesion from 1.7 to 4.1 kPa and friction angle from 11° to 34°. Cohesive strength was proportional to the ice rubble piece thickness. Relative cohesion described by cohesion over the thickness was 16 ± 8 kPa/m. Experiments conducted in Russia indicate similar results for relative cohesion (Kärnä (Ed.) 1997).

Sayed et al. (1992) observed in shear box tests with plane strain conditions that deformations in rubble are non-recoverable. However, rubble did not have time to consolidate between sample preparation and testing. Also, the strain rate effect or initial porosity had no influence on the stress-strain relation. They also measured the relation between the hydrostatic pressure and volumetric strain describing the compressibility of rubble. Therefore, the porosity of rubble decreases due to an increase of hydrostatic pressure.

Azarnejad and Brown (2001) observed in small-scale punch tests that the friction angle increased according to the loading rate, but it was assumed that only friction describes the rubble strength (cohesion was zero). They also concluded that better theories need to be developed for interpreting the results at higher rates. In their small-scale punch tests, ice rubble was obtained from ice machines, and the tank was filled with fresh water. Aging describes the time between the rubble formation and the loading test. Already one hour of aging increased the shear strength significantly due to freeze bonding between ice blocks. With a small loading rate, the friction angle was 37° for zero-aged rubble. With 1-h aging the corresponding friction was approximately 47°. Large variation of the friction angle was determined depending on the loading rate, aging and rubble thickness. Lemee and Brown (2002) observed from the same measurements that if the loading rate is high, the hydrodynamic loads due to water inside the voids has more contribution causing different type of failure mechanism and load pattern. During slow loading, the water inside the voids in the underwater part of the rubble escapes freely.

Small-scale punch shear tests in an ice basin have been carried out by Jensen et al. (2001). Visual observation with an underwater camera in a 2-dimensional punch test (plain strain) indicated that the failure surface inclined significantly (40°) from the vertical direction. During vertical loading the floating ridge also deformed by bending in addition to shear. In some cases the bending deformation initiated the failure.

In addition to the LOLEIF and STRICE projects, full-scale tests of pressure ridge mechanical properties have only been carried out a few times: notably by Leppäranta and Hakala, (1989) and (1992), Croasdale et al. (1997) and Smirnov et al. (1999). With limited resources, loading systems have been underpowered or too slow to simulate correctly real ice rubble/structure interaction. No instrumentation to monitor what is happening inside the rubble has been reported. Leppäranta and Hakala (1992) reported cohesion from 1.5 kPa to over 4.0 kPa, which is comparable to the results of small-scale measurements by Weiss et al. (1981). However, the values better describe shear strength than cohesion, because frictional behavior was not taken into account. Parallel to the LOLEIF and STRICE -projects, two collaborative projects involving Russian, Canadian and US groups were conducted to gather in-situ strengths of first year ridges (Croasdale et al., 1997). The testing methods were based on a review of techniques conducted in Canada in 1996 (Bruneau et al., 1998). The test programs were repeated in both Canada and Russia (Okhotsk Sea) in 1998. Timco et al. (2000) presented some of those results using a simple approximation of the punch shear strength as the average shear strength through the keel. The maximum in nine tests was 12.8 kPa and the average 8.5 kPa describing the lower bound, because these values included three tests in which the maximum load did not fail the keel. The lack of a proper constitutive model restricts the accurate analysis of test results. Some of the results of these tests are still proprietary.

It is known that properties in nature differ considerably from laboratory results, because the internal structure and time history are always different (Leppäranta and Hakala (1989) and (1992), Croasdale et al. (1997)). In the laboratory, tests are always performed on a smaller scale, and ice rubble is artificially manufactured, which causes different ice fragment shapes and sizes. In addition, a different temperature history and salinity affect the freeze bonds and consolidation by freezing. Evidently the texture of the rubble, consolidation and loading rate have caused large variations in interpreting results. Therefore, the comparison of results between small-scale and full-scale is uncertain. This establishes the need of in-situ full-scale testing.

2.2.6 Ridge load models

Several ice load calculation algorithms have been developed for first-year ridges. The forces contributed by the consolidated layer and rubble, are predicted separately and added together to build the global ridge load. Usually the material behavior of the keel and sail is adopted from soil mechanics. The models can be categorized as global or local according to the failure mode as shown in Fig. 2.7. Simultaneous failure is assumed to proceed along the failure plane in the ridge. Therefore, the failure mode is assumed beforehand.

Some of the models are based on the limit load approach in which the failure plane proceeds according to various kinematic mechanisms derived from compatibility requirements. Prodanovic (1981) developed an upper bound model based on Mohr-Coulomb material behavior. Maximum load F_h due to ice rubble in the keel is defined as

$$F_h = \sigma_p D_e h_k \left[1 + a \frac{h_k}{D_e} \left(1 + b \frac{h_k}{D_e} \right) \right] \tag{2.11}$$

where σ_p is the compressive strength of ice rubble in plain strain, D_e is the effective structure width and h_k is the keel thickness. Coefficients a and b depend on the friction angle.

Other models based on local failure have been developed by Dolgopolov et al. (1975), Mellor (1980), Croasdale (1980), Hoikkanen (1984), Krankkala and Määttänen (1984), Croasdale and Cammaert (1993) and Croasdale et al. (1994). Most of these models estimate the keel load, but some of them contain both the sail and keel load. There are a few theories presented by Croasdale (1980), Prodanovic (1981) and Croasdale and Cammaert (1993) that assumed global ridge failure. It should be noted that the present ridge load models predict only the maximum ridge load against a structure. Kärnä et al. (2001) developed a limit load model where the whole ridge penetration process can be simulated by updating the ridge geometry during the failure process.

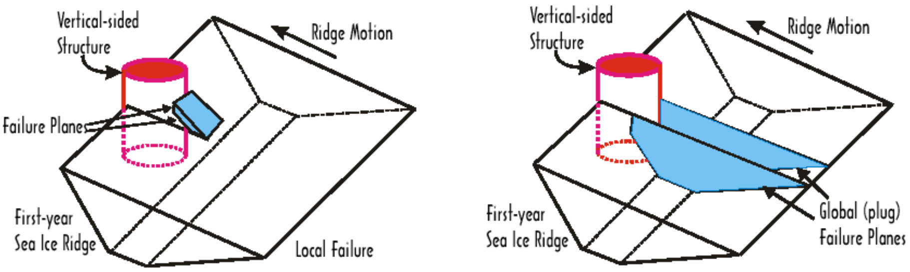

Figure 2.7. Local and global keel failure modes (Timco et al. 1999).

Wright and Timco (2001) characterized the frequency of different types of ridge failure modes measured in the Beaufort Sea with both wide and narrow structures. Due to pre-selection of the failure mode, the ridge load models cannot predict forces if a different type of failure mode takes place. The failure mode depends on several factors including the surrounding ice thickness, the size and age of the ridge, its continuity, velocity, structure shape and dimensions etc. Anyway, the failure process during ridge-structure interaction is not well known.

3 Full-scale testing of ridge mechanical properties

3.1 General

Full-scale ridge loading tests were carried out to determine the mechanical behavior of both ice rubble and the consolidated layer. A new testing method was developed and supplementary hardware needed to be designed and constructed. The goal was to load the ridge components resulting in similar failure modes to those realized in real ridge-structure interaction. In this thesis, the punch shearing of rubble is analyzed in details.

3.2 Site selection

Every year a variety of different ridges form early in the winter close to the coastline of Hailuoto Island, due both to pressure and shear action of moving ice fields further out in the Gulf of Bothnia. These ridges remain stationary, locked into landfast ice, for the rest of the winter giving a safe location for test camp on the ice. At Marjaniemi, the westernmost tip of Hailuoto (Fig. 3.1), is the University of Oulu Biological Research Center, which provides accommodation and restaurant services. Also, meteorological conditions provided for the Finnish Meteorological Institute, are recorded at a local ship navigation pilot-station.

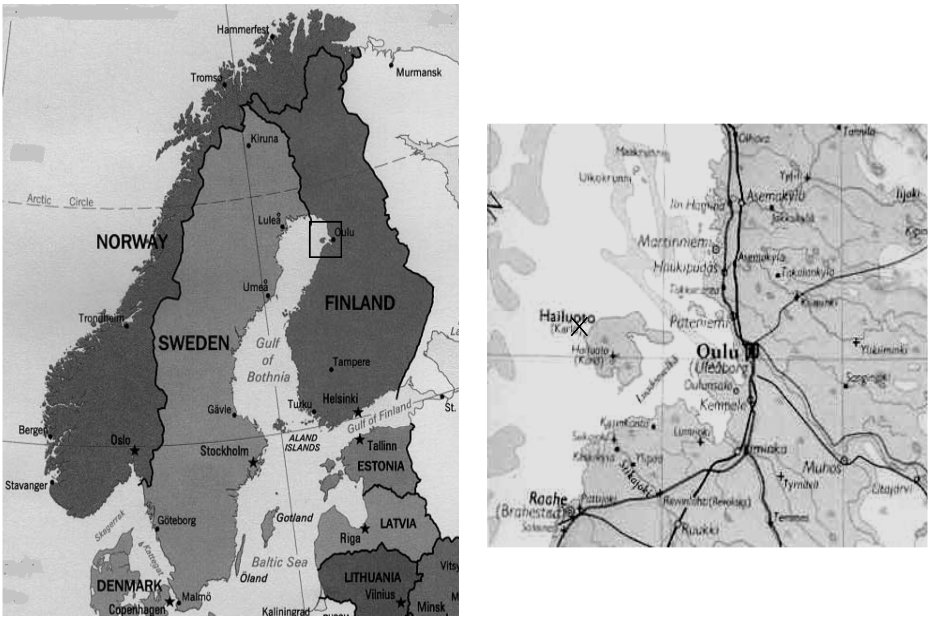

Figure 3.1. Map of the test site location. The site is marked by a cross on the right.

The Finnish Institute of Marine Research produces ice maps twice a week informing of the latest ice conditions. Based on this information an aerial survey was conducted every year in February to locate a good test site (Fig. 2.4.). Because access to a site can be complicated by extensive ridge formations or leads, prospective sites were visited by snowmobile immediately after the survey. The level ice thickness was measured by drilling to ensure safe transportation to the site, while the ridge keel depth was measured to ensure that the ridge fit the requirements for testing. For final site selection the dimensions of the ridge keel were the most important factor, followed by distance from the shore camp and the access route.

3.3 Development of testing methods

3.3.1 Test types

Assumed ridge failure mechanisms guided the planning of measurement procedures. Global ridge failure takes place by shearing along three-dimensional failure surfaces. Mechanical properties need to be determined both for the rubble and the consolidated layer in full-scale. Also, the interaction between the rubble in the keel and the consolidated layer had to be measured.

The first plan consisted four types of in-situ tests:
- ridge keel punch shearing test (vertical load)
- consolidated layer flexural strength test (vertical load)
- consolidated layer compressive test (horizontal load)
- consolidated layer shearing test on top of the rubble (horizontal load).

The testing procedure was expanded further for the last test period in 2003:
- level ice flexural strength test, both upward and downward loading
- uplift of a slab of consolidated layer

This thesis focused to the punch shear test. Therefore, the other test types are presented in STRICE and LOLEIF project reports (Heinonen et al., 2000(a,b) and 2004).

3.3.2 Punch shear test

During the punch shear test the ridge keel was loaded by pushing a circular plate downwards to break the rubble underneath (Fig. 3.2). As the purpose of the experiment was to load only the rubble of the ridge, the consolidated layer was cut free from the surrounding solid ice field. Also, to break simultaneously both the consolidated layer and the underlying rubble would need a very high load capacity, and it would be difficult to separate the contribution of these two elements in the measured failure load. Due to the submerged ice blocks, the rubble was loaded initially by buoyancy causing initial stress distribution.

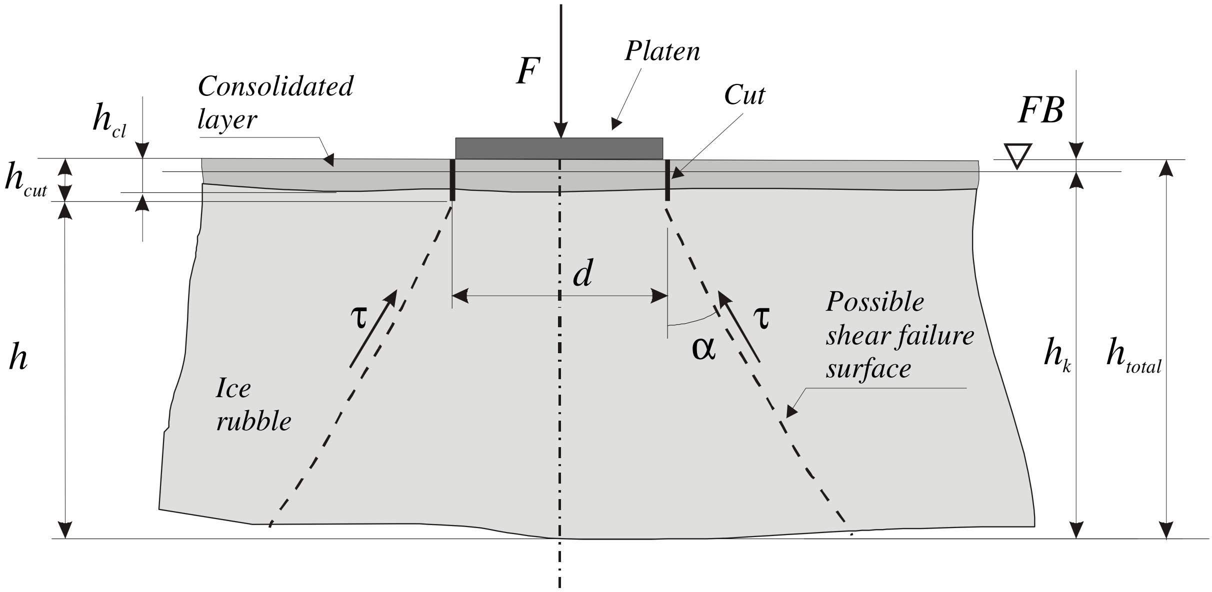

Figure 3.2. Principal sketch of the punch shear test.

The circular loading plate results in axisymmetric failure surface if the thickness of the underlying rubble is constant and the material is homogenous. To avoid the effects of individual ice blocks, the perimeter of the platen and the effective keel thickness (*h* in Fig. 3.2) need to be large compared to the size of the ice block. It was assumed that the perimeter of the platen and the effective keel thickness should be at least 10 times the block thickness. The effective keel thickness *h* is defined as follows:

$$h = h_k + FB - h_{cut} \tag{3.1}$$

where h_k is the keel depth measured from free board (*FB*) and h_{cut} is the cut depth. Based on the typical behavior of cohesive-frictional material, the failure plane was assumed to incline from the vertical direction as shown in Fig. 3.2.

Time histories of load and displacements in different locations must be measured for determining deformation mechanisms of ice rubble.

3.4 Development of hardware and instrumentation

A new test set-up was designed and constructed by the Laboratory for Mechanics of Materials at Helsinki University of Technology. Based on earlier estimates of ridge keel strength it was calculated that a punch load of about 1 MN is needed (Leppäranta and Hakala, 1989). The stroke has to be of the order of the parent ice sheet thickness.

Different choices for loading were considered. Only a hydraulic actuator is compact enough, it allows a sufficiently high and controlled loading rate, and it is versatile also for other types of testing in addition to punch shearing. A new lightweight cylinder was designed and manufactured specially for these in-situ ice tests. The final weight of the 1 MN per 0.70 m stroke hydraulic cylinder was only half of what was commercially available. A BobCat, a general-purpose tractor with front loader, had a high performance hydraulic power unit that was used to power the hydraulic actuator during all tests and the hydraulic chainsaw.

The reaction force of the hydraulic actuator was grounded to the surrounding ice field. This was accomplished by having a loading rig with a 9 m tall mast that transferred the reaction force first to the mast tip. From there steel wire ropes - up to 20 couples of diameter 14 mm - distributed the load to ice anchors located around an 8 m radius from the center of the punch load, as shown in Figs. 3.3 and 3.6.

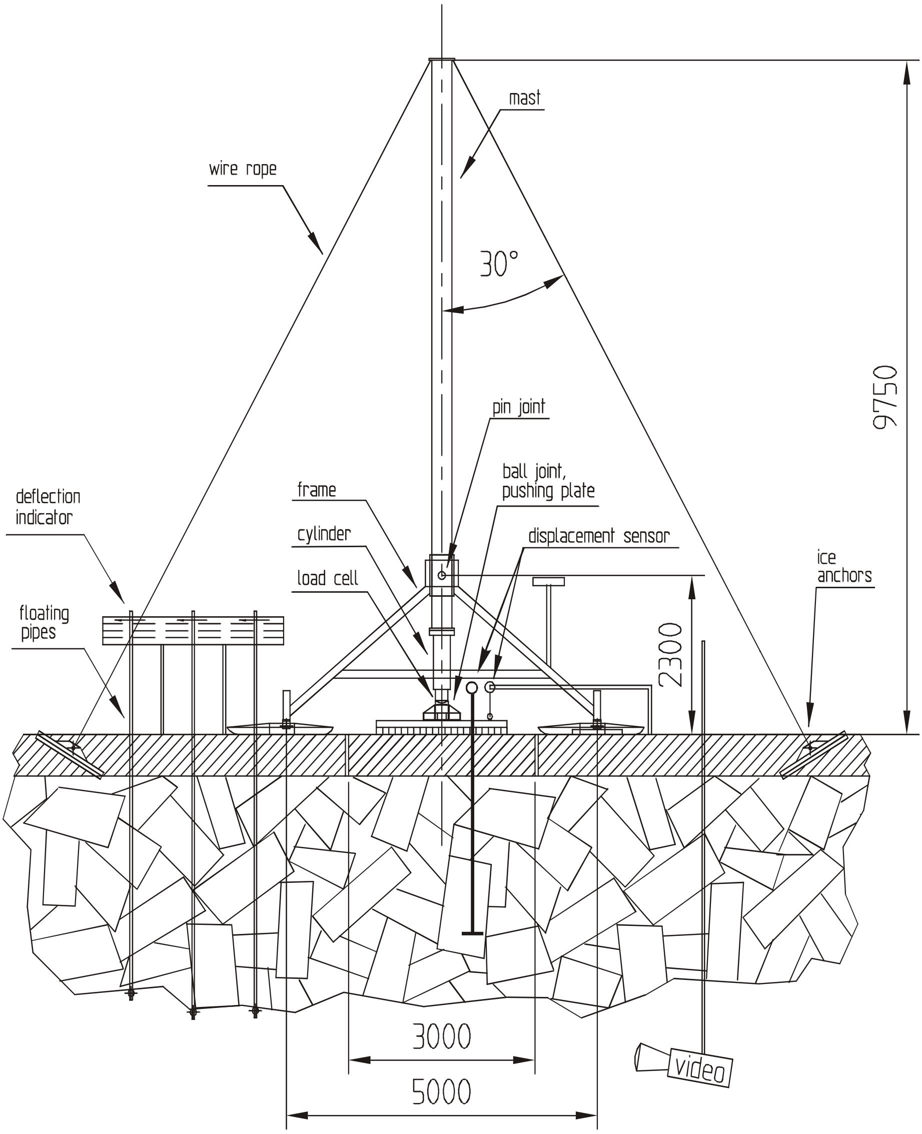

Figure 3.3. Hardware and instrumentation for the ridge keel punch test.

Ice anchors were simple steel pipes that were installed into a drill hole. The load was transferred perpendicularly to the center of an anchor through a steel flat. Usually the installation was left to adfreeze for the next day but the anchoring capacity proved to be adequate even without any adfreezing. Depending on expected load 12 - 20 anchors were used for the test.

The hydraulic cylinder used for the punch shearing tests was also used for consolidated layer crushing and horizontal shearing tests. The mast in the loading rig was tilted in a horizontal position, supported at the tip, and used to carry the weight of the hydraulic cylinder, as shown in Fig. 3.4. The cylinder could then be lowered to the proper level for horizontal crushing or shearing tests.

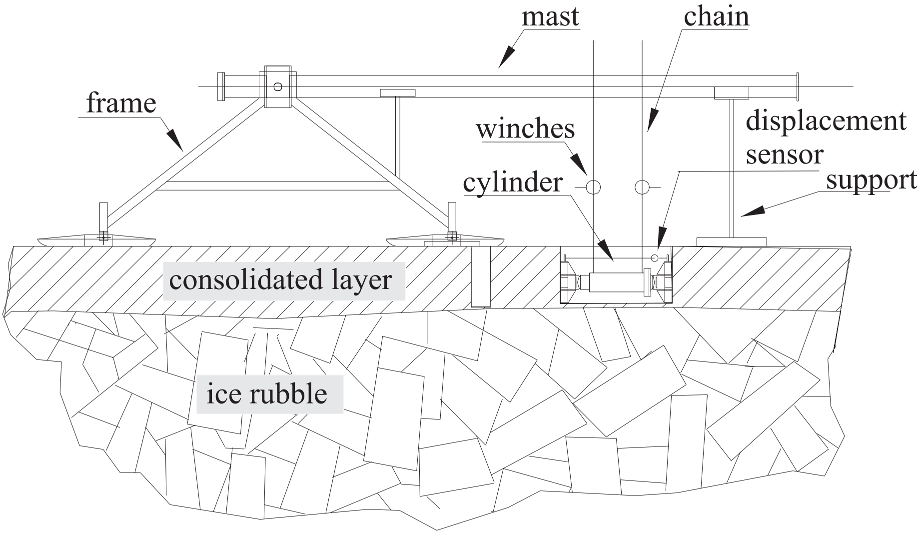

Figure 3.4. Cross section of the horizontal test set-up.

The loading rig was designed to be as lightweight as possible so it could easily be adapted to different test configurations. The weight was an important issue because on an open ice field manpower is the main source of energy for manipulating components while changing test configurations and adjusting the correct load application sequence. The vertical location of the mast can be adjusted. The erection of the mast was originally done with hand-driven winches but later a hydraulic actuator was added. The test rig was installed on skis so it could be towed from ashore to the test site with all components attached. The skis can be adjusted vertically, and the ski base and track width can be extended to span over a 7 m diameter test site.

Displacement transducers were used to measure direct displacement under the actuator, compaction of the rubble under the load, and propagation of the failure surface in the rubble. For the compaction measurement, a 2.5 m deep hole was drilled close to the center of the loading platen. The lower end of the displacement transducer was fixed to the anchor at the bottom of the hole. For failure surface propagation both mechanical and electrical transducers were used in two perpendicular arrays radially outward from the center (Figs. 3.3 and 3.5). The mechanical transducer was simply a float anchored to the bottom layer of the ridge keel. A rod in a hole through the keel indicated on the surface any movement down below. This was manually measured before and after the test and recorded by video camera during the test. The electrical transducer was similar to the one in the compression measurement, except that the anchoring was now made to the bottom of the ridge keel. At least six displacement transducers were used to measure the keel bottom displacement in each test.

Only standard video equipment was used for underwater video recording. A surveillance video camera was installed inside a watertight casing. Power and signal cables were passed through a plastic hose fixed watertight to the casing. The camera was installed at the end of a long rod and cables fixed to the rod. A 20 cm hole was drilled through the ridge keel and the camera was lowered through the hole about 2 m below the keel bottom. A hinge in the rod and camera bracket allowed the camera to be pointed towards the center of the test site. The location of the video was about 5 m from the center. The video monitor and recorder were installed in a hut on the ice. Underwater lights were also lowered under the keel bottom in the same way as the video camera. In general the lighting was less than optimal; the best footage could only be obtained if the ambient light was adequate. Sometimes it was hard to make a deep hole for the video camera through the ridge keel. An additional bonus was that while lowering the video camera through the rubble it was possible to see the structure of the rubble directly on the monitor. Also, viewing underneath allowed monitoring of the composition of floes at the lower surface of the keel. In one instance, diving with underwater video was accomplished.

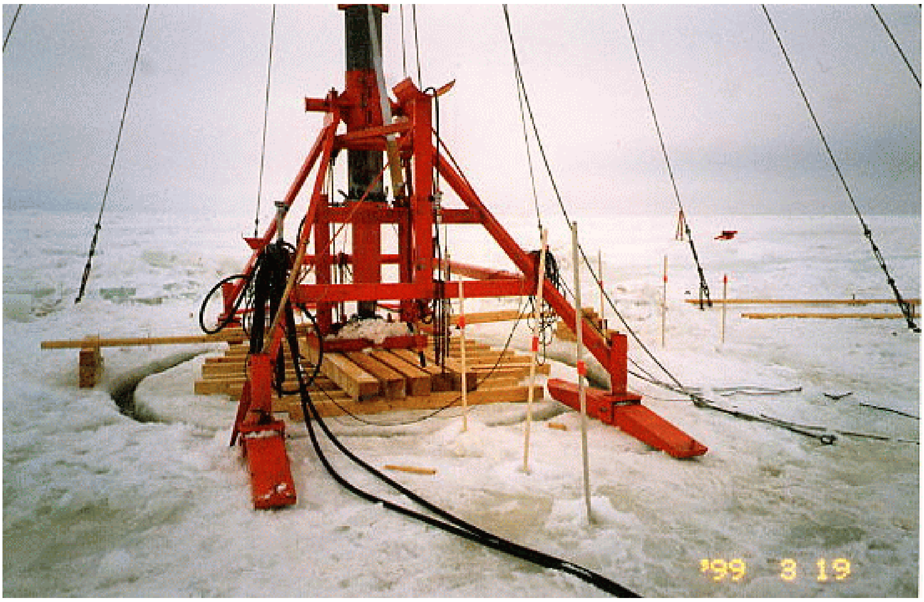

Figure 3.5. Photograph of the punch test set-up before loading, Test 11 in 1999.

3.5 Transportation

The main means of transportation on ice was an amphibious all-terrain Nasu Sisu vehicle. In addition to personnel transportation its trailer with a hoist was used to carry all the materials and provisions. A shelter for instruments and personnel was provided by two simple, rented caravans. The Nasu Sisu was used to tow the test rig, caravans and BobCat to and from the test sites.

3.6 Preparing the ridge for the experiment

Preparation for each ridge keel punch shearing test consisted following steps:

- ridge sail removal
- keel depth profile mapping by drilling
- test center location definition
- consolidated layer cutting
- ice anchor installations
- test rig installation
- wooden beams on top of the consolidated layer for even load distribution
- steel wire rope attachment to anchors and tightening
- load and displacement transducer installations
- underwater video installation
- initial state recording
- loading with data recording
- observations after load removal
- test rig removal

First the ridge sail and snow was removed or smoothened enough by the BobCat for controlled load application. To measure the keel geometry a grid of holes was prepared with a 2-inch diameter drill. The grid was rectangular with a spacing of 2 m between holes as shown in Fig. 3.6. The total keel thickness and freeboard were registered for each hole. Porosity of the keel was not recorded for each hole in each test-area, but in most test sites the porosity was determined in the holes covering the test platen (inner circle in Fig. 3.6). The number of holes drilled and the amount of porosity data recorded for each test-area varied.

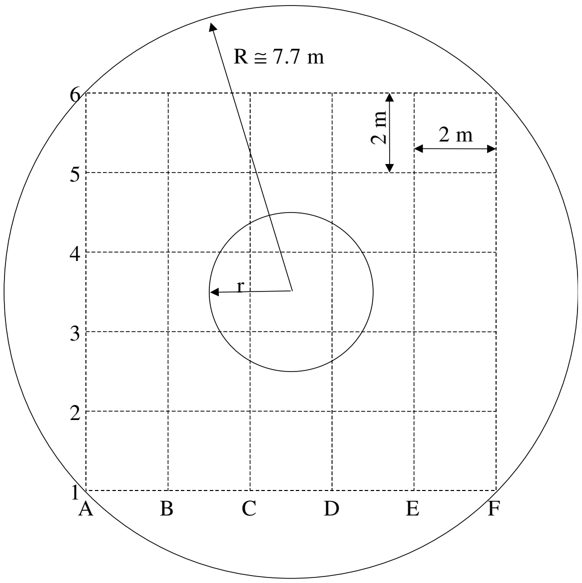

Figure 3.6. Schematic view of the grid of drilled holes. The anchors in the punch test were inserted in the larger circle; the smaller circle is the platen.

The consolidated layer under the load actuator was cut free from the surrounding consolidated layer by a chainsaw. In trials it was learnt that a chainsaw slit was not adequate even though the cut was made at an oblique angle. Polyethylene sheets in the chainsaw cut were tried to prevent parts from sticking to each other, with poor success. Therefore, a wider cut was accomplished by making two parallel chainsaw cuts 10 - 15 cm apart and removing the intervening ice. This was time-consuming and required a lot of manpower. In some cases when the chainsaw did not reach through the whole consolidated layer, cutting was extended by drilling 10 cm holes side by side into the bottom of the cut. Chainsaws had problems with slush getting into the induction air. An improvement was to use a hydraulic chainsaw. The hydraulic excavator in the BobCat was also applied during the last measurement campaign, which cut the preparation time drastically.

3.7 Ice characterization

Ice characterization was carried out in 1999, 2000, 2001 and 2003. The university of Oulu conducted crystallographic studies and uniaxial compressive tests for the ice samples taken from the consolidated layer during the measurement period from the test site at Marjaniemi. Both horizontal and vertical thin sections were prepared with a microtome. Polarized light and photography were used to distinguish different ice crystals and their size.

Ice uniaxial compression tests were made using closed loop material testing equipment (Fiskars) in a -10°C cold room. The loading rate was chosen to be about 10^{-3} s^{-1} to correspond to the highest ice strength in the transition zone. Ice samples were first cut by a band saw close to the final size. A cylindrical shape was made with a lathe and the ends were cut with a band saw. Compliant platens according to IAHR guidelines were used to ensure uniform deformation during the compression. A data logger recorded the load and deformation.

3.8 List of field test program

Altogether 33 ridge mechanical loading tests were performed during LOLEIF and STRICE projects in winters 1998-2001 and 2003. Different tests are presented in Table 3.1.

Table 3.1. Test program for ridge mechanical loading.

Year	1998	1999	2000	2001	2003	Total
Punch test (vertical)	2	5	3	2	0	12
Bending test (vertical)	0	1	1	4	3+5(**	14
Horizontal compression test	1	2(*	0	0	0	3
Horizontal shear test	1	2	0	0	0	3
Uplift test (vertical)	0	0	0	0	1	1
Total	4	10	4	6	9	33

(* During the 2nd test the connector between the hydraulic hose and cylinder broke.

(** Bending tests for solid ice without underlying rubble, both downward and upward loading.

4 Test results

4.1 General

The main objective of the test series was to measure the full-scale ridge keel material parameters in order to develop a constitutive model for ridge keel failure predictions by the Finite Element Method (FEM). Tests were conducted by applying a vertical load to a circular platen until the underlying ridge keel failed by punch shearing as described in Ch. 3. By varying the diameter of the platen in relation to the keel depth, a different type of internal stress distribution could be evaluated in the keel. This makes it easier to distinguish the contribution to the failure load of two different failure mechanisms: compaction and shear failure. The stress distribution in a thick keel is determined by the shear and compression stresses. In the case of a shallow keel, bending of the keel might affect the stress distribution causing tensile stresses at the keel bottom. This was studied numerically in Ch. 7. As a continuum model was sought, the diameter of the platen was chosen to be so large that individual floe failures in the developing failure surface would not induce too much variation. In practice the keel depth and platen perimeter were chosen to be at least ten times the ice block thickness, which was usually around 0.2 m. The thinnest keel was 2.2 m and the smallest diameter 2.5 m, creating a perimeter of 7.9 m. The first one is 11 times the ice block thickness, the latter 39 times. No exact value is known for the minimum ratio between the loaded keel geometry and an individual ice block to describe continuum behavior.

Typically in ice related problems, especially in the case of ice rubble, accuracy of results cannot be quantified in high confidence level. All recordings with calibrated transducers were very accurate (maximum error was below 1%). However, without making experimental uncertainty analyses, one can establish other error sources as:

- Fixing of the displacement transducers inside the rubble (compaction measurement) and at the keel bottom could be incomplete, because there was no visual contact while connecting the transducer.
- Geometry of the keel (thickness) was determined manually by drilling a grid of holes through the keel (Fig. 3.6). Precision in drilling work is fairly coarse. The maximum error in thickness measurement is approximately

±10cm. However, in comparison to typical keel thickness from 3 to 6 m, the maximum relative error is between 2% and 3%. The error in the average keel thickness will be less, because some of the error compensates each other. The total error in keel bottom shape is composed of the measurement error and the use of a discrete grid. The error in geometry will further affect material parameters defined from the maximum load and keel geometry in the punch tests. Also, the buoyancy load due to submerged rubble depends on the keel volume and therefore geometry determination.

4.2 Measured quantities and locations of transducers

Following quantities were measured in punch shear tests:

- force F pushing the platen downwards
- platen displacement u
- displacement inside rubble in relation to platen displacement defined as compaction of rubble Δu
- keel bottom displacements (X_1, X_2, X_3, Y_1, Y_2 and Y_3)

Compaction of rubble Δu is defined as

$$\Delta u = u - u_1 = L_0 - L_1 \tag{4.1}$$

which is positive when the displacement inside the rubble u_1 is less than in the platen u. L_0 describes the original and L_1 the current distance between the top of the platen and the sensor location (Fig. 4.1).

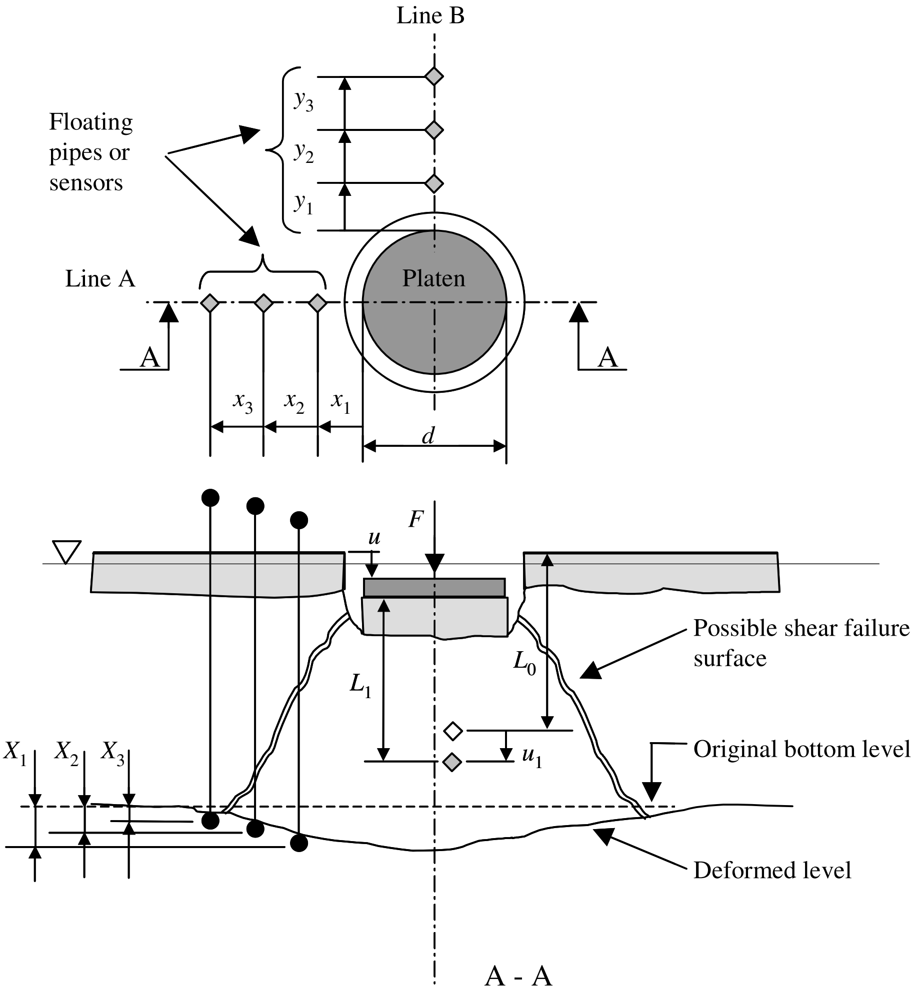

Figure 4.1. Measurement of displacements at the bottom of and inside the keel. Top view above and cross-sectional view below.

Keel bottom displacements were measured by floating pipes at three positions in two perpendicular lines, A and B, as shown in Fig. 4.1. The level of each pipe was measured three times:

- the original level before a test
- the level when the platen was at the lowest position
- the permanent level after a test, when the load was relieved and the piston in the hydraulic cylinder was driven back to the initial position.

Therefore, the differences in the last two readings gave recoverable movements. Accurate locations of the sensors were measured for each test case. Levels for the pipes were marked with red tape, making the level changes easier to follow on the video recording.

In 2000, LVDT displacement sensors were used instead of floating pipes in one or two holes closest to the platen. The LVDT sensors recorded time history data instead of the displacement at two points in time: when the platen was at the bottom level, and the permanent displacement after a test. LVDT sensors were replaced by potentiometer transducers for the last two measurement campaigns (2001 and 2003). Displacement time histories in Tests conducted in 1999 were recorded only for the platen and inside the rubble.

The sensor measuring the displacement inside the rubble in relation to the platen was fixed at the depth of roughly 2.5 m. Locations of the keel bottom displacement devices are shown in Table 4.1.

Table 4.1. Locations of keel bottom displacement devices corresponding to the dimensions shown in Fig. 4.1.

		Line A			Line B		
Test #	$d/2$ (m)	x_1 (m)	x_2 (m)	x_3 (m)	y_1 (m)	y_2 (m)	y_3 (m)
0/2000	1.50	0.75	1.50	2.25	0.75	1.35	2.10
3/2000	2.35	0.65	1.15	1.65	0.65	1.15	1.65
4/2000	1.55	0.45	0.95	1.45	0.45	0.95	1.45
10/1999	2.25	0.65	1.65	2.65	0.65	1.65	2.65
11/1999	2.05	0.50	1.25	2.00	0.50	1.25	2.00

4.3 Time history data of punch tests

An appropriate loading rate was chosen both to avoid creep deformations and to avoid pore pressure effects due to water in cavities. The loading rate was adjusted by the hydraulic pump of the BobCat. Maximum flow accomplished maximum piston velocity equal to 30 mm/s but in all test cases it was adjusted lower. The control system did not receive feedback information. Therefore, the platen velocity was not exactly constant during large load drops, being lower before global keel failure than afterwards.

The maximum total effective time for the tests was around 40 s. The load build-up time was usually less than 7 s, but longer in two cases. In some tests the platen was first pushed down at the lowest level (stroke 700 mm). Next the load was relieved and the load was increased again by pushing the platen down. The total time for two load cycles was around 140 s. Maximum values for the loads ($F_{\max}$) and respective values for time and displacements (u) are shown in Table 4.2. Also shown are the main dimensions, keel thickness (h_k), effective keel thickness (h), diameter of the platen (d) and the ratio d/h (dimensions are shown in Fig. 3.2). The keel thickness was averaged from the drilling results of each test site.

The following five punch test cases from 1999 and 2000 were selected for a detailed study in finite element simulations:

- Test 0/2000
- Test 3/2000
- Test 4/2000
- Test 10/1999
- Test 11/1999

The list of selected tests contains all tests from 2000, because in 2000 the instrumentation was developed further from 1999 to account also time history measurements of keel bottom displacements. To investigate rubble mechanical behavior in different ice conditions, two cases were selected randomly from 1999. Rough analysis based on an analytical model was made for all punch tests from 1998 to 2001 (Ch. 4.5). The recorded time history curves for each selected case are shown in Figs. 4.2-4.6.

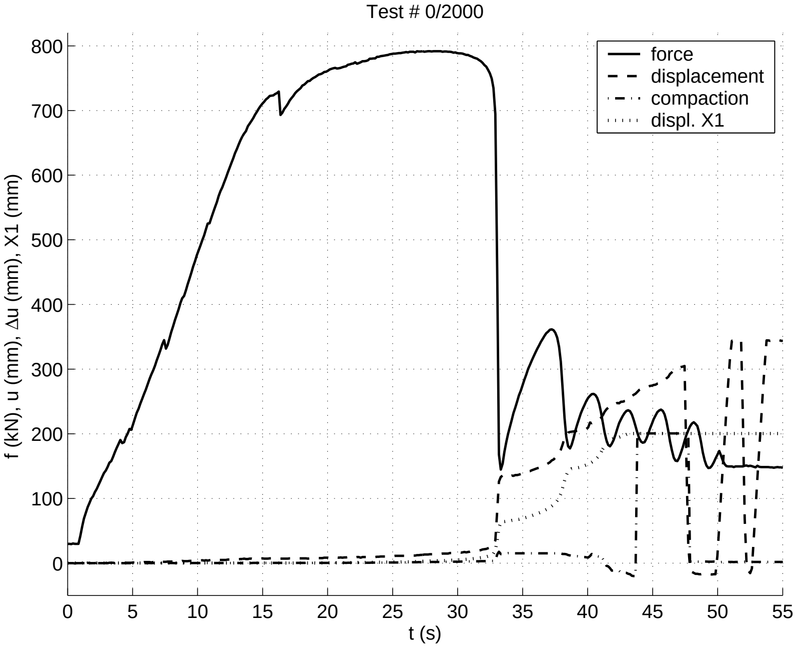

Figure 4.2. Time history plots from Test 0/2000 showing the pushing force (f), platen displacement (u), compaction of the rubble (Δu) and keel bottom displacement (X_1).

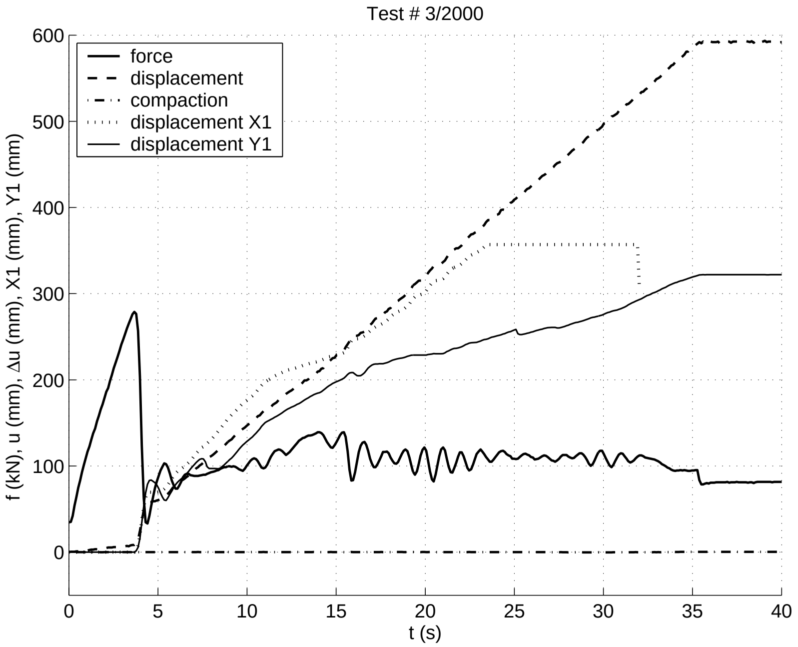

Figure 4.3. Time history plots from Test 3/2000 showing the pushing force (f), platen displacement (u), compaction of the rubble (Δu) and keel bottom displacements (X_1) and (Y_1).

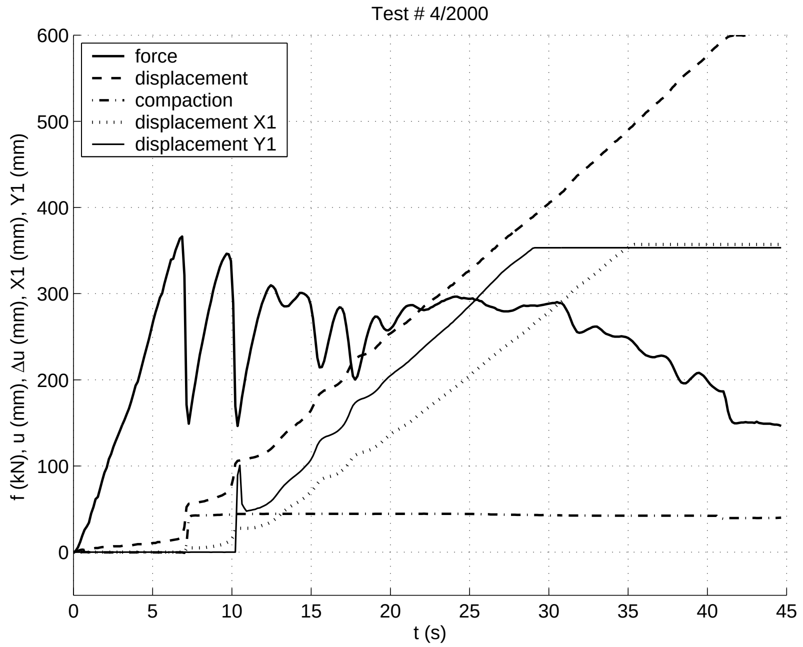

Figure 4.4. Time history plots from Test 4/2000 showing the pushing force (f), platen displacement (u), compaction of the rubble (Δu) and keel bottom displacements (X_1) and (Y_1).

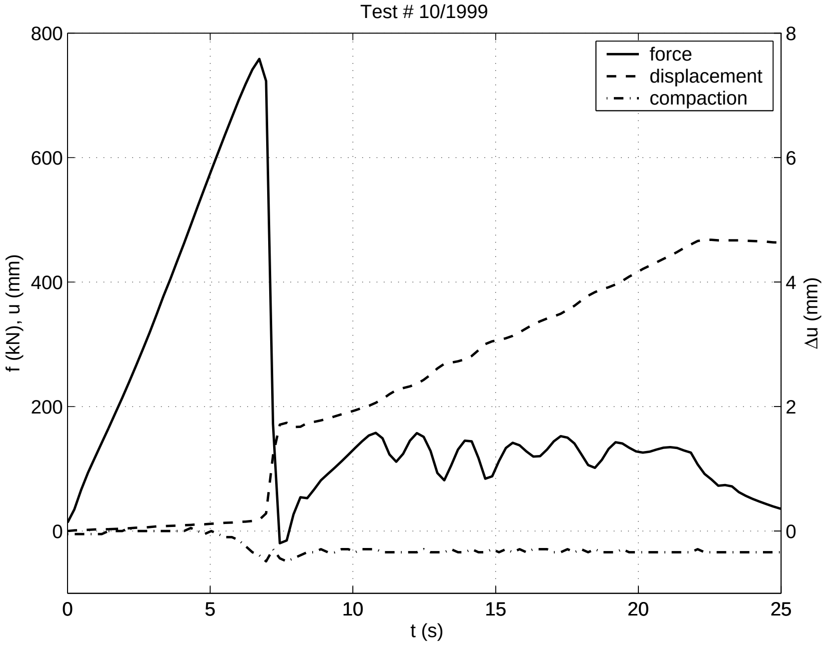

Figure 4.5. Time history plots from Test 10/1999 showing the pushing force (f), platen displacement (u) and compaction of the rubble (Δu).

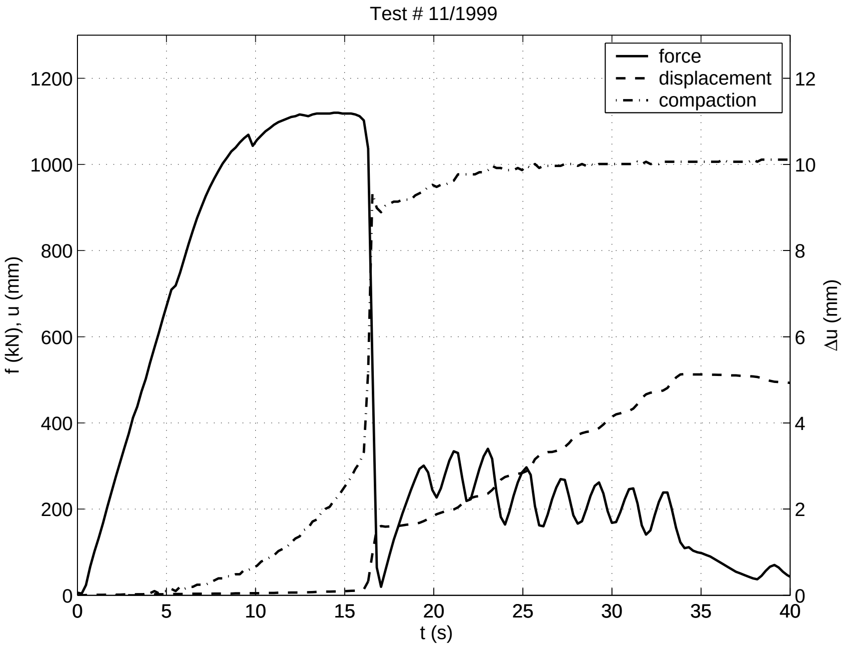

Figure 4.6. Time history plots from Test 11/1999 showing the pushing force (f), platen displacement (u) and compaction of the rubble (Δu).

Table 4.2. Load capacity, corresponding displacement and time and main dimensions in the selected punch tests.

Test #	$F_{\max}$ (kN)	u (mm)	at time (s)	d (m)	h_k (m)	h (m)	d/h
0/2000	792	12.2	26.9	3.0	5.2	4.6	0.65
3/2000	279	8.3	3.7	4.7	3.0	2.2	2.15
4/2000	366	18.1	6.9	3.1	4.9	4.1	0.76
10/1999	758	18.1	6.7	4.5	4.5	3.1	1.44
11/1999	1120	8.8	14.4	4.1	6.4	5.0	0.82

Fairly similar time histories were recorded in each test also when comparing the results between various winters. First the force grew linearly to the first global keel failure, then dropped steeply. In two cases (0/2000 and 11/1999) the force flattened out before global failure. The maximum load (peak load) was reached just before global failure. Afterwards the load had smaller peaks. The first load peak was mostly much higher than subsequent peaks. Blocks are fastened together cohesively, which can be interpreted as there being a skeleton, or as blocks being wedged to each other yielding a cohesive-type structure. The first break is due to a break of the skeleton structure. Once the skeleton is broken, the shear failure propagates further as loading continues. Smaller subsequent peaks are partly a consequence of individual floe failures in the rubble. Also, rearrangements of the blocks can cause peaks in the load response.

Significant displacement jumps of the platen were found mainly in the first load drop. Subsequently the displacement grew fairly smoothly, except in Test 4/2000, where also the second force drop caused a high jump. Large drops are consequences of skeleton failure, where several blocks fail simultaneously in the shear failure zone close to the edge of the platen. As the failure proceeds deeper in the keel, the probability of block failure decreases. The blocks can move and rotate in a lower pressure state and therefore can avoid failure. In such a case, rubble failure is a consequence of rearrangement of ice blocks.

The steel wire ropes in the test rig store lots of strain energy, which is released when the keel breaks. This disadvantage of the test system causes a higher shear rate during the force drop, and larger force drops during global keel failure as well as after subsequent smaller force peaks. The post peak load response is more likely dynamic instead of the static approximation, and the measurement does not describe the keel softening phase correctly. Therefore, this study concentrates on measuring the global keel load capacity and on simulating progressive keel failure up to the peak.

The difference between the tests is seen both in the load and in the displacement curves. When the load capacity of the keel is low enough, as in Tests 3/2000, 4/2000 and 10/1999, the force increased linearly until the first global failure occurred. The maximum load was achieved within 7 s, corresponding to a short load build-up time. However, in two cases (0/2000 and 11/1999) almost constant loading was applied for a longer time (26 and 14 s to the maximum force). The force grew linearly with time, then evened out and stayed almost constant until failure. In these cases the capacity of the loading system was almost reached. Despite the different force curves in the time domain, the force-displacement response was very similar for all tests (Fig. 4.7). The load increased linearly to the maximum value. Therefore, the load-build-up time was short enough in all cases to neglect time dependent deformation mechanisms, as mentioned also in Ch. 2.1 and by Beltaos (2002). In Tests 0/2000 and 11/1999, hydraulic flow decreased due to higher internal leaks of the hydraulic system causing a lower loading velocity and a lower strain rate in the keel. Although the same kind of Bobcat was applied in every year, the hydraulic power varied. The load capacity was significantly lower in 2000 than in 1999.

In Test 4/2000, the secondary load peaks were almost as high as the first one. In addition, the residual force level was approximately half of the maximum force, which is much higher than in all other tests. Due to the uneven keel thickness the platen tilted slightly during loading in Test 4/2000. After the first global keel break, the part of rubble under the platen was also tilted and at same time pressed against intact rubble on the other side of the failure plane. Due to the tilting of the platen, the axisymmetric approximation in the analysis in Ch. 7 is less accurate.

Significant displacements were measured inside the keel in relation to the platen in most of the tests cases indicating compaction of rubble. In some cases the relative displacement was too small to make any observations. The sensor was difficult in practice to fix into the rubble, and because individual blocks can move and rotate relatively much, there was some uncertainty and overflow of the measurements. In some cases the measurement indicated larger displacement inside the rubble than in the platen, which was interpreted as individual ice block rotation. If the ice block is initially in a lateral position, it rotates considerably because one edge moves upwards while the vertical load is transmitted at the other edge. A closer study of keel deformations is made in Ch. 4.4.

In Tests 3/2000 and 4/2000 the platen was first pushed at the lowest level (stroke 700 mm). The load was relieved and in Test 3/2000 increased again by pushing the platen down. The pushing force was much lower in the second push than in the first. In addition, significant load oscillation was no longer observed. This strongly indicates that the ice blocks in the rubble are cohesively connected to each other, creating a skeleton type of structure that behaves basically as cohesive-frictional material.

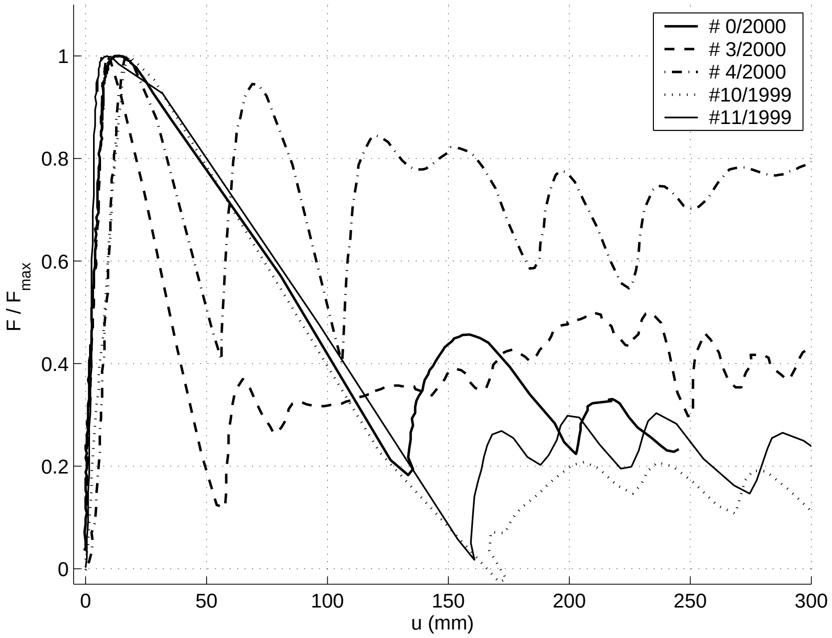

Figure 4.7. Non-dimensional force (force/max force) versus platen displacement for all selected tests.

4.4 Keel deformations

In Test 0/2000, a small amount of compaction was observed when the first failure occurred (at about 33 s as shown in time history curve Fig. 4.2). Larger compaction was recorded subsequently as the rubble failure proceeded further, until 44 s when the sensor probably became detached. An overflow of the displacement measurement system restricted further recording.

In Test 3/2000, no results were recorded inside the rubble. One could assume unsuccessful fixing of the displacement sensor, which was difficult to achieve in rubble. However, both bottom displacements (X_1 and Y_1) indicated approximately the same movements as in the platen. Therefore, the rubble did not really compact in the case of the thin keel.

In Test 4/2000, the rubble compacted at the same time as the first global failure (at 7 s). Subsequently the amount of compaction stayed at the same level while loading continued. Also, the keel bottom displacement increased with the same rate as the platen displacement after the peak load, with some delay.

Test 10/1999 did neither show any significant compaction, but Test 11/1999 indicated similar compaction that was found in Test 0/2000 as shown in Fig.4.8.

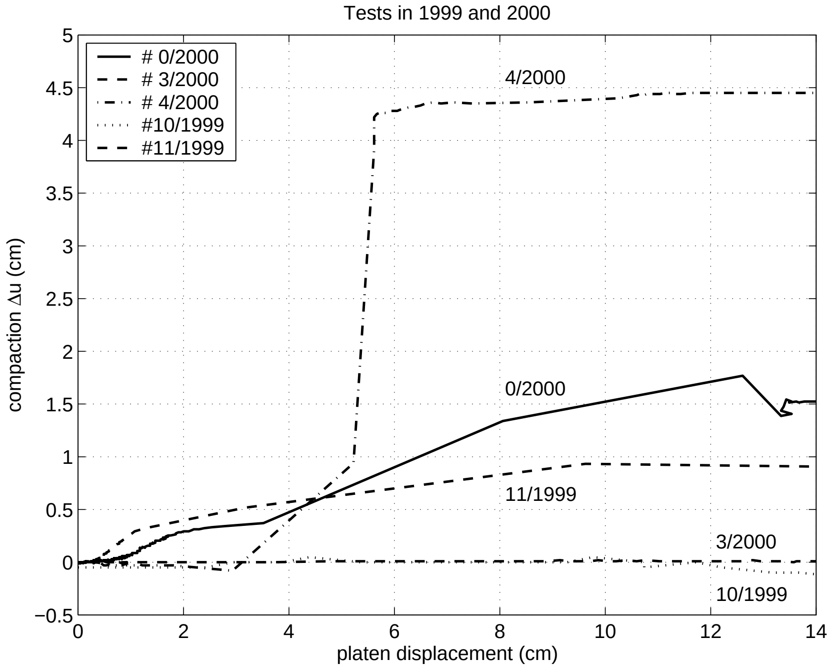

Figure 4.8. Compaction of the rubble as a function of the platen displacement for tests in Years 1999 and 2000.

Compaction of the rubble is presented in Fig. 4.8 as a function of platen displacement. In most cases, compaction of the rubble increased during the pushdown. In Test 4/2000 the compressibility was slightly negative at the beginning but it turned to compaction after the peak load. Once the failure surface was activated, the rubble moved as a rigid block while the pushdown load continued. In that case, the subsequent load peaks were relatively high in comparison the global peak (Fig. 4.4).

Keel bottom displacements from the measurements in 2000 are shown in Figs. 4.9-4.11 as a function of the platen displacement. Table 4.1 presents the location of each device. All curves are cut due to overflow of the measurement range. LVDT sensors were replaced by potentiometer transducers with a larger operation scale for the subsequent measurements.

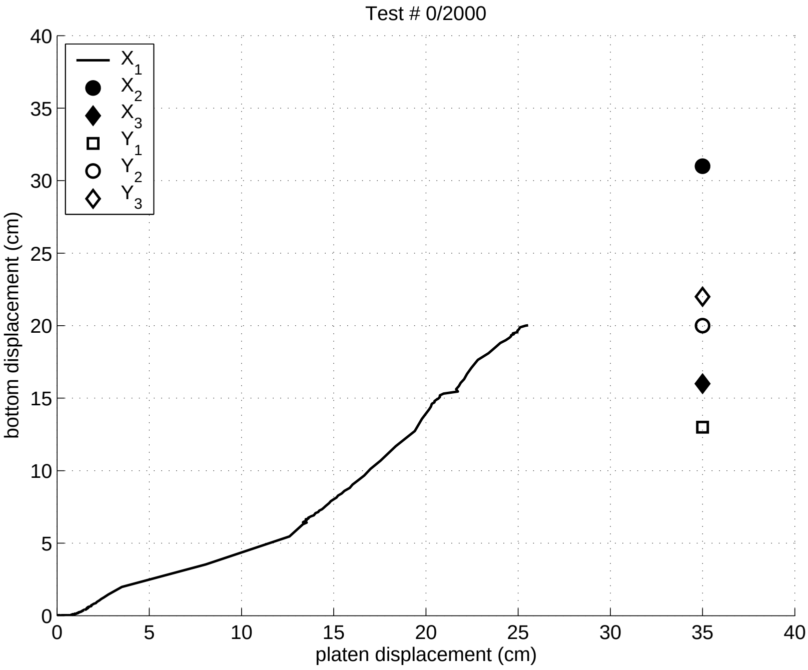

Figure 4.9. Keel bottom displacements in Test 0/2000. Manual measurements along two perpendicular lines with floating pipes are indicated by symbols.

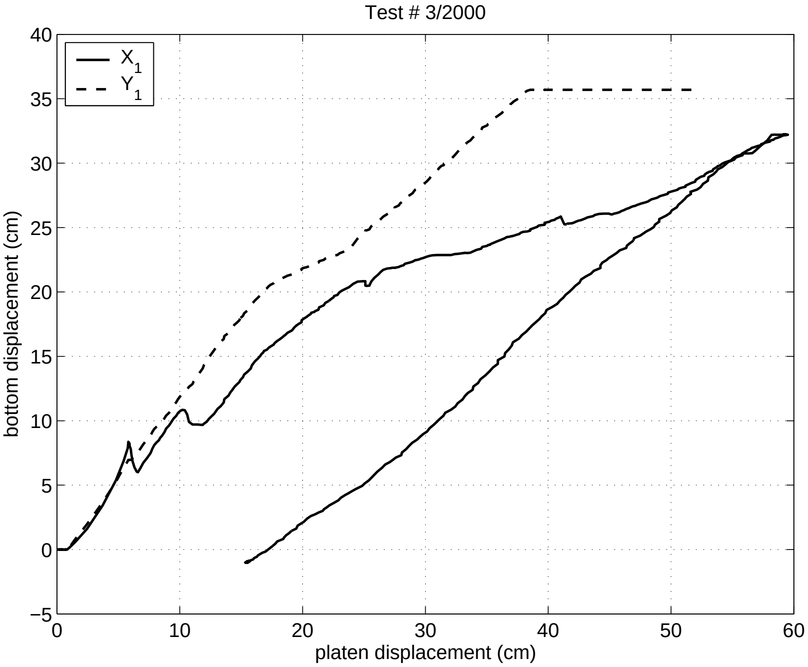

Figure 4.10. Keel bottom displacements in Test 3/2000.

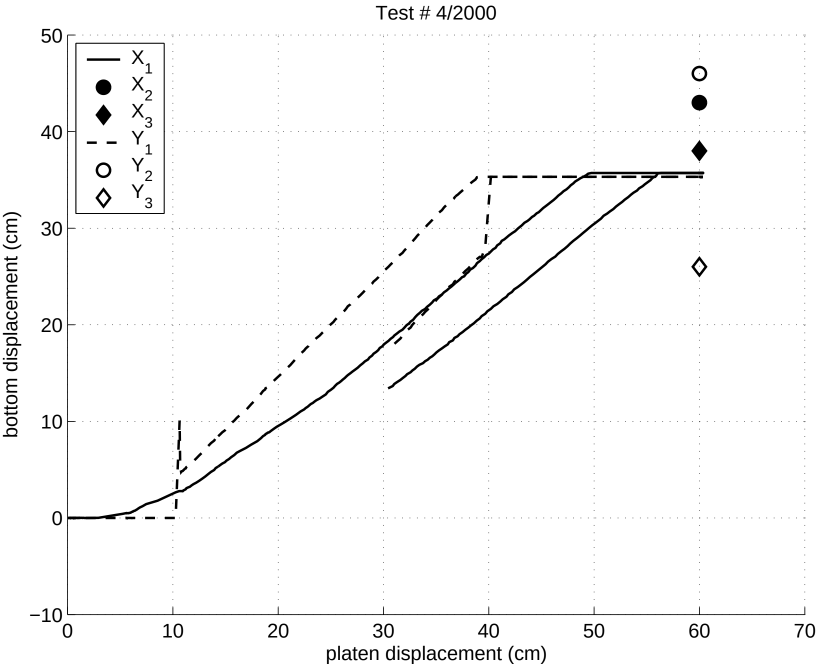

Figure 4.11. Keel bottom displacements in Test 4/2000. Manual measurements along two perpendicular lines with floating pipes are indicated by symbols.

Displacements at the keel bottom indicated good agreement between continuous time history measurements and discrete measurements through floating pipes. Also, continuous measurement at two points resulted in very similar displacements as seen in Tests 3/2000 and 4/2000. In the case of the thin keel (Test 3/2000), the discrete measurements did not show any movements at keel bottom indicating rather vertical (cylindrical) failure surface. It was also observed that two out of four floating pipes were not fixed properly because the pipes did not float. However, in two other cases (Tests 0/2000 and 4/2000) rather large displacements at the keel bottom were measured at all points. Thus, the area which moves at the keel bottom is much larger than the loaded area at the top, indicating that the failure proceeds through the keel along the surface which spreads outwards.

The keel bottom displacements were larger closer to the center-line than further away in most cases. However, Test 0/2000 indicated an opposite trend, probably caused by individual block movement rather than continuous rubble deformation.

Permanent movements were observed for both the platen and the keel bottom displacements after unloading, supporting the use of plasticity theory in the analysis.

Underwater video observation also indicated that the whole keel moved downwards during the pushdown. In some cases the floating pipe movement was also observed by the underwater video. Generally, it was difficult to predict the underwater movements because the underwater scale was missing. However, visual observations of rubble movements increased understanding of rubble deformation mechanisms and supported the model development.

4.5 Summary of experimental data

A total of 12 punch shear tests were completed while the diameter to keel-depth ratio varied from 0.65 to 2.15. The largest punch plate diameter was 4.7 m and the deepest keel 6.4 m. The main values describing the punch load capacity are listed in Table 4.3. In some tests the capacity of the load actuator was not initially enough to break the coherence of floes sticking out from the keel to the consolidated layer under the punch plate. In such cases the cut around the platen was opened deeper and the test continued. In general, the tests were successful and the quality of data can be regarded to be very good. Improvement would be needed only in making the test rig stiffer. The stored elastic energy in steel wire ropes makes the displacement rate after the first failure much faster than the otherwise controlled rate of load actuator advance.

The maximum nominal pressure at the top of the platen (q) is defined as the maximum force over the loaded area:

$$q = \frac{F_{\max}}{\pi d^2/4} \tag{4.2}$$

where $F_{\max}$ is the maximum force measured during the punch test and d is the diameter of the platen.

Table 4.3. Main values from the punch tests. $F_{\max}$ *= maximum force, d = platen diameter, h = effective keel thickness,* h_k *= keel thickness, q = maximum nominal pressure,* η_k *= keel porosity,* η_r *= rubble porosity, FB = freeboard,* h_{cut} *= cut depth, NM = Not Measured.*

Test #	Site #	$F_{\max}$ (kN)	d (m)	h (m)	h_k (m)	q (kN/m^2)	d/h	η_k (%)	η_r (%)	FB (m)	h_{cut} (m)
1998											
1	1	223	2.6	3.7	4.5	42	0.70	NM		NM	0.80
2	2	677	3.7	4.7	5.5	63	0.80	NM		NM	0.80
1999											
2	1-1	765	3.3	4.0	4.6	88	0.84	34	38	0.20	0.80
6	1-2	936	3.4	2.8	4.0	106	1.21	27	31	0.26	1.50
9	2-1	695	3.4	4.0	5.6	77	0.84	31	35	0.00	1.60
10	2-2	758	4.5	3.1	4.5	48	1.44	42	46	0.06	1.40
11	2-3	1120	4.1	5.0	6.4	87	0.82	37	41	0.10	1.50
2000											
0	1	792	3.0	4.6	5.2	112	0.65	37		0.27	0.85
3	3	279	4.7	2.2	3.0	16	2.15	34		0.06	0.90
4	4	366	3.1	4.1	4.9	48	0.76	NM		0.20	1.00
2001											
1	1	74	4.6	2.7	3.7	4	1.7	38		0.13	1.00
2	1	201	2.5	4.0	5.0	41	0.6	18		0.14	1.00

The load capacity in the punch test depends on the geometrical dimensions, effective thickness of the keel and the diameter of the platen. The maximum nominal pressure is presented in Figs. 4.12 and 4.13 as a function of the ratio *d/h* and of the thickness *h*. A trend line based on regression analysis ($y = a + bx$, where *a* and *b* are constants) has been added into the plots. A clear trend can be seen between the maximum nominal pressure and the keel thickness. Obviously, the thick keel has a higher load capacity than the thin one. The trend is not as self-evident when the *d/h* ratio varies. Despite the decreasing trend line, it should be noted that most of the points lie around the value $d/h \approx 0.75$ and the load variation is large, resulting in poor fitting. It was assumed beforehand that the failure mode in the keel depends on the *d/h* ratio, because the stress state inside the keel is different. With large values for *d/h* ratio (the keel is shallow) the bending deformation changes the stress distribution, causing tensile stresses at the bottom part of the keel. That effect was studied by seeking large values for the *d/h* ratio.

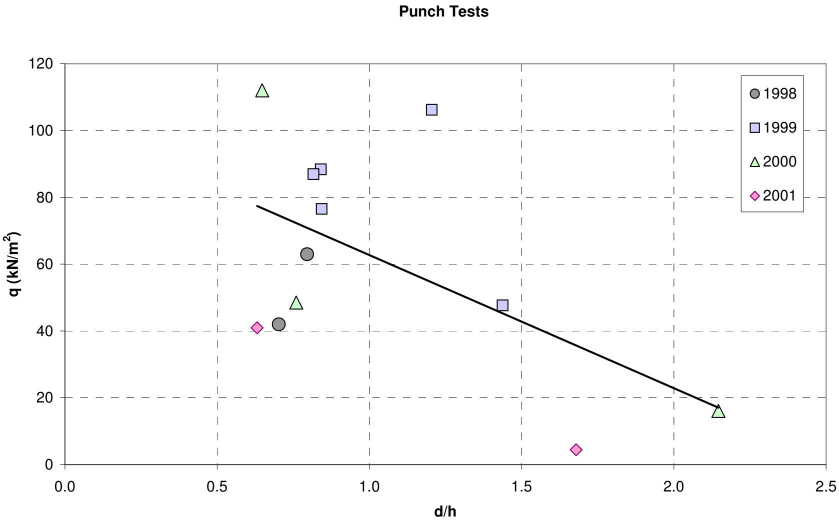

Figure 4.12. Maximum nominal pressure versus d/h ratio.

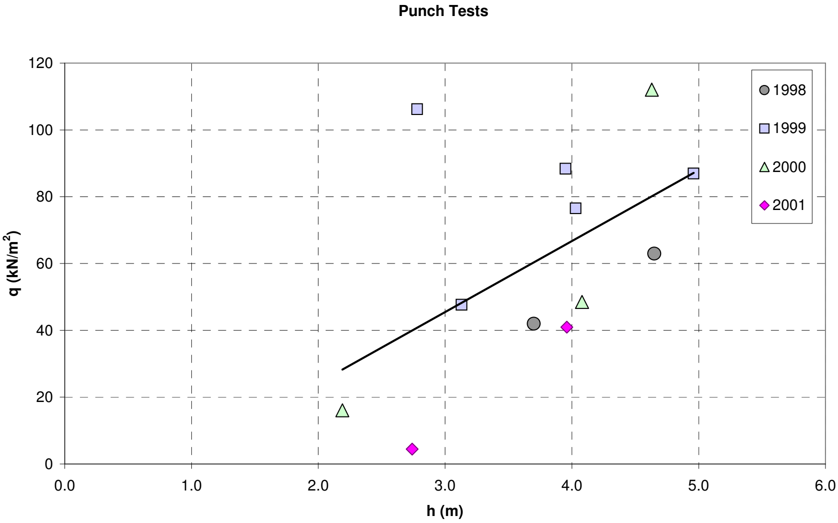

Figure 4.13. Maximum nominal pressure versus effective keel depth.

The first approximation of the shear strength in the keel is made by assuming a cylindrical failure surface by choosing angle α = 0 (Fig. 3.2). The average shear strength along the failure surface is therefore

$$\tau = \frac{F_{\max}}{\pi d h} \tag{4.3}$$

The average shear strength is plotted against the keel depth in Fig. 4.14. The results from each test are presented in Table 4.4. More advanced predictions are based on the limit load approach, upper bound solution (Heinonen and Määttänen, 2000(c)) or lower bound solution (Jensen et al., 2000). The rubble was modeled using the Mohr-Coulomb material model. The major difficulty in limit load models with the pressure-dependent failure criterion is that the internal stress state in the keel is approximated. Thus, the separation of the cohesive and frictional contribution in the shear strength is uncertain, supporting the numerical finite element application.

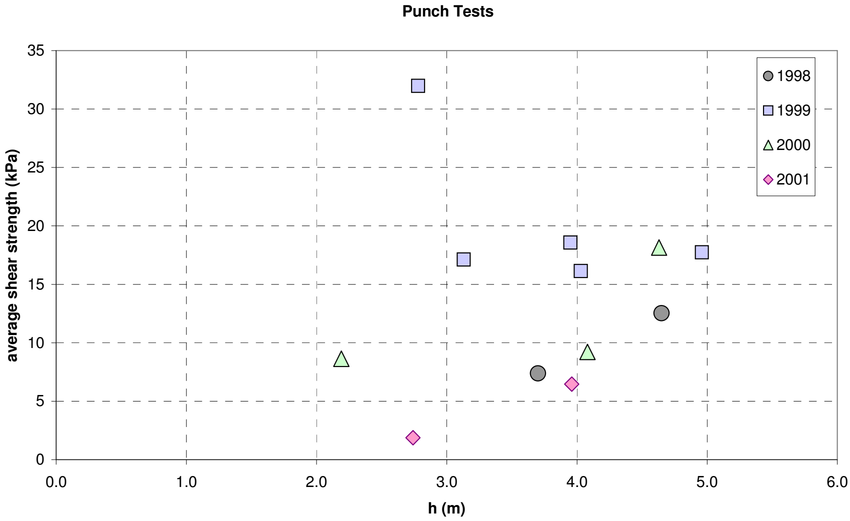

Figure 4.14. Average shear strength versus effective keel depth.

Table 4.4. Average shear strengths according to the assumed cylindrical failure mode in punch tests.

1998 **#**	τ (kPa)	**1999** **#**	τ (kPa)	**2000** **#**	τ (kPa)	**2001** **#**	τ (kPa)
1	7.4	2	18.6	0	18.1	1	1.9
2	12.5	6	32.0	3	8.6	2	6.5
		9	16.1	4	9.2		
		10	17.1				
		11	17.7				
average	10.0		20.3		12.0		4.2
average of all tests				13.8			

Average shear strengths varied largely from 4.2 to 20.3 kPa between different winters. The maximum 32.0 kPa in Test 6/1999 was almost double compared to other tests conducted during the same winter (16.1-18.6 kPa). It was difficult to make the cut during the winter of 1999, because up to six rafted layers of ice were observed in the consolidated layer. Extremely high shear strength in Test 6/1999 indicates that the cut was not properly made through the consolidated layer. Test 1/2001 represents a very thin keel in which the rubble was almost unconsolidated. One single force peak represented the global keel failure, but the load level was roughly equal to the buoyancy load while the platen was pushed down. A mild winter with short consolidation time explains the lower keel strength, especially in 2001 but also in 2000. In the winter of 1999 the ridges were well consolidated, having a thick consolidated layer consisting of several rafted layers (up to six layers, each 20 cm thick).

5 Material model

5.1 Rubble failure and deformation mechanisms

Ice rubble is a composition of discrete particles, blocks, that can move with respect to each other. A load applied to this kind of particulate system is transmitted by contact forces developed between adjacent blocks. The contact forces can be divided into normal and tangential components as shown in Fig. 5.1. The contact is frictional, i.e. the tangential force depends on the normal force. The dependency between the force components depends for example on the contact geometry and the existence of freeze bonds, while both of them depend on temperature history, sea currents etc. On a larger scale, the contact interaction phenomenon can be averaged over a representative volume. The overall strain in an average sense results partly from the deformations of individual ice blocks and partly from the relative sliding between the blocks.

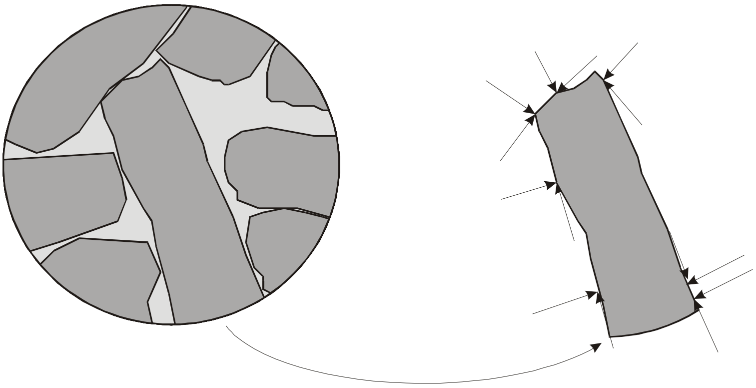

Figure 5.1. Contact forces between adjacent ice blocks in the keel. The forces are divided into normal and tangential components.

Several different mechanisms can be described for the ice rubble failure and deformation mechanisms. Ice rubble can fail by different mechanisms due to the complicated internal structure. The typical failure mechanisms are classified as follows:

1. Cohesive bonds between ice blocks fail due to shear or tensile forces.
2. Cohesive bonds fail due to hydrostatic pressure and rubble is compacted.
3. After bond failing, blocks can move relative to each other like granular frictional material. If hydrostatic pressure is very low or negative, ice blocks move easily without breaking.
4. Individual ice block failure due to bending or shearing. The block failure needs either intact bonds between the blocks or the hydrostatic pressure high enough to ensure that the force needed to break a block is transmitted from the surrounding blocks.
5. Individual block failure by crushing due to hydrostatic pressure or compression.

The deformation mechanism depends on the failure mechanism. They are classified in the following way.

1. When the hydrostatic pressure is high, rubble compacts during the failure process and the volume of ice rubble decreases.
2. In the case of individual ice block failure, one block splits into smaller blocks which are small enough to fill some of the cavities between larger ice blocks. The volume of ice rubble decreases.
3. Under low hydrostatic pressure the blocks are able to move and rotate causing volumetric expansion.

The observations made for rubble failure and deformation mechanisms build up the features needed in a macro-level material model. The major failure modes are shearing and compaction.

5.2 Comparison between discrete model and continuum model

Generally, there are two different strategies to simulate the constitutive behavior of granular assemblies: a discrete model and a continuum model. In the discrete model ice rubble is modeled as a granular assembly. Each individual ice block is modeled as a particle. The shape of a particle is approximated, the simplest one is a circle in the two-dimensional case and a ball in the three-dimensional case. The size of discrete elements may vary. Instead of stress and strain, the constitutive law is replaced by a contact law formulated in terms of contact forces and relative displacements. (Hopkins et al., 1999 and Løset, 1993).

Discrete models take into account the behavior of a single particle, while continuum models describe the material behavior of a volume of rubble in an average sense, in which the details of the rubble are smoothed out. The stress and strain fields are described by continuous functions. The examined volume of rubble must contain at least a certain number of ice blocks, which is not exactly known. Particle models are believed to provide further insight into complex microstructural phenomena, but the method itself is usually too expensive to model larger complex structures. Also, difficulties arise when modeling the geometry of the internal structure accurately and when modeling the contact phenomena. Therefore, a continuum model applied in finite element simulation is considered an appropriate alternative. (Kuhl et al., 2000).

5.3 Effective stress state

The principle of effective stress can be applied for dividing the total stress into two parts: the pore pressure and the effective stress (Lewis and Schrefler, 1998).

$$\sigma_{ij} = -u\delta_{ij} + \sigma'_{ij} \qquad ; \qquad \delta_{ij} = \begin{cases} 1 & ; \quad i = j \\ 0 & ; \quad i \neq j \end{cases} \tag{5.1}$$

where σ_{ij} is the stress, u is the pore pressure, δ_{ij} is kronecker delta and σ'_{ij} is the effective stress.

The load is carried through the skeleton structure of ice blocks, causing an effective stress state in the rubble. Individual block dilation due to pore pressure is insignificant in comparison to the dilatation and shearing in the skeleton structure of ice rubble. Because of high porosity, water inside the voids in the underwater part of rubble escapes during the slow loading process. However, if the loading rate is high the hydrodynamic loads have a greater contribution, causing changes in failure mechanisms and load pattern (Lemee and Brown, 2002). Target strain rates in full-scale measurements carried out in this work were slow enough to ignore the pore pressure effect. Hence, in the forthcoming study the pore pressure is assumed to be neglible and therefore the stress equals the effective stress. The use of the effective stress means that only the buoyancy forces affect the initial stress state in rubble, not the pressure caused by water in voids.

5.4 Strain decomposition

A constitutive law is defined to describe the dependency between the stress and the strain in a continuum. Usually, the strain is separated into parts. All of them describe different deformation mechanisms and they are taken to be independent of each other, i.e. there is no interaction between different deformation mechanisms. The strain tensor ε can then be introduced as a sum of the elastic strain ε^e (recoverable), the inelastic strain ε^{ie} and the damage strain ε^d.

$$\varepsilon_{ij} = \varepsilon_{ij}^{e} + \varepsilon_{ij}^{ie} + \varepsilon_{ij}^{d} \tag{5.2}$$

The first two terms in Eq. (5.2) describe the deformation mechanisms due to the block rearrangements. The first term ε^e also contains the elastic deformations of individual ice blocks. The damage strain describes the failing of an ice block, for example shearing, bending or crushing failure. In the sense of ice rubble, the individual ice block failure is defined as a damage of one point or part of the area/volume in the ice rubble.

Because it is difficult to separate the inelastic and damage strain components from each other, they are combined as a non-recoverable strain (plastic strain), i.e. $\varepsilon^p = \varepsilon^{ie} + \varepsilon^d$. Consequently, the strain includes only two different parts. A simplified model for the strain decomposition is then

$$\varepsilon_{ij} = \varepsilon_{ij}^{e} + \varepsilon_{ij}^{p} \tag{5.3}$$

The possibility of different kinds of non-recoverable deformation modes is taken into account by defining a proper criterion in the stress space, i.e. a combined locus for the damage and the block rearrangements. Because the mathematical description of the non-recoverable strain is similar to the plasticity theory, we also use the term plastic strain to describe the non-recoverable strain.

When the elastic deformations of ice rubble and solid ice are compared, one observes that the elastic deformations of individual ice blocks can be neglected. This means that inter-particle sliding is the major contributor to the strain. Also, the deformations are most likely permanent (Sayed et al., 1992). Therefore, the elastic contribution is less important for modeling.

The additive strain decomposition is valid even in the case of finite deformation if the following requirements are filled (ABAQUS Theory Manual, 2001):

1. the strain rate measure is the rate of deformation tensor ($\dot{\varepsilon}_{ij} = D_{ij}$)
2. the elastic strains are small.

The rate of deformation tensor D_{ij} is defined as a symmetric part of the velocity gradient.

$$D_{ij} = \frac{1}{2}\left(\frac{\partial v_i}{\partial x_j} + \frac{\partial v_j}{\partial x_i}\right) \tag{5.4}$$

where the velocity v_i of a material particle is defined according to Lagrangian viewpoint as a time derivative of the current spatial coordinates x_i.

$$v_i = \frac{\partial x_i}{\partial t} \tag{5.5}$$

Definition for stress and strain is described closer in Ch.6.

5.5 Stress and strain invariants

It is useful to present the constitutive laws by dividing the stress σ_{ij} and the strain ε_{ij} into deviatoric and dilatation parts. A hydrostatic pressure p is defined as

$$p = -\frac{1}{3}(\sigma_{11} + \sigma_{22} + \sigma_{33}) = -\frac{1}{3}\sigma_{kk} \tag{5.6}$$

and a deviatoric stress tensor s_{ij} is defined as

$$s_{ij} = \sigma_{ij} + p\delta_{ij} \tag{5.7}$$

The strain is divided into parts similarly.

$$\begin{aligned} e_{ij} &= \varepsilon_{ij} - \frac{1}{3}\varepsilon_{kk}\delta_{ij} \\ \varepsilon_{kk} &= \varepsilon_{\mathrm{vol}} = \varepsilon_{11} + \varepsilon_{22} + \varepsilon_{33} \end{aligned} \tag{5.8}$$

where e_{ij} is a deviatoric strain and $\varepsilon_{\mathrm{vol}}$ is a dilatation strain (a volumetric strain).

It is also useful to present other stress invariants. Using invariants the presentation of constitutive laws becomes shorter and they are independent of the co-ordinate system. The stress invariants can be written as

$$\begin{aligned} p &= -\frac{1}{3}\sigma_{kk} \\ q &= \sqrt{\frac{3}{2}s_{ij}s_{ij}} \\ r &= \left(\frac{9}{2}s_{ij}s_{jk}s_{ki}\right)^{1/3} \end{aligned} \tag{5.9}$$

where p corresponds to the first invariant of the stress tensor with a negative sign (the hydrostatic pressure), q is von Mises equivalent stress (the second invariant of the deviatoric stress tensor), and r is the third invariant of the deviatoric stress tensor. Constitutive laws are often written as a function of these three invariants as is seen later. The definition of invariants can be found in a slightly different form in other references.

5.6 Elastic deformations

Rubble can be treated as an elastic material when the load is low enough to cause any permanent damage to the rubble. The simplest model, the linear elastic model, can be written according to the Hooke's law (Belytschko et al., 2000).

$$\sigma_{ij} = C_{ijkl}\varepsilon^{\mathrm{e}}_{kl} \tag{5.10}$$

where C_{ijkl} is an elastic tensor containing two independent elastic constants: Young's modulus E and Poisson value ν.

$$C_{ijkl} = \frac{E}{2(1+\nu)}\left[\frac{2\nu}{1-2\nu}\delta_{ij}\delta_{kl} + \delta_{ik}\delta_{jl} + \delta_{il}\delta_{jk}\right] \tag{5.11}$$

The elastic constitutive relationship is often written as

$$p = -K\varepsilon^{\mathrm{e}}_{\mathrm{vol}} \qquad ; \qquad s_{ij} = 2Ge^{\mathrm{e}}_{ij} \tag{5.12}$$

or

$$\sigma_{ij} = K\varepsilon^{\mathrm{e}}_{\mathrm{vol}}\delta_{ij} + 2Ge^{\mathrm{e}}_{ij} \tag{5.13}$$

where K is a modulus of compressibility and G is a shearing modulus. The relation between different elastic quantities is

$$G = \frac{E}{2(1+\nu)} \qquad ; \qquad K = \frac{E}{3(1-2\nu)} \tag{5.14}$$

5.7 Plastic deformations

Plastic deformation occurs only when the yield condition $f = 0$ is met. The yield function f written by the stress invariants and internal variables, governs the onset and continuance of plastic deformations. The plastic strain $\varepsilon^{\mathrm{p}}_{ij}$ in rate form is given by a flow rule often specified in terms of a plastic flow potential function g

$$\dot{\varepsilon}_{ij}^{\mathrm{p}} = \lambda \frac{\partial g}{\partial \sigma_{ij}} \tag{5.15}$$

where λ is the plasticity multiplier. If the potential function is chosen equal to the yield function (i.e. $g = f$), the flow rule is called associative. For the associative rule, plastic flow is in the normal direction to the yield surface.

A consistency condition ensures that the stress state lies on the yield surface all the time, i.e. $\dot{f} = 0$. Evolution laws determined by the internal variables govern the yield surface evolution during plastic deformations.

5.8 Dissipation work and volumetric behavior

The rate of mechanical dissipation work $\dot{W}^{\mathrm{p}}$ can be decomposed into deviatoric and volumetric parts as follows:

$$\dot{W}^{\mathrm{p}} = \sigma_{ij}\dot{\varepsilon}_{ij}^{\mathrm{p}} = \dot{W}_{\mathrm{dev}}^{\mathrm{p}} + \dot{W}_{\mathrm{vol}}^{\mathrm{p}} \tag{5.16}$$

with

$$\dot{W}_{\mathrm{dev}}^{\mathrm{p}} = s_{ij}\dot{e}_{ij}^{\mathrm{p}} \quad ; \quad \dot{W}_{\mathrm{vol}}^{\mathrm{p}} = -p\dot{\varepsilon}_{\mathrm{vol}}^{\mathrm{p}} \tag{5.17}$$

Based on the dissipation work decomposition one might define a deviatoric strain rate quantity $\dot{\varepsilon}_{\mathrm{dev}}^{\mathrm{p}}$ which is a scalar quantity and the energy conjugate to the stress invariant q.

$$\dot{W}_{\mathrm{dev}}^{\mathrm{p}} = s_{ij}\dot{e}_{ij}^{\mathrm{p}} = q\dot{\varepsilon}_{\mathrm{dev}}^{\mathrm{p}} \tag{5.18}$$

Thus, the rate of mechanical dissipation work takes the form

$$\dot{W}^{\mathrm{p}} = q\dot{\varepsilon}_{\mathrm{dev}}^{\mathrm{p}} - p\dot{\varepsilon}_{\mathrm{vol}}^{\mathrm{p}} \tag{5.19}$$

Based on Eq. (5.18) and the definition for q in Eq. (5.9), one finds the following relation for the equivalent deviatoric plastic strain rate (Runesson, 1999):

$$\dot{\varepsilon}^{\mathrm{p}}_{\mathrm{dev}} = \sqrt{\frac{2}{3}\dot{e}^{\,\mathrm{p}}_{ij}\,\dot{e}^{\,\mathrm{p}}_{ij}} \qquad \textbf{(5.20)}$$

In the case of the associative flow rule, the volumetric plastic strain and equivalent deviatoric plastic strain can be defined by the yield function gradient in the invariant space (meridian space) (Runesson, 1999).

$$\dot{\varepsilon}^{\mathrm{p}}_{\mathrm{vol}} = -\lambda\frac{\partial f}{\partial p} \quad ; \quad \dot{\varepsilon}^{\mathrm{p}}_{\mathrm{dev}} = \lambda\frac{\partial f}{\partial q} \qquad \textbf{(5.21)}$$

The volumetric plastic strain represents the horizontal component of the yield surface gradient in the meridian plane, while the equivalent deviatoric plastic strain is the vertical component as shown in Fig. 5.2.

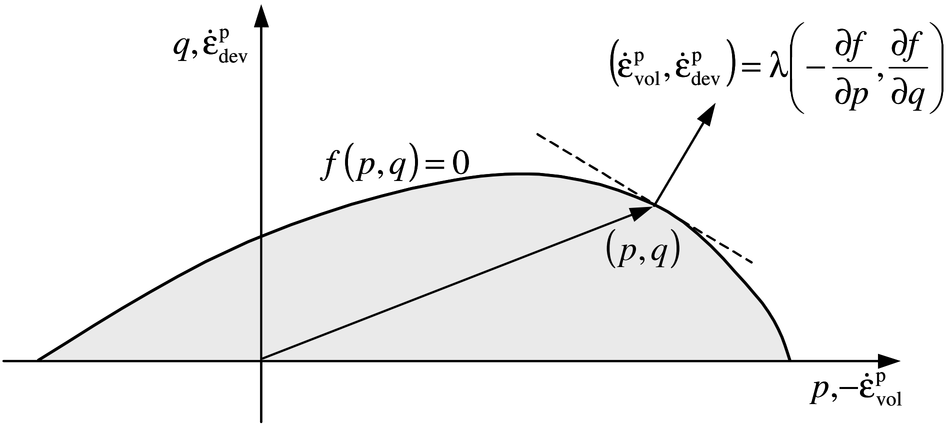

Figure 5.2. Gradient of the yield surface in the meridian plane.

5.9 Yield function

5.9.1 Mohr-Coulomb and Drucker-Prager

The material failure initiates when the stress state reaches the limit described by the yield function. Because the plastic deformations depend on the yield function in the case of the associative flow rule, the choice of the yield function is the most critical task in the material model.

One of the most common failure criteria for ice rubble is the Mohr-Coulomb criterion (MC), which is also very widely used in geotechnical engineering. The shear stress τ on the shear failure plane is modeled as

$$|\tau| = c - \sigma_n \tan\varphi \qquad \textbf{(5.22)}$$

where c is the cohesion and φ is the angle of internal friction, both of which are material parameters, and σ_n is the normal stress affecting the failure surface. The model gives a straightforward connection between the shear strength and the material parameters. Therefore, the MC model is useful in simpler computation models like limit load calculations.

However, because the yield envelope contains corners in the stress space shown in Fig. 5.3 (i.e. the gradient of the surface is not continuous), the MC model is not robust in numerical FE analysis without any modifications. In numerical analysis the Mohr-Coulomb yield function should be modified to smoothen out the sharp corners. The numerical implementation in ABAQUS fits well the original Mohr-Coulomb criterion by rounding the corners of the yield surface. One can rewrite the MC model in terms of principal stresses ($\sigma_1 \geq \sigma_2 \geq \sigma_3$) as following (ABAQUS/Standard User's Manual, 2001):

$$\sigma_1 - \sigma_3 + (\sigma_1 + \sigma_3)\sin\varphi - 2c\cos\varphi = 0 \qquad \textbf{(5.23)}$$

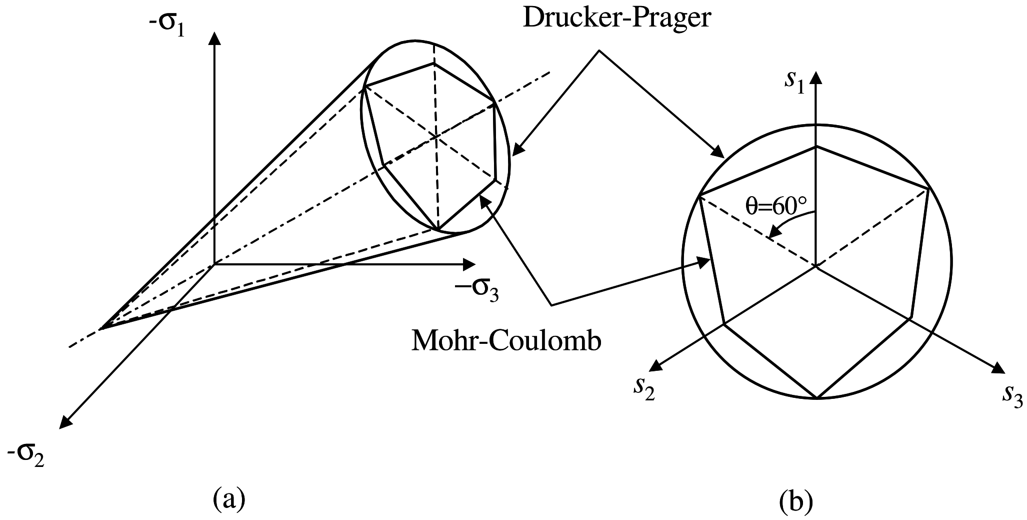

Figure 5.3. Drucker-Prager and Mohr-Coulomb yield surfaces matched along the compressive meridian (a) in principal stress space (b) in the deviatoric plane.

For general states of stress the Mohr-Coulomb model is more conveniently written in terms of three stress invariants as

$$f = R_{\text{mc}} q - p \tan\varphi - c = 0 \tag{5.24}$$

where

$$R_{\text{mc}}(\theta, \varphi) = \frac{\sin(\theta + \pi/3)}{\sqrt{3}\cos\varphi} + \frac{1}{3}\cos\left(\theta + \frac{\pi}{3}\right)\tan\varphi \tag{5.25}$$

where θ is the polar angle in the deviatoric plane (see Fig. 5.3). One can find value for θ from the following equation by using the stress invariants.

$$\cos 3\theta = \left(\frac{r}{q}\right)^3 \tag{5.26}$$

The Drucker-Prager model (DP) in Eq. (5.27) represents a similar shear criterion in the stress invariant space. It has been widely used to model frictional granular-like materials (soils etc.) that exhibit a pressure dependent yield. In the DP model the yield function has a linear relationship between the 2^{nd} deviatoric stress invariant q and the hydrostatic pressure p as shown in Fig. 5.4. To make difference between MC and DP parameters, cohesion in the MC model is c and the friction angle φ, while in the DP model the corresponding parameters are d and β.

$$f(p,q) = q - p\tan\beta - d = 0 \tag{5.27}$$

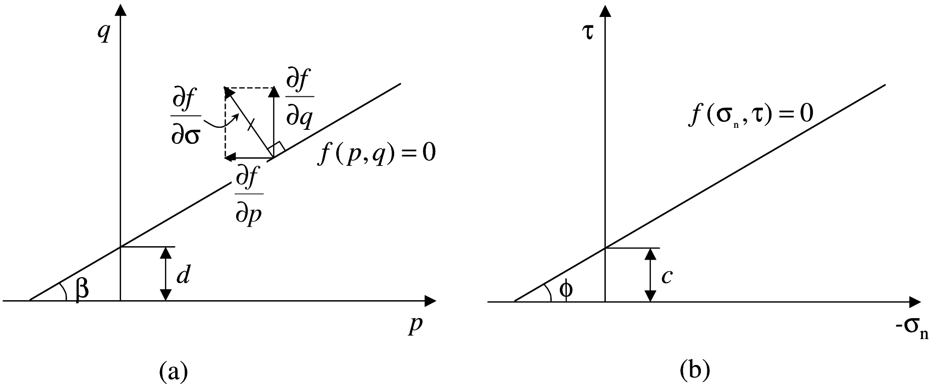

Figure 5.4. (a) Drucker-Prager stress criterion in the meridian plane and (b) Mohr-Coulomb stress criterion

The DP model is a smooth approximation of the MC criterion. The parameters are matched by adjusting the cone size in the DP criterion. The following relations are valid while matching the parameters along the compressive, tension or shear meridian plane, which means that the two yield surfaces are made to coincide along the chosen meridian, as shown in Fig. 5.3.

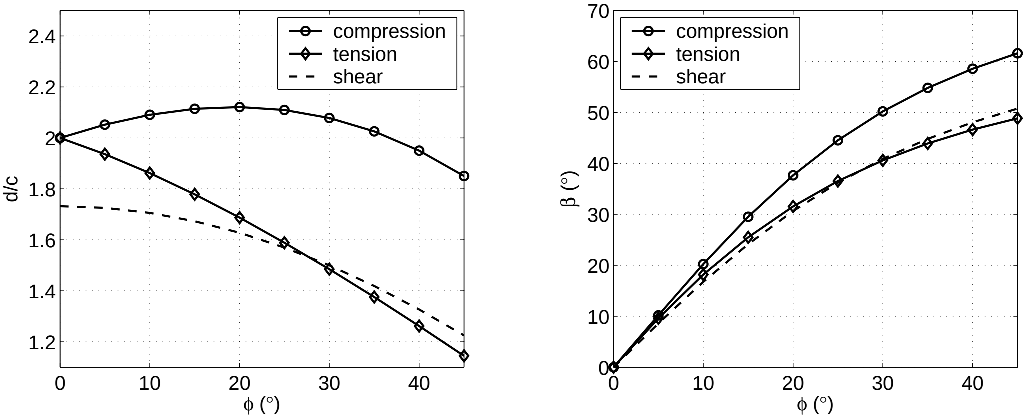

Figure 5.5. Relation between Drucker-Prager (d and β) and Mohr-Coulomb (c and φ) material parameters as a function of the friction angle in the MC model.

$$\tan\beta = \frac{6\sin\varphi}{3-\sin\varphi} \quad ; \quad d = \frac{6c\cos\varphi}{3-\sin\varphi} \quad ; \quad \text{compressive}$$

$$\tan\beta = \frac{6\sin\varphi}{3+\sin\varphi} \quad ; \quad d = \frac{6c\cos\varphi}{3+\sin\varphi} \quad ; \quad \text{tension} \tag{5.28}$$

$$\tan\beta = \sqrt{3}\sin\varphi \quad ; \quad d = \sqrt{3}c\cos\varphi \quad ; \quad \text{shear}$$

Because the parameter matching is valid only in the chosen stress state, the parameters in different models cannot be compared exactly in the general stress analysis in which the stress state characteristic varies arbitrarily.

The most important observation in these cohesive-frictional models MC and DP is that the material expands continually during plastic deformations. Also, the dilatation during shear failure depends on the friction angle, i.e. a higher friction angle results in more expansion. Only the elastic part of the deformation provides compaction. The dilatation is the most questionable feature in the classical cohesive-frictional models (MC or DP). Of course, one can adjust the dilatation behavior with a non-associative flow rule, but the compaction failure cannot be modeled that way.

5.9.2 Shear-cap criterion

Because the dilatation is not modeled correctly in the classical models (MC and DP), the yield criterion must be modified to take the volumetric behavior and the compaction failure into account as well. By adding a cap yield surface to the shear criterion (DP for instance), one bounds the yield surface in hydrostatic compression. This cap yield criterion with volumetric hardening controls the dilatation while material fails either by shearing or by compaction.

To make numerical simulations easier to converge, a smooth yield function is created by combining two elliptical yield surfaces together, one for the shear failure and one for the cap failure describing the compaction failure. The model is similar to that found in ABAQUS developed for modeling geological materials. However, the numerical stability of the modified Drucker-Prager model in ABAQUS is not acceptable in the case of low hydrostatic pressure while the tension stresses dominate. Therefore, the modified Drucker-Prager model is developed further to cover a larger range of hydrostatic pressure.

The yield function for the shear failure is

$$f_s = \sqrt{[(p-p_a)\tan\beta]^2 + q^2} - (d + p_a\tan\beta) \qquad ;\ p \le p_a \tag{5.29}$$

and the yield function for the cap failure is

$$f_c = \sqrt{(p-p_a)^2 + (Rq)^2} - R(d + p_a\tan\beta) \qquad ;\ p > p_a \tag{5.30}$$

where d and β are the corresponding Drucker-Prager parameters for cohesion and friction. R defines the cap shape and p_a describes the pressure that divides the shear and cap failure parts as shown in Fig. 5.6. One observes that the volumetric component of the yield surface gradient results in expansion in the shear failure region and compaction in the cap part.

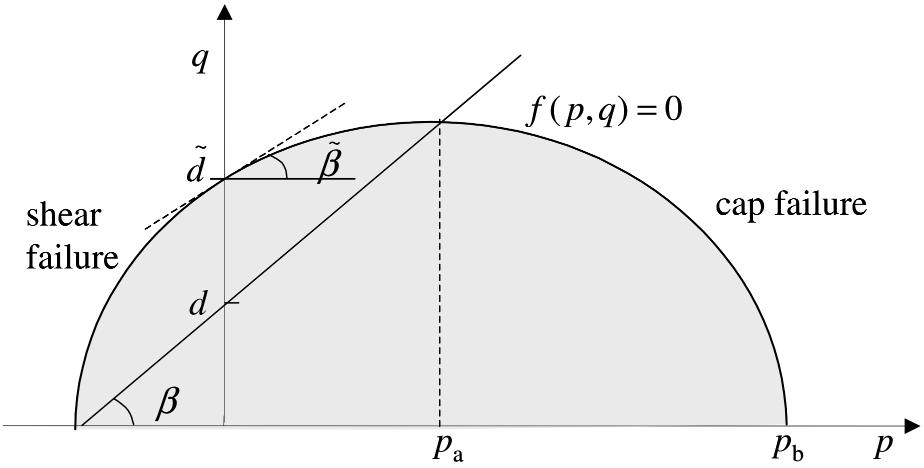

Figure 5.6. Shear-cap yield function in the meridian plane.

Although the corresponding Drucker-Prager parameters describe the yield function, they are not real cohesion and friction angle. To define the value of q and corresponding tangent ($\mathrm{d}q/\mathrm{d}p$) from the yield function at zero pressure, one describes cohesive-frictional behavior physically. This is worth defining while comparing the results with other cohesive-frictional material models. Therefore, the physical parameters, $\tilde{d}$ and $\tilde{\beta}$ are defined in Eq. (5.31) and a graphical interpretation is shown in Fig. 5.6.

$$\tilde{d} = \sqrt{d(d + 2p_\mathrm{a}\tan\beta)} \; ; \qquad \tan\tilde{\beta} = \frac{p_\mathrm{a}\tan^2\beta}{\tilde{d}} \qquad \textbf{(5.31)}$$

5.10 Evolution laws of the shear-cap yield surface

5.10.1 Cap hardening

The material softens during the shearing failure process, while the shearing causes dilatation and the rubble becomes looser. This is the case, when the hydrostatic pressure is less than p_a. During the cap failure process the material hardens, while individual ice blocks are compressed due to the hydrostatic pressure ($p>p_a$) and inter-particle contact forces increase. Therefore, the material hardening law should be defined by the dilatation behavior with the volumetric plastic strain as a hardening variable.

The model is based on observations in the small-scale experiments. The void ratio e depends on the pressure p according to a logarithmic law (Wong et al. 1990, Sayed et al. 1992)

$$\mathrm{d}e = -\lambda \mathrm{d}(\ln p) \tag{5.32}$$

where λ is a material parameter. The relation between the void ratio and the hydrostatic pressure is modified further to contain the volumetric strain instead of the void ratio. Therefore, the cap hardening law for p_b in Fig. 5.6 is expressed as (Lewis and Schrefler, 1998)

$$p_b = p_0 \exp\left(\frac{-(\varepsilon^{p}_{vol} - \varepsilon^{p}_{vol}|_0)}{\kappa_0} \right) \tag{5.33}$$

where p_0 describes the hydrostatic pressure and $\varepsilon^{p}_{vol}|_0$ the volumetric plastic strain at the reference state (subscript 0). κ_0 is a material parameter containing information on e_0 and λ ($\kappa_0 = \lambda/(1+e_0)$). The corresponding cap hardening curve is presented in Fig. 5.7.

The hardening variable in the yield function is p_a, which is defined from the compatibility requirement of two yield functions f_s and f_c (ABAQUS/Standard User's Manual, 2001)

$$p_a = \frac{p_b - Rd}{1 + R\tan\beta} \tag{5.34}$$

According to the cap hardening law, hardening or softening of material depends only on the volumetric plastic strain. The size of the yield surface is controlled by adjusting the material parameter p_a, which depends on p_b according to Eq. (5.34). When the stress state lies on the cap side ($p > p_a$), the volumetric plastic strain is negative and the ice rubble is compacted. While the rubble is compacted, the yield surface grows. Correspondingly, when the stress state lies on the shear failure side ($p < p_a$), the volume increases causing the yield surface to shrink. The effect of volumetric plastic strain is shown in Fig. 5.7.

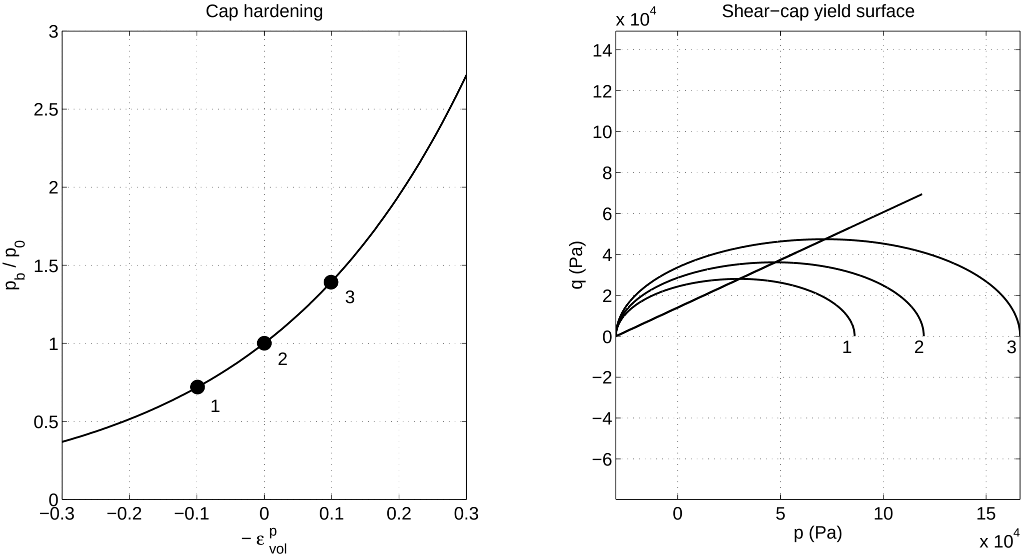

Figure 5.7. Cap hardening curve described by normalized hydrostatic pressure vs. the volumetric plastic strain. Corresponding points indicate the change of size of the yield surface shown on the right.

5.10.2 Cohesive softening

The cohesive strength of rubble decreases during ice block failure as well as during bond failure. This is modeled by the strain softening law, in which the state of the equivalent deviatoric plastic strain describes the cohesive strength state according to exponential law.

$$d = d_0 \exp\left(\frac{-\varepsilon^{\mathrm{p}}_{\mathrm{dev}}}{\varepsilon_{\infty}}\right) \tag{5.35}$$

where d_0 describes the initial cohesive strength. ε_{∞} describes how fast the cohesion decreases, and $\varepsilon^{\mathrm{p}}_{\mathrm{dev}} = \varepsilon_{\infty}$ is the strain level corresponding to cohesion $d = 0.37d_0$. The evolution law for cohesive softening and the effect for the yield surface are shown in Fig.5.8.

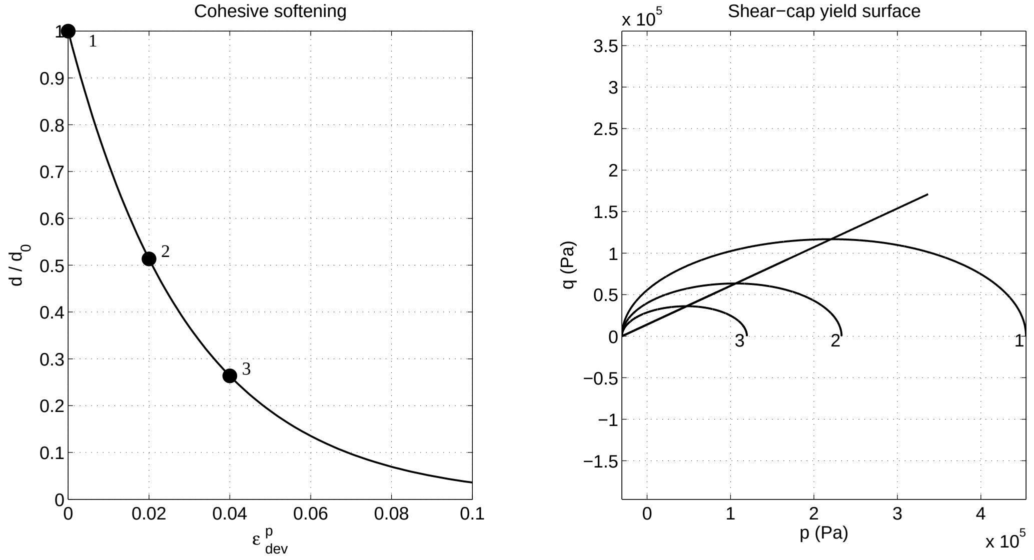

Figure 5.8. Cohesive softening curve normalized with the initial value vs. the equivalent deviatoric plastic strain. Corresponding points indicate the yield surface shrinkage shown on the right.

5.11 Constitutive law

A constitutive law determines the relation between stress and strain. As described earlier, the strain rate tensor $\dot{\varepsilon}_{ij}$ is divided into two parts, elastic and plastic.

$$\dot{\varepsilon}_{ij} = \dot{\varepsilon}^{\mathrm{e}}_{ij} + \dot{\varepsilon}^{\mathrm{p}}_{ij} \tag{5.36}$$

The variables in the yield function are the stress tensor and internal force vector q_{i}.

$$f(\sigma_{ij}, q_i) = 0 \tag{5.37}$$

The stress tensor σ_{ij} is a function of the strain (total strain ε_{ij}) and the plastic strain $\varepsilon^{\mathrm{p}}_{ij}$. The quantity q_{i} contain parameters p_{a} and d in the yield function , i.e. $\mathbf{q} = (p_{\mathrm{a}}, d)$, which depend on the internal state variables $\boldsymbol{\alpha} = (\varepsilon^{\mathrm{p}}_{\mathrm{vol}}, \varepsilon^{\mathrm{p}}_{\mathrm{dev}})$ (hardening variables). Let us formulate the yield function as

$$f(\sigma_{ij}, p_{\mathrm{a}}, d) = 0 \tag{5.38}$$

The loading and unloading conditions are stated by the Kuhn-Tucker complementary condition, which requires that

$$\begin{gathered} \lambda \geq 0 \ , \qquad f(\sigma_{ij}, q_i) \leq 0 \\ \text{and} \\ \lambda f(\sigma_{ij}, q_i) = 0 \end{gathered} \tag{5.39}$$

The first term indicates that the multiplier in the plastic strain is non-negative. The second term indicates that the stress state must always lie on or within the yield surface. The last condition requires that the stress state must lie on the yield surface during plastic loading while $\lambda>0$. The last condition is stated as the consistency condition requiring that $\dot{f} = 0$.

Therefore, by differentiating the yield function one finds

$$\dot{f} = \frac{\partial f}{\partial \sigma_{ij}}\dot{\sigma}_{ij} + \frac{\partial f}{\partial p_{\mathrm{a}}}\dot{p}_{\mathrm{a}} + \frac{\partial f}{\partial d}\dot{d} = 0 \tag{5.40}$$

The stress rate is written according to the Hooke’s law.

$$\dot{\sigma}_{ij} = C_{ijkl}\dot{\varepsilon}^{\mathrm{e}}_{kl} = C_{ijkl}\left(\dot{\varepsilon}_{kl} - \lambda\frac{\partial g}{\partial \sigma_{kl}}\right) \tag{5.41}$$

where definitions of the strain rate decomposition (Eq. (5.36)) and the flow rule (Eq. (5.15)) are applied. C_{ijkl} is the elastic tensor containing two independent elastic constants (see Eq. (5.11)).

The evolution laws for internal hardening variables are defined as

$$\dot{d} = \frac{\partial d}{\partial \varepsilon^{\mathrm{p}}_{\mathrm{dev}}} \dot{\varepsilon}^{\mathrm{p}}_{\mathrm{dev}} \tag{5.42}$$

and

$$\dot{p}_{\mathrm{a}} = \frac{\dot{p}_{\mathrm{b}} - R\dot{d}}{1 + R\tan\beta} = \frac{1}{1 + R\tan\beta}\left(\frac{\partial p_{\mathrm{b}}}{\partial \varepsilon^{\mathrm{p}}_{\mathrm{vol}}} \dot{\varepsilon}^{\mathrm{p}}_{\mathrm{vol}} - R \frac{\partial d}{\partial \varepsilon^{\mathrm{p}}_{\mathrm{dev}}} \dot{\varepsilon}^{\mathrm{p}}_{\mathrm{dev}} \right) \tag{5.43}$$

Inserting Eqs. (5.41), (5.42) and (5.43) into Eq. (5.40), we get the final form for the consistency condition.

$$\begin{aligned} \dot{f} = {} & \frac{\partial f}{\partial \sigma_{ij}} C_{ijkl}\left(\dot{\varepsilon}_{kl} - \lambda \frac{\partial g}{\partial \sigma_{kl}} \right) + \\ & + \frac{\partial f}{\partial p_{\mathrm{a}}} \frac{1}{1 + R\tan\beta}\left[\frac{\partial p_{\mathrm{b}}}{\partial \varepsilon^{\mathrm{p}}_{\mathrm{vol}}}\left(-\lambda \frac{\partial g}{\partial p} \right) - R \frac{\partial d}{\partial \varepsilon^{\mathrm{p}}_{\mathrm{dev}}} \lambda \frac{\partial g}{\partial q} \right] + \\ & + \frac{\partial f}{\partial d} \frac{\partial d}{\partial \varepsilon^{\mathrm{p}}_{\mathrm{dev}}} \lambda \frac{\partial g}{\partial q} = 0 \end{aligned} \tag{5.44}$$

λ is then solved

$$\lambda = \frac{\dfrac{\partial f}{\partial \sigma_{ij}} C_{ijkl} \dot{\varepsilon}_{kl}}{\dfrac{\partial f}{\partial \sigma_{ij}} C_{ijkl} \dfrac{\partial g}{\partial \sigma_{kl}} + \dfrac{\partial f}{\partial p_{\mathrm{a}}} \dfrac{1}{1 + R\tan\beta}\left(\dfrac{\partial p_{\mathrm{b}}}{\partial \varepsilon^{\mathrm{p}}_{\mathrm{vol}}} \dfrac{\partial g}{\partial p} + R \dfrac{\partial d}{\partial \varepsilon^{\mathrm{p}}_{\mathrm{dev}}} \dfrac{\partial g}{\partial q} \right) - \dfrac{\partial f}{\partial d} \dfrac{\partial d}{\partial \varepsilon^{\mathrm{p}}_{\mathrm{dev}}} \dfrac{\partial g}{\partial q}} \tag{5.45}$$

One could rewrite the evolution laws for hardening in a general form as

$$\dot{q}_k = -\lambda h_k \tag{5.46}$$

where h_k is the hardening function. The constitutive law is now written from Eqs.

(5.45) and (5.41)

$$\dot{\sigma}_{ij} = C_{ijkl}\dot{\varepsilon}^{\mathrm{e}}_{kl} = C^{\mathrm{ep}}_{ijkl}\dot{\varepsilon}_{kl} \tag{5.47}$$

where the constitutive tensor for plastic deformations is

$$C^{\mathrm{ep}}_{ijkl} = C_{ijkl} - \frac{\dfrac{\partial f}{\partial \sigma_{mn}} C_{mnkl} C_{ijop} \dfrac{\partial g}{\partial \sigma_{op}}}{\dfrac{\partial f}{\partial \sigma_{mn}} C_{mnop} \dfrac{\partial g}{\partial \sigma_{op}} + \dfrac{\partial f}{\partial q_k} h_k} \tag{5.48}$$

The associative flow rule ($g = f$) was applied in all shear-cap model simulations presented in Ch. 7. Therefore, the constitutive tensor remains symmetric.

6 Numerical implementation into ABAQUS/Standard

6.1 General

ABAQUS/Standard is a general-purpose finite element program providing nonlinear analysis, in which the equilibrium statement is written in a Lagrangian viewpoint from the principle of virtual work.

$$\int_V \sigma_{ij} \delta\dot{\varepsilon}_{ij} \mathrm{d}V = \int_S t_i \delta v_i \mathrm{d}S + \int_V b_i \delta v_i \mathrm{d}V \tag{6.1}$$

where σ_{ij} and ε_{ij} are any conjugate pairing of stress and strain, δ indicates virtual differences, v_j is the velocity, t_i is the traction acting on the surface S and b_i is the body force at any point within the considered volume V. Updated Lagrangian description is adopted in the case of finite deformation, in which all variables are referred to the current configuration at time t. A kinematic relation between the velocity v_j and strain ε_{ij} used in ABAQUS/Standard was defined in Eq. (5.4).

In static analysis in which inertia forces are ignored, the implicit solver finds a solution for following nonlinear equilibrium equations derived from the virtual work principle:

$$\begin{aligned} \mathbf{F} &= \mathbf{f}^{\mathrm{ext}} - \mathbf{f}^{\mathrm{int}} = 0 \\ \mathrm{d}\mathbf{F} &= \mathbf{K}(\mathbf{u})\mathrm{d}\mathbf{u} \end{aligned} \tag{6.2}$$

where $\mathbf{F}$ is the nodal force vector, $\mathbf{f}^{\mathrm{ext}}$ is the sum of the external forces defined by the right side in Eq. (6.1), $\mathbf{f}^{\mathrm{int}}$ describes the internal forces defined by the left side in Eq. (6.1), $\mathbf{u}$ contains nodal displacements (u_x, u_y and u_z) and $\mathbf{K}$ is the tangential stiffness matrix. The displacement approximation ($\tilde{u}_i$) in the element method is interpolated from the nodal solution by shape functions.

$$\tilde{\mathbf{u}} = \mathbf{N}\mathbf{u} \tag{6.3}$$

where $\mathbf{N}$ contains the shape functions. Deformations measured by the strain are determined from displacements as

$$d\boldsymbol{\varepsilon} = \mathbf{B}(\mathbf{u})\,d\mathbf{u} \qquad \textbf{(6.4)}$$

where **B** is called a kinematic matrix defining the kinematic relation based on the shape functions. In the case of large deformations, **B** depends on the displacements and the equilibrium equations become geometrically nonlinear. Also, the formulation of **B** depends on the definition for the strain (Green-Lagrange or logarithmic, for instance).

From a virtual work approach, the stiffness matrix can be written as follows:

$$\mathbf{K} = \int_V \mathbf{B}^T \mathbf{C} \mathbf{B}\, dV \qquad \textbf{(6.5)}$$

where the integration is taken over by the element volume *V*. **C** is the constitutive tensor in matrix form. In the nonlinear analysis, the stiffness matrix is presented in a tangential form ($\mathbf{K} = d\mathbf{F}/d\mathbf{u}$).

6.2 UMAT subroutine in ABAQUS/Standard

The user can apply his/her own material model in ABAQUS/Standard by writing a user material subroutine (UMAT) in Fortran language (F77). Only the constitutive relation needs to be determined. All other computation routines are provided by ABAQUS/Standard. The values of the following variables are passed into UMAT:

- the time and time increment
- the stress
- the strain and the strain increment
- the user-defined solution-dependent state variables (STATEV)
- the predefined field variables, the temperature, the deformation gradient etc.

They define the state at the beginning of the time increment (the state at the end of the previous increment). In the UMAT subroutine the user has to update following quantities:

- the new stress state (Eq. (6.8) in Ch. 6.4)
- the material Jacobian matrix (DDSDDE) at the end of time increment (Eq. (6.10) in Ch. 6.4)
- the user defined solution dependent state variables (STATEV) (for intance hardening parameters)

The material Jacobian matrix (DDSDDE) is a part of the tangential stiffness matrix used for estimation of the next increment in the iteration of the nonlinear force balance equation. The user may also define energy quantities, for instance the dissipation energy.

6.3 Stress and strain definitions

A definition for stress and strain becomes important when the material undergoes finite deformations. The stress and strain measures are based on the definitions used in ABAQUS/Standard resulting in a conjugate pairing of stress and strain used in Eq. (6.1). Considering equilibrium in the current configuration, one finds the Cauchy stress (often called as “true” stress) as a compatible stress measure for the rate of deformation tensor ($\dot{\varepsilon}_{ij} = D_{ij}$). The internal work rate can be expressed in terms of the Kirchhoff’s stress τ_{ij} as

$$\int_V \sigma_{ij}\dot{\varepsilon}_{ij}\mathrm{d}V = \int_{V^0} \tau_{ij}\dot{\varepsilon}_{ij}\mathrm{d}V^0 \qquad \textbf{(6.6)}$$

where $J=\mathrm{d}V/\mathrm{d}V_0$ is the ratio of the material volume in the current and reference configurations. σ_{ij} is chosen as the Cauchy stress which is a direct measure of the traction carried by the current unit area. The Cauchy and Kirchhoff’s stresses are identical for an incompressible material. The Kirchhoff’s stress is useful in the development of constitutive models for materials undergoing large volume changes considering geometric non-linearity. It is the work conjugate to the strain defined from the rate of deformation tensor D_{ij} with respect to the volume in the reference configuration (ABAQUS Theory Manual, 2001). Therefore, the relationship between the Cauchy and Kirchhoff’s stresses is

$$\tau_{ij} = J\sigma_{ij} \qquad \textbf{(6.7)}$$

The strain passed into UMAT subroutine is defined as the integral of the rate of deformation tensor. This is actually non-trivial in a general case especially if the principal axes of the strain rotate during the deformation. The integration over the time increment is constructed by the central difference algorithm according to Hughes-Winget method (Hughes and Winget, 1980). Because the strain is referred to a fixed coordinate system, all the components are rotated to account for the rigid body motion that occurs during the increment. The strain defined from the rate of deformation tensor requires that the elastic strain is small compared to unity. This also means that the strain rate decomposition is valid, $\dot{\varepsilon}_{ij} = \dot{\varepsilon}^{\mathrm{e}}_{ij} + \dot{\varepsilon}^{\mathrm{p}}_{ij}$ (ABAQUS Theory Manual, 2001).

6.4 Stress integration

New values of the state variables (σ_{ij}, $\varepsilon^{\mathrm{p}}_{ij}$, q_i) are obtained by integrating the constitutive equations over an incremental strain history with given initial conditions. The new stress state at time t_1 is

$$\sigma_{ij}(t_1) = \sigma_{ij}(t_0) + \int_{t_0}^{t_1} C^{\mathrm{ep}}_{ijkl}\dot{\varepsilon}_{kl}\,\mathrm{d}t \qquad \textbf{(6.8)}$$

A frequently used family of stress integration algorithms is based on the generalized trapezoidal rule (NAFEMS, 1992). A discrete formulation can be written as

$$\begin{aligned} (\Delta\sigma_{ij})_{n+1} &= C_{ijkl}\big((\Delta\varepsilon_{kl})_{n+1} - (\Delta\varepsilon^{\mathrm{p}}_{kl})_{n+1}\big) \\ (\Delta\varepsilon^{\mathrm{p}}_{ij})_{n+1} &= \Delta\lambda\left[(1-\alpha)\left(\frac{\partial f}{\partial\sigma_{ij}}\right)_n + \alpha\left(\frac{\partial f}{\partial\sigma_{ij}}\right)_{n+1}\right] \\ f(\sigma_{ij}, q_i)_{n+1} &= 0 \end{aligned} \qquad \textbf{(6.9)}$$

where α is a parameter ranging from 0 to 1.The subscript *n* describes the state at the beginning of the time increment and *n+1* at the end of the time increment. By choosing α = 0, the method remains explicit known as the *Forward Euler* integration scheme. However, in that case the stable strain increment becomes too short for failure modeling applications. By choosing $\alpha = 1$, the integration scheme becomes implicit, requiring local iterations. The method is known as *Backward Euler* incrementation, providing a stable algorithm.

A cutting-plane algorithm was chosen for the stress integration scheme in UMAT (Simo and Hughes, 1998). It is a variation of general return-mapping algorithms based on Backward Euler incrementation. The computation scheme is shown in Box 1. The plastic strain $\varepsilon_{ij}^{\mathrm{p}}$, internal hardening parameters ($\varepsilon_{\mathrm{vol}}^{\mathrm{p}}, \varepsilon_{\mathrm{dev}}^{\mathrm{p}}$) and forces ($p_{\mathrm{a}}$, d) were chosen for solution-dependent state variables (STATEV). The algorithm is based on the strain (total strain ε) and the strain increment ($\Delta\varepsilon$) given at the beginning of each time increment.

The geometric interpretation is shown in Fig. 6.1. A trial state based on the elastic predictor is first found in each time increment. Thereafter, in each iteration the stress state approaches the yield surface along a linearized path. The direction of each stress jump in cuts is normal to the current yield surface.

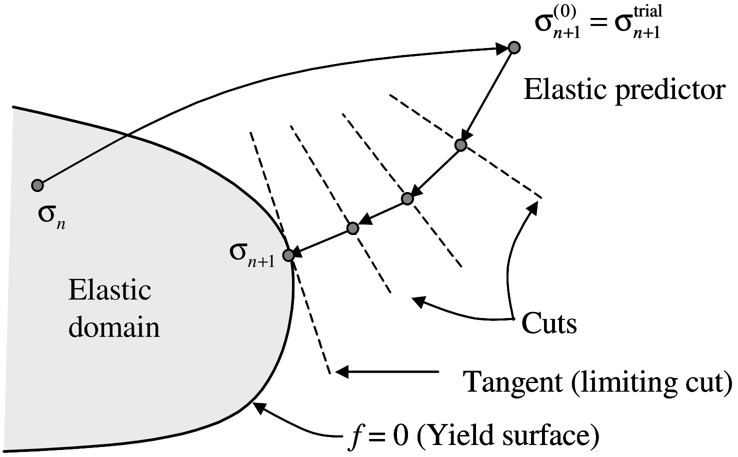

Figure 6.1. Geometric interpretation of the cutting-plane algorithm.

Box 1. *General convex cutting-plane algorithm (Simo and Hughes, 1998).*

```
1   Initialize   $k = 0, \quad \boldsymbol{\varepsilon}^{\mathrm{p}^{(0)}}_{n+1} = \boldsymbol{\varepsilon}^{\mathrm{p}}_{n}, \quad \boldsymbol{\alpha}^{(0)}_{n+1} = \{(\varepsilon^{\mathrm{p}}_{\mathrm{vol}})_n, (\varepsilon^{\mathrm{p}}_{\mathrm{dev}})_n\}, \quad \Delta\lambda^{(0)}_{n+1} = 0$
2   Compute stresses, internal forces and yield function
        $\boldsymbol{\sigma}^{(k)}_{n+1} = \mathbf{C}\left(\boldsymbol{\varepsilon}_{n+1} - \boldsymbol{\varepsilon}^{\mathrm{p}^{(k)}}_{n+1}\right)$
        $\boldsymbol{q}^{(k)}_{n+1} = q(\boldsymbol{\alpha}^{(k)}_{n+1})$
        $f^{(k)}_{n+1} = f(\boldsymbol{\sigma}^{(k)}_{n+1}, \boldsymbol{q}^{(k)}_{n+1})$
3   IF   $f^{(k)}_{n+1} < TOL$
        THEN EXIT
    ELSE
        Compute increment to plastic consistency parameter
        $\Delta\lambda^{(k)}_{n+1} = \dfrac{f^{(k)}_{n+1}}{\left(\dfrac{\partial f}{\partial \boldsymbol{\sigma}}\right)^{(k)}_{n+1} \mathbf{C} \left(\dfrac{\partial f}{\partial \boldsymbol{\sigma}}\right)^{(k)}_{n+1} + \left(\dfrac{\partial f}{\partial \boldsymbol{q}}\right)^{(k)}_{n+1} \boldsymbol{h}^{(k)}_{n+1}}$
        Update state variables
        $\boldsymbol{\varepsilon}^{\mathrm{p}^{(k+1)}}_{n+1} = \boldsymbol{\varepsilon}^{\mathrm{p}^{(k)}}_{n+1} + \Delta\lambda^{(k)}_{n+1} \left(\dfrac{\partial f}{\partial \boldsymbol{\sigma}}\right)^{(k)}_{n+1}$
        $\boldsymbol{\alpha}^{(k+1)}_{n+1} = \{(\varepsilon^{\mathrm{p}}_{\mathrm{vol}})^{(k+1)}_{n+1}, (\varepsilon^{\mathrm{p}}_{\mathrm{dev}})^{(k+1)}_{n+1}\} = \alpha\left(\varepsilon^{\mathrm{p}^{(k+1)}}_{n+1}\right)$
        SET $k = k+1$ AND GOTO 2
    ENDIF
```

When the solution for the stress state is valid, the user has to define the constitutive matrix at the end of each time increment. This is done for the main FE-program to create the global tangential stiffness matrix (Eq. (6.5)), which is needed for estimating the next increment when solving the global nonlinear balance equations.

While the material undergoes large volume changes because pressure-dependent yield and geometric nonlinearity are considered, the exact definition of the consistent material matrix (Jacobian) is given by (ABAQUS/Standard User's Manual, 2001)

$$\mathbf{C} = \frac{1}{J}\frac{\partial\Delta(J\boldsymbol{\sigma})}{\partial\Delta\boldsymbol{\varepsilon}} \qquad \mathbf{(6.10)}$$

This definition agrees with Kirchhoff's stress measure.

The convergence of the global equilibrium equations depends strongly on the material Jacobian. Instead the exact consistent material matrix, the constitutive matrix at the end of each time increment was evaluated for approximation of the material Jacobian. The cutting-plane algorithm with the simplified Jacobian is programmed straightforwardly providing robust computations but the convergence rate remains linear. Usually the consistent material matrix improves the convergence rate to quadratic. The stability limit for the strain increment is usually large enough.

7 Simulation of full-scale tests by FEM

7.1 General

Numerical simulations of the punch test were made by a commercial finite element program ABAQUS/Standard. The shear-cap material model was applied by the user material subroutine (UMAT). Reference data was created by simulations with Mohr-Coulomb (MC) and Drucker-Prager (DP) material models. The parameters in the material models were calibrated by comparing the FEM simulations with the full-scale experimental tests.

Because both the keel geometry and the internal structure are complicated, the model was simplified. The keel geometry was approximated to be even and to continue far away from the loading point. Both the rubble and the consolidated layer were approximated to be homogeneous. Because the keel was loaded with the circular platen, both the loading and geometry are axisymmetric. This kind of 2-dimensional axisymmetric model reduces the number of degrees of freedom remarkably, providing cost-effective simulation of how damage proceeds in the keel and also how the material parameters affect both the rubble strength and the failure mode. Moreover, the geometry and loading, the failure mode in the keel will also be symmetric. It was observed in the experiments that the platen did not tilt significantly during pushdown, supporting the axisymmetric approximation. Therefore, axisymmetric analysis was assumed to be valid.

Temperature of ice blocks in submerged rubble was considered constant and therefore the temperature dependency can be ignored. Also, all material properties were considered constant throughout the keel.

As time dependent deformation mechanisms were not included in the material model, the loading rate was prepared to gain the strain rate between two extreme cases:

- A slow strain-rate, approximately below 10^{-3} s^{-1}, leads to creep deformation as mentioned in Ch. 2.1.
- Pore water pressure build-up during a rapid loading, resulting in high

strain-rate. However, this is assumed to be negligible because of high porosity levels in ice rubble (between 27% and 42% in the 1999 and 2000 (Table 4.3)).

Only static analyses were conducted to simulate the punch tests. Inertia forces and damping effects were ignored. Dynamic analysis is needed to simulate the energy release from steel wire ropes in the post peak region. Therefore, the main argument in the calibration of material parameters was to simulate the maximum load correctly. Comparison between experimental and numerical data is not accurate in the post peak region.

A numerical uncertainty analysis was restricted to the element mesh dependency study (Ch 7.4).

7.2 Finite element model

The finite element model simulating the punch test is presented in Fig. 7.1. The keel was divided into two layers, the ice rubble and the consolidated layer. The keel geometry was simplified and modeled by first order axisymmetric solid elements (CAX3 and CAX4). The thickness of both layers was constant averaged from the drilling results.

The consolidated layer behaves like an elastic material. The elastic modulus was determined from the laboratory tests (compression tests) (Heinonen et al., 2000(a) and Heinonen and Määttänen, 2000(b)). The second layer underneath, the rubble, was assumed to be homogeneous in which the parameters did not have any spatial variation.

Symmetric boundary conditions were applied at the center line. The far end boundary conditions were modeled by using infinity elements (CINAX4). These elements kill the displacements at the far end (in the radial axis). This kind of boundary condition means that the keel is assumed to continue in the radial (horizontal) direction.

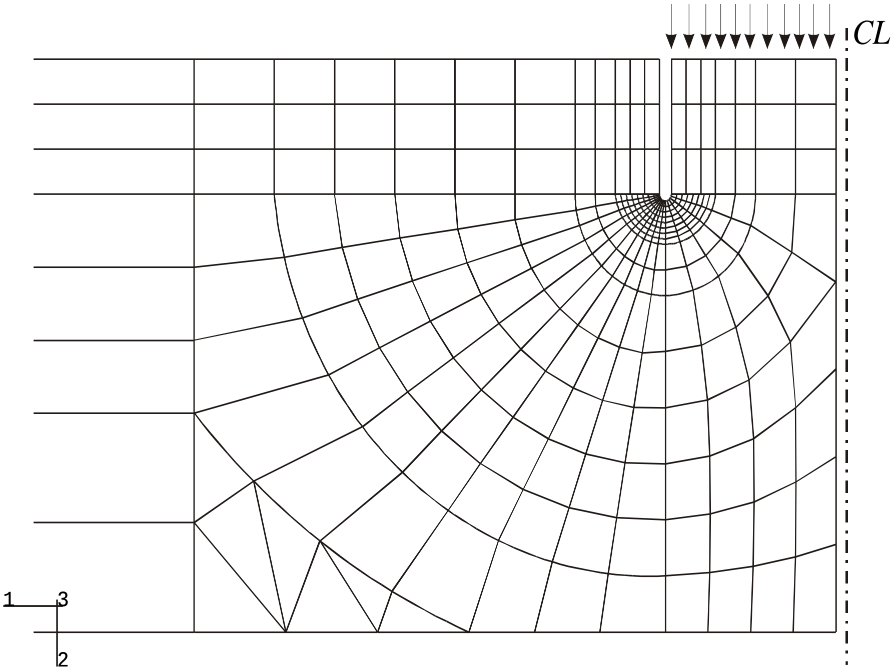

Figure 7.1. Axisymmetric finite element model of the punch shear test.

The analysis contained two steps. In the first, the initial stress state inside the keel due to the buoyancy was solved. The upper surface of the consolidated layer was fixed to avoid top layer displacements in the first step. The average volume force γ due to buoyancy in the rubble is

$$\gamma = (\rho_w - \rho_i)(1 - \eta)\,g = \rho_r\,g \qquad \textbf{(7.1)}$$

where ρ_w is the density of water and ρ_i is the density of the ice blocks. η is the rubble porosity and g is the gravitative acceleration ($g = 9.81$ m/s^2). ρ_r is apparent rubble density.

The platen was pushed down in the second step. The load was applied by forcing the platen downwards controlling the displacement. When the platen moves downwards, some water is replaced and the buoyancy increases. Therefore, an additional hydrostatic pressure dependent on the displacement was added at the bottom surface of the consolidated layer including the platen.

$$p = k\rho_w g u_z \qquad \textbf{(7.2)}$$

where u_z is the platen displacement in the vertical direction. k is a parameter describing the volume fraction which is replaced ($k = 1$ before the ice plate is totally submerged, after that wooden beams between the circular ice plate and the steel loading plate were submerged, in that case $k < 1$).

When the platen was pushed downwards, the shear stress concentrated under the edge of the platen and the shear strain accumulated in a narrow area at the beginning. In this kind of shear concentration the strain might be localized and the solution becomes dependent on the element mesh, both element size and alignment. To decrease the effects of the discretization a fine mesh was created under the gap becoming coarser at the deeper level. Curvilinear elements were applied to give several possibilities for the mesh guided localized zone to proceed. Different meshes between the parts, the consolidated layer and the keel as well as between the consolidated layer and the platen, were connected with a tied contact. That feature creates constraint equations between the nodes, forcing equal displacements in the contact surfaces.

Altogether five test cases from 1999 and 2000 were chosen for the numerical simulations (Table 4.2).

7.3 Calibration of material parameters

7.3.1 General

The parameters in the material model were calibrated by comparing the FEM simulations with the full-scale experimental tests.

The material constitutive parameters are divided into three categories:

- Elastic properties describe the linear part at the start of push down.
- The initial yield surface is determined by parameters d_0, β, p_a and R. They describe predominantly the punch load capacity.
- Hardening laws, i.e. cohesive softening and cap hardening, describe how the damage proceeds inside the keel and therefore determine the post peak load response.

To obtain reliable parameters, some of them were evaluated from other studies and some features were simplified to decrease the number of needed parameters and possible parameter combinations.

First, the Poisson value was chosen equal to 0.3, which is a typical value for a material composed of particles (Harr, 1977). Numerical testing was needed for evaluation of the elastic modulus.

Second, it was assumed that the initial hydrostatic pressure strength p_0 (cap pressure) depends on the initial cohesion. Wong et al. (1990) carried out small-scale experimental tests to find out the constitutive relation between the pressure p, the 2nd deviatoric stress invariant q and the void ratio. Corresponding the initial porosity (0.4) one finds that

$$\frac{p_0}{d_0} = 8.55 \qquad \textbf{(7.3)}$$

The sensitivity of p_0 / d_0 ratio is studied by parametric analysis in Ch. 7.3.12.

Third, the parameters for the cohesive softening and cap hardening were approximated to be equal ($\varepsilon_\infty = \kappa$).

Fourth, the first approximation for the hardening parameter based on Wong's paper was $\kappa = 0.3$, and this was further justified from the post peak response in full-scale tests. Numerical testing indicated that the hardening parameter must be much lower to simulate the post peak softening correctly. Therefore, $\kappa = 0.03$ was chosen for parametric simulations. Different types of ice, block shape and size distribution and loading condition also account for the different evaluation between full-scale and small-scale parameters. Due to uncertain evaluation, parametric analyses were made to study the effect of the hardening parameter (see Ch. 7.3.10).

Fifth, the volumetric plastic strain at the reference state ($\varepsilon^{\mathrm{p}}_{\mathrm{vol}}|_0$) in the cap evolution law was ignored. Thus the hardening laws were simplified in the following form:

$$d = d_0 \exp\left(\frac{-\varepsilon^{\mathrm{p}}_{\mathrm{dev}}}{\kappa}\right) \quad ; \quad p_{\mathrm{b}} = p_0 \exp\left(\frac{-\varepsilon^{\mathrm{p}}_{\mathrm{vol}}}{\kappa}\right) \qquad \textbf{(7.4)}$$

Sixth, numerical testing indicated that a low value for the cap side shape factor R caused too much volumetric compaction during the plastic deformations on the cap side. That was avoided by a shallower yield function on the cap side, which was created with a larger value of the shape factor. Therefore, the cap side shape factor R was approximated equal to 2. Due to uncertain evaluation, parametric analyses were conducted to study the effect of the cap shape parameter (see Ch. 7.3.11).

These simplifications allow us to model the rubble with two elastic parameters (E and ν) and with four plastic parameters (d_0 and β, p_0/d_0, κ), in which parameters ν, p_0/d_0 and κ were evaluated above. Thus, one elastic and two plastic state parameters need to be evaluated in parametric analyses. The fixed parameters are summarized in Table 7.1.

Table 7.1. Fixed material properties of rubble used in the numerical full-scale simulations.

Parameter	ν	R	p_0/d_0	κ
Value	0.3	2	8.55	0.03

Number of FEM analyses for each test case were needed to find reliable parameters that simulate correctly the measured load-displacement curve and the displacement field in the keel.

7.3.2 Load response

The load response in punch tests was discussed in Ch. 4. It was observed that pushdown force first increased almost linearly before the rubble underneath started to fail. When load capacity was achieved, the keel started to soften and the force decreased while the rubble failed further until the residual frictional strength was achieved (Fig. 7.2). Some small load-drops due to individual ice block failure were measured during the load-increasing phase. This kind of local damage cannot be simulated in an axisymmetric continuum model. The first large drop after the peak load was a consequence of global skeleton failure, including some dynamic effect due to the strain energy released from the steel wire ropes. In the numerical simulations, all rapid load-drops were smoothed out.

Numerical testing was needed for evaluation of the elastic modulus of rubble that was calibrated to fit the linear part of the load-displacement curve before the peak load (Table 7.2). Therefore, the elastic modulus can be evaluated independently of the plastic stage parameters. Actually, the elastic modulus determined the scale of the keel displacement. Parameter variation ensured that an elastic modulus chosen in the questionable range did not have an effect on the load capacity.

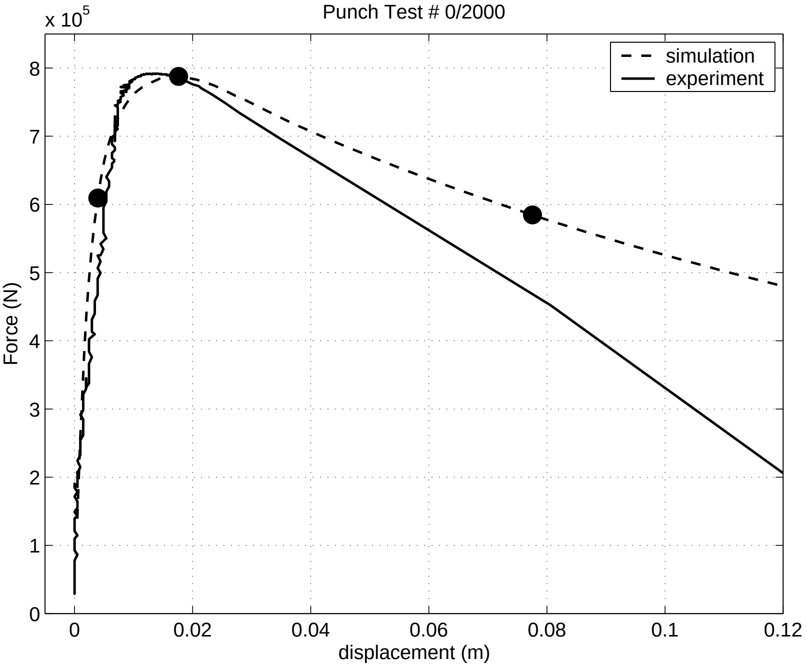

Figure 7.2. Load-displacement curve from both simulation and experiment in punch test 0/2000. Dots indicate different loading phases chosen for closer study.

Table 7.2. Elastic modulus of rubble used in numerical full-scale simulations.

Test #	0/2000	3/2000	4/2000	10/1999	11/1999
E (MPa)	100	48	22	120	100

A rather large variation was found for the elastic modulus (from 22 to 120 MPa). Some variation is described with the different consolidation and the internal stress state. In particulate media with rather high porosity (up to 40 %), the material itself is loose and the stiffness depends on the pressure state. This could be taken into account by applying a porous elastic model instead of Hooke's law. In addition, the preparation in the field, for instance the manually defined circular cut depth, could cause some variations to the keel stiffness.

The corresponding Drucker-Prager parameters, initial cohesion d_0 and the friction angle β, were left for the variation to adjust the maximum force (the load capacity). It should be noted that the hardening parameter κ was primarily adjusted to simulate softening in the post peak domain, but it also has an effect on the load capacity, as demonstrated in Ch. 7.3.10.

7.3.3 Stress state in the keel

The failure mode is determined by the stress state characteristic, which depends both on the loading and boundary conditions and on the keel geometry as well. The keel floats in water and it is fixed to the surrounding ice field. During vertical loading downwards, the buoyancy produces a flexible support. The thickness of the keel defines the bending stiffness. However, because the elastic modulus of the solid ice is much higher than that of the rubble, the bending stiffness is composed mainly of the consolidated layer. During the vertical punch load, the keel fails by shearing and possibly by compaction. However, to what extent bending of the flexural foundation is significant depends on the bending stiffness.

Hydrostatic pressure distributions at the time of maximum load are presented in Figs. 7.3 and 7.4 to demonstrate the effect of the keel thickness. Only the rubble part of the keel is shown. Two cases are selected: a thick keel Test 0/2000 and a thin keel Test 3/2000. The darker blue area in the contour plots indicates the hydrostatic tension. The pressure distribution along the vertical line under the cap is shown in Fig. 7.5. Most of the volume under the platen in both cases undergoes hydrostatic compression, causing this part to fail both by shearing and compaction. Due to the hydrostatic tension, the keel bottom fails by shearing according to the cohesive strength. However, all simulations indicated that the failure always begins at the upper part of the keel, never at the bottom due to tensile failure caused by the bending deformation.

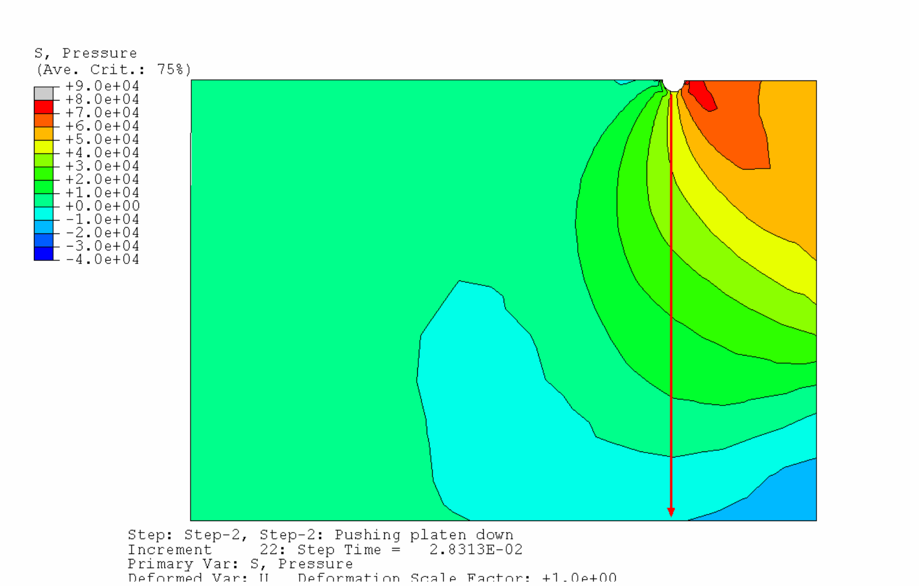

Figure 7.3. Pressure distribution in a thick keel at the time of maximum load (Test 0/2000). Blue area indicates a negative pressure. Red line indicates a path for pressure distribution in Fig. 7.5.

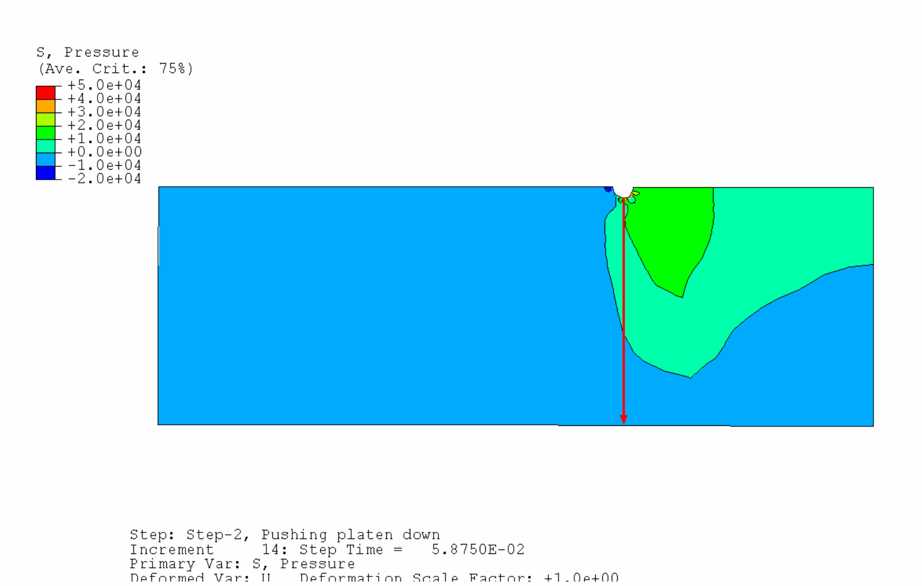

Figure 7.4. Pressure distribution in a thin keel at the time of maximum load (Test 3/2000). Blue area indicates a negative pressure. Red line indicates a path for pressure distribution in Fig. 7.5.

The thinner keel has a larger tension zone at the bottom. Also, the friction angle has a slight effect on that as shown in Fig. 7.5. The higher the friction angle is, the stronger and also stiffer the upper part of rubble becomes due to the cap hardening phenomenon moving also the neutral plane downwards.

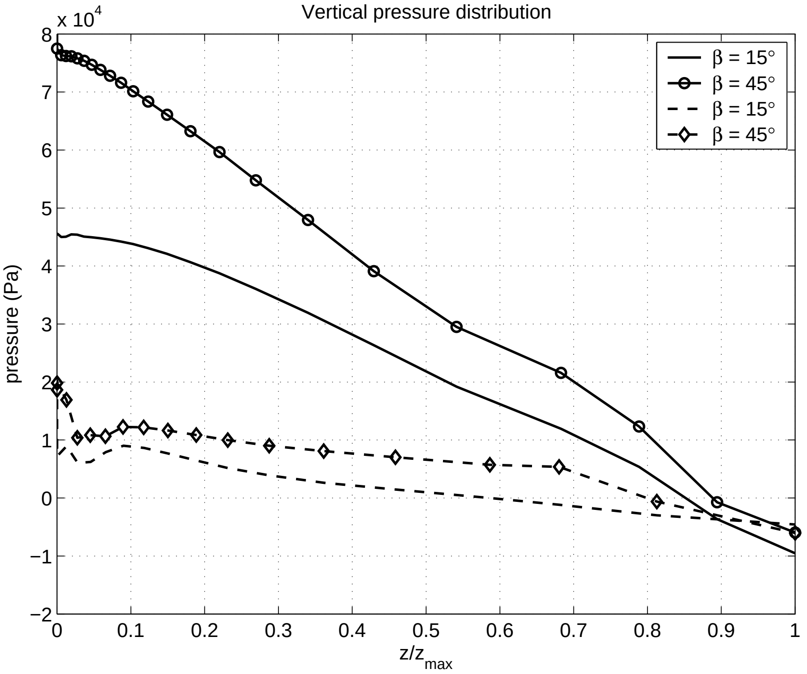

Figure 7.5. Hydrostatic pressure distribution with different friction angles in the vertical direction under the gap. Continuous lines represent the thicker keel (0/2000) and dashed lines the thinner one (3/2000).

7.3.4 Dilatation and failure mode

The failure mode depends on the dilatation and therefore on the friction angle. This dilatation phenomenon has a significant effect on the failure mechanism and the deformation field. It differs from the pure cohesive-frictional material which is clearly observed in the punch test simulations.

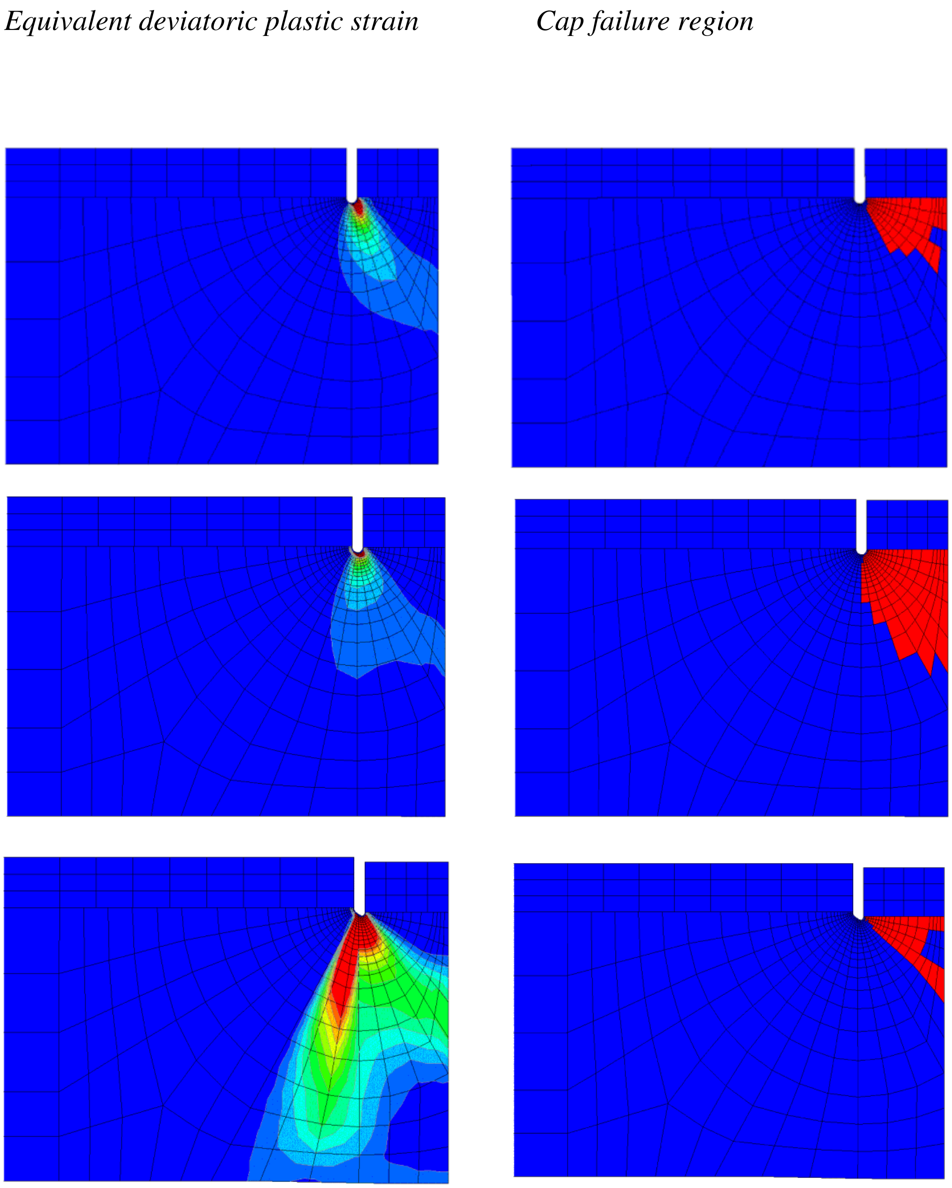

Figure 7.6. Failure distributions in the keel at different times (from top: before peak load, at peak load and after peak load). On the left: deviatoric plastic strain invariant; on the right: region of cap failure. $d_0 = 14$ *kPa and* $\beta = 25\,°$.

The failure progression is measured by the field variables. The volumetric plastic strain characterizes the rubble compaction and the equivalent plastic deviatoric strain characterizes the shear failure phenomenon. Fig.7.6 shows the failure distributions during punch loading at different times. Corresponding points in the load-displacement curve are shown in Fig. 7.2. In the load-increasing phase, cap failure occurs under the platen. At the same time the shear failure described by the deviatoric plastic strain invariant takes place mostly at the boundary of the cap failure area, starting from the bottom of the circular cut. As loading continues, the cap failure region enlarges and the shear failure zone proceeds further, turning at the same time towards the vertical plane. The maximum load capacity is therefore a combination of the shear failure and the cap failure. Thereafter, when the keel starts to collapse, the cap region area decreases. At the boundary zone of the cap failure area, the failure mode turns from compaction to shear as pushdown loading continues. Due to the volumetric expansion during shear failure, the shear failure zone spreads outwards, finally creating a conical plug punched through the keel. During that softening phase, the compacted area is small.

Failure progression in the keel and the relation between the failure modes depend strongly on the friction angle. With a low friction angle, shear failure dominates and compaction is insignificant. As the friction angle increases, the compaction phenomenon becomes more significant and the region of the compacted area increases. This was observed for all simulated punch tests. The effect of the internal friction angle is shown in Fig. 7.7, where the compacted area is plotted at the time of the maximum load for different friction angles.

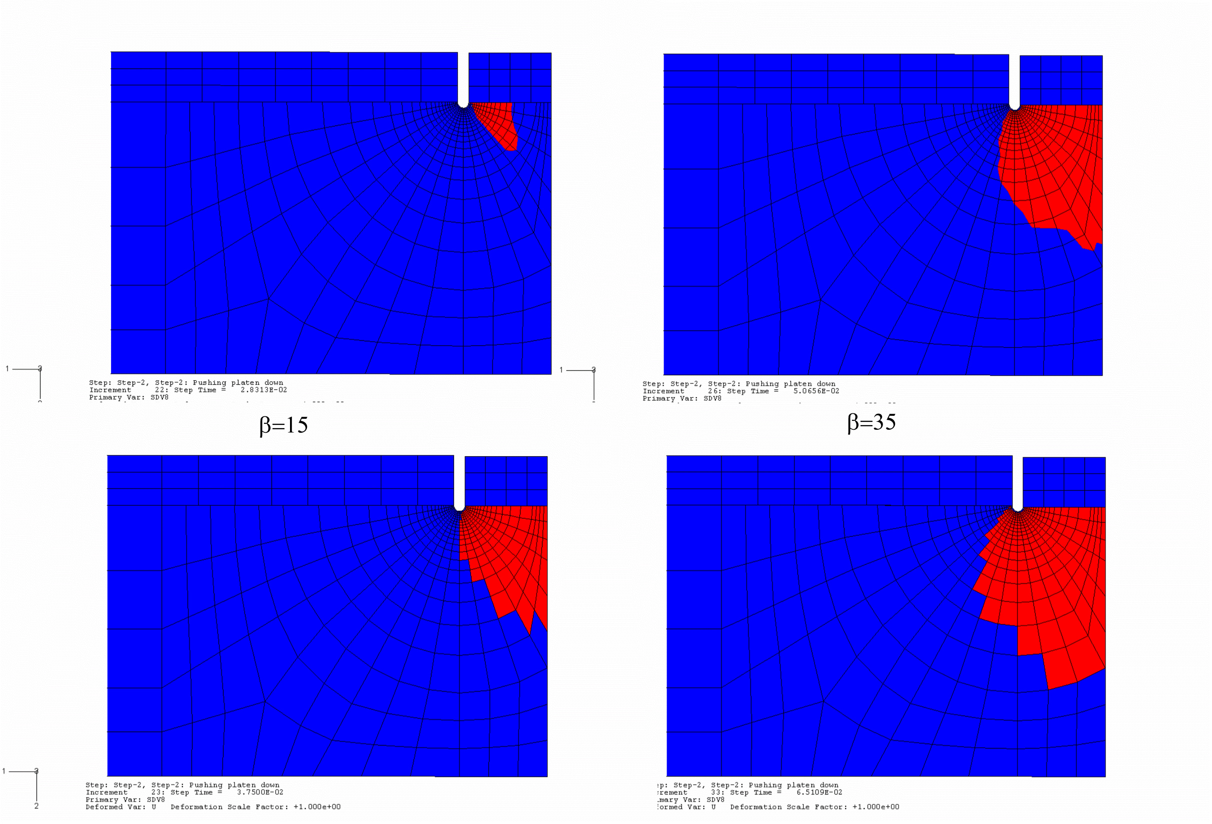

β=15 β=35

β=25 β=45

Figure 7.7. Cap failure region for different friction angles at maximum load.

As seen in Fig. 7.6, the final plug punched through the keel is approximately conical. The cone angle is small and increases slightly when β increases from 15° to 25° (Fig. 7.8). Increasing the friction angle above 25°has an insignificant effect on the shear failure progression. Larger friction causes more compaction in the region under the platen. Therefore, some material flows towards the compacted region instead of outwards. Hence the conical shear failure zone does not incline further outwards, although the friction angle is higher.

A conical shear failure mode is typical for cohesive-frictional material (Heinonen, 1999). For the Mohr-Coulomb and Drucker-Prager models the cone angle of the failure plane depends strongly on the friction angle. A larger friction angle results in a larger cone angle. The shear failure zone in the shear-cap model is usually wider than in cohesive-frictional material models, at least in the case of a larger friction angle (Fig. 7.9).

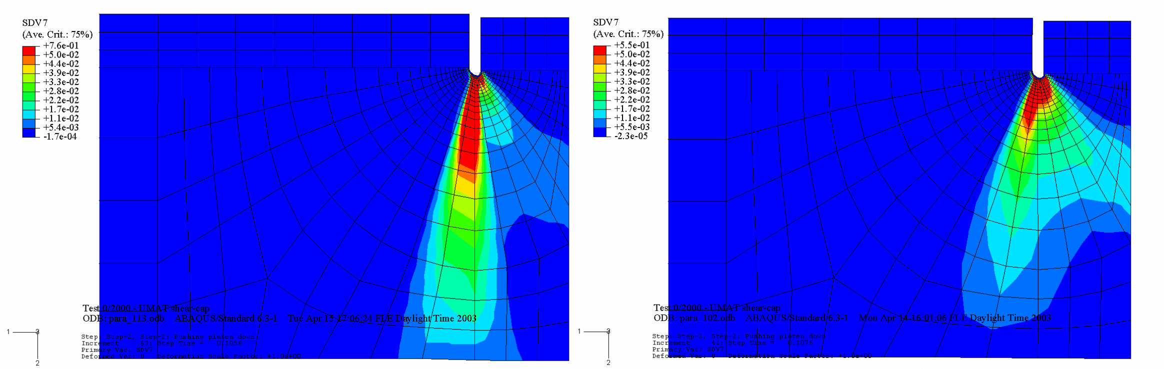

β=15 β=35

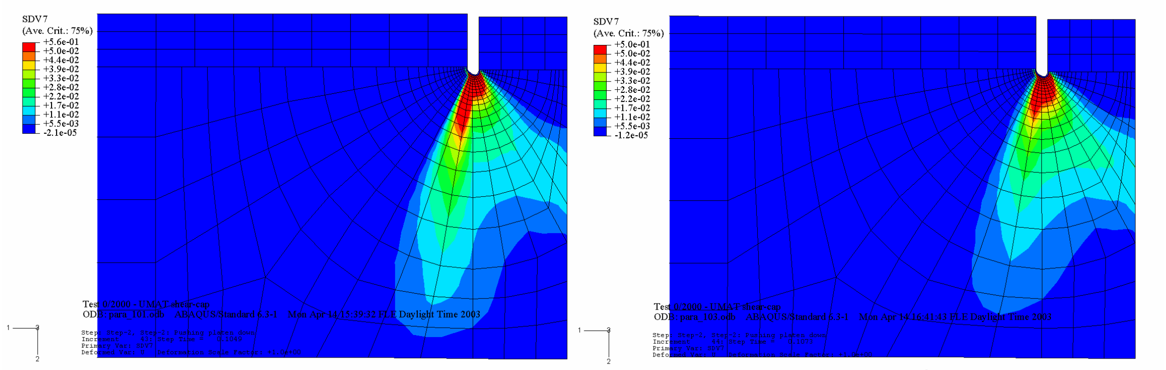

β=25 β=45

Figure 7.8. Deviatoric plastic strain invariant distribution for different friction angles in the softening phase (u = 0.05 m)

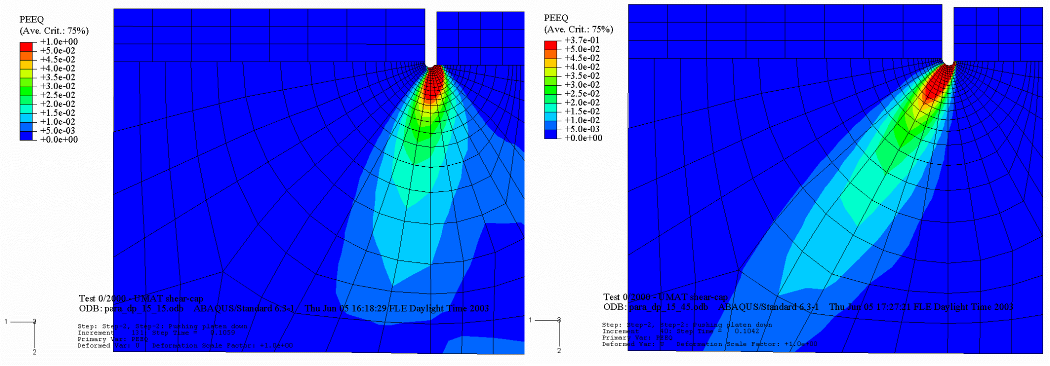

β = 15°

β = 45°

Figure 7.9. Equivalent plastic strain distribution for different friction angles simulated with the Drucker-Prager material model (u = 0.05 m).

7.3.5 Parameter analysis for the shear-cap criterion

A dependency between the corresponding Drucker-Prager parameters, d_0 and β, was found by varying both the initial cohesion and the friction angle. The load-displacement curve in Test 0/2000 for different friction angles is presented in Fig. 7.10.

The maximum force increases as the cohesion or friction angle increases. Softening depends mainly on the friction angle because the softening parameter itself was fixed. Two different cases can be described:

Case 1: The friction angle is low (below 25°):

The keel collapses more sharply when the friction angle is low. The shear failure is more likely because the stress state in most material points lies on the shear failure side as shown in Fig. 7.11. Therefore, the compaction failure has a minor role. In this case the rubble softens due to the cohesive softening mechanism. Because the horizontal component of the yield surface gradient is low, volumetric expansion is low. Therefore, softening on the cap side is insignificant. The deviatoric part of the plastic strain (proportional to cos β) describes most of the deformations. Compaction failure can occur only at points where the stress state is very close to the hydrostatic pressure (p/q > 1/tan β).

Case 2: The friction angle is high (over 25°):

With higher friction angles the keel does not really soften, because the compaction failure mechanism becomes more important. The cap failure criterion is achieved first in the large area. During cap failure the material hardens instead of softens. At the points where shear failure occurs, a large amount of rubble dilatation results only if the pressure is negative. Otherwise, the material expands only very slightly, because the yield surface in that region is flat and the gradient points upwards have a very small horizontal component.

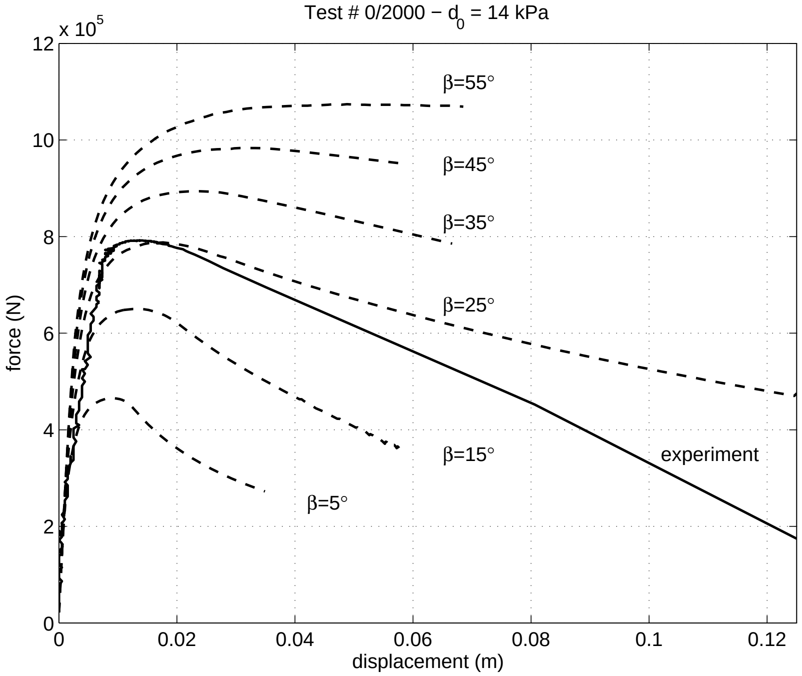

Figure 7.10. Load-displacement curves in Test 0/2000 with different friction angles.

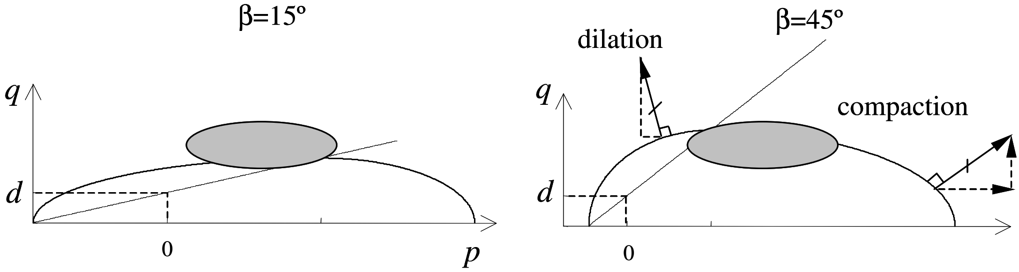

Figure 7.11. Yield surfaces in meridian plane for the friction angle $\beta=15$ °on the left and $\beta=45$ ° on the right. Other parameters are kept constant. The shaded areas characterize typical stress states in the keel during punch tests.

Volumetric expansion has two effects. First, during the load-increasing phase, the hydrostatic pressure increases due to confinement of the surrounding material, resulting in more frictional strength. Also, the stress state is moving close to the cap part and the failure mode turns from shearing to plastic compaction. The opposite effect was observed in the post peak phase, where the cap failure region decreased, causing the failure mode to shift from compaction to shear.

By plotting the maximum force versus cohesion and the measured load capacity in the same plot (Fig. 7.12), cross points can be found between the simulated and the measured lines representing admissible combinations of cohesion and the friction angle for each test case.

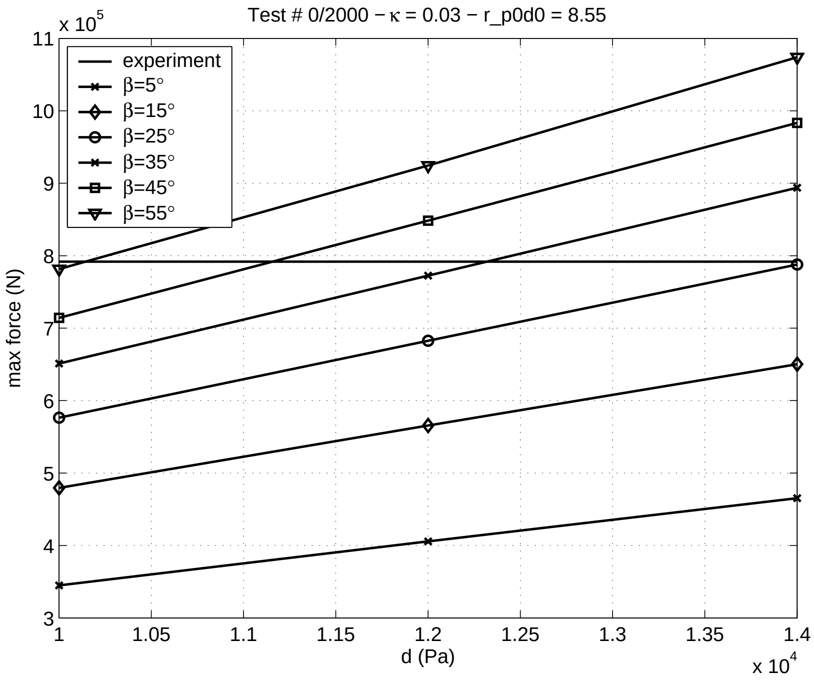

Figure 7.12. Maximum force in Test 0/2000 versus corresponding initial cohesion with different values for the internal friction angle.

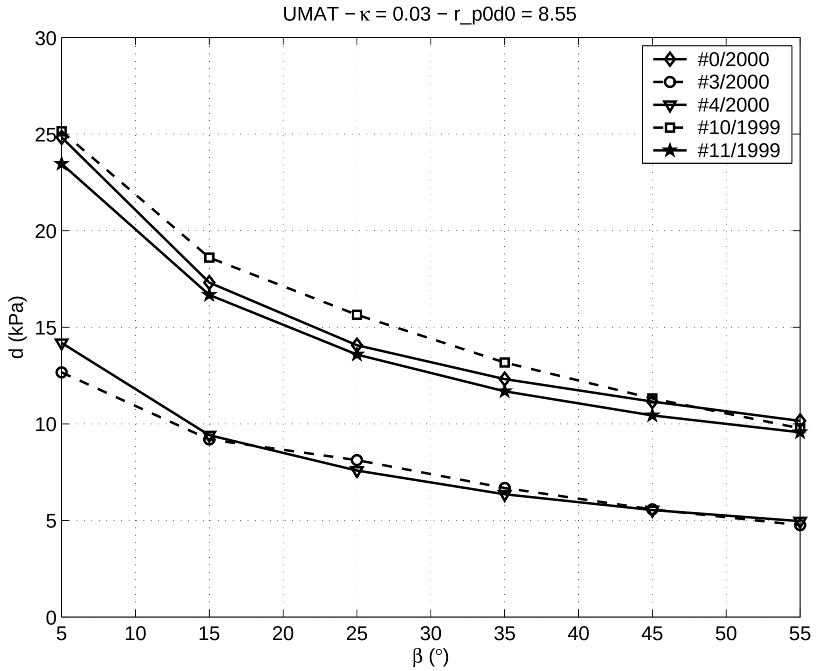

Figure 7.13. Curve describing possible combinations of the corresponding cohesion and internal friction angle.

Admissible parameter combinations for predicting the ridge load capacity correctly with the shear-cap model are shown in Fig. 7.13. In all cases the dependency on the friction angle is similar. Because the rubble strength is a combination of the cohesive and the frictional strength, the larger friction angle results in lower cohesion to simulate the same punch load. Some of the cases gave similar results among themselves, but there are two groups. Cohesion was approximately double in cases 0/2000, 10/1999 and 11/1999 compared to cases 3 and 4 in the year 2000.

Because admissible parameter combinations are based on the pushdown force and platen displacement, more information is needed to evaluate the parameters from the admissible parameter combination curves. A softening part of the load-displacement curve indicates that the friction angle should be less than 50° otherwise the load does not decrease from the maximum level. Parameter evaluation is continued by studying the keel deformations(Chapter 7.3.9).

7.3.6 Parameter analysis for MC and DP criteria

The same analyses were made with the cohesive-frictional material models Drucker-Prager (DP) and Mohr-Coulomb (MC). The simulations produced corresponding values for cohesion and the internal friction angle in cases where the material failed only by shearing. Both of these material models are found in ABAQUS, therefore the UMAT subroutine was not needed. The parameter comparison between DP and MC models is exactly valid only in the chosen meridian as defined in Ch. 5. Therefore, they cannot be compared exactly in the general stress analysis, in which the stress state characteristic varies arbitrarily. However, this relation is used in numerical punch test simulations to get a general idea of the correlation between the models.

Analyses with cohesive-frictional models (DP and MC) were made according to ideal plasticity theory without hardening or softening. The results of admissible parameter combinations in different material models are presented in Fig. 7.14.

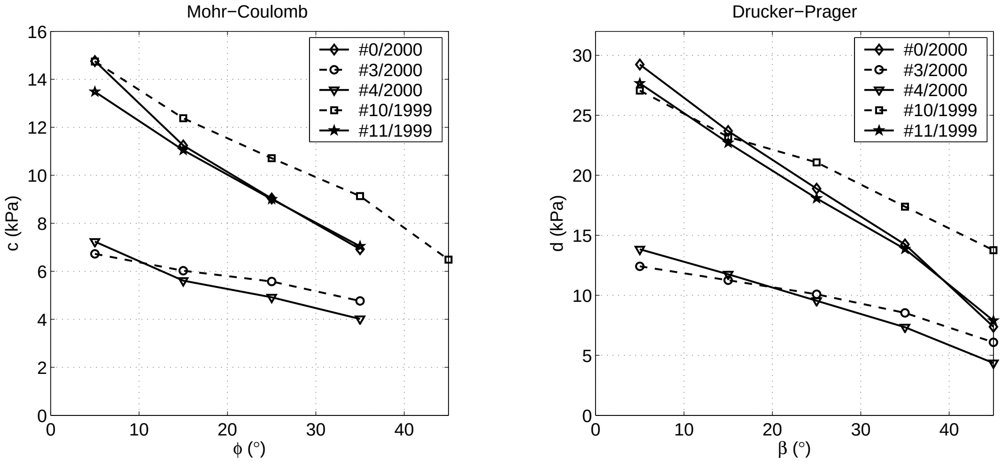

Figure 7.14. Admissible parameter combinations in the Mohr-Coulomb and the Drucker-Prager material models.

The dependency between cohesion and the friction angle is more linear in cohesive-frictional material models than it was in the shear-cap model. However, similar trends with two groups of test cases were observed.

The parameters were adjusted by the relation between MC and DP parameters (Eq. (5.28)) to compare the values in different models (Fig. 7.15). The best agreement was observed by matching the parameters along the shear meridian, because the shear failure was the primary failing mode in the punch test simulation while using the cohesive-frictional material model. Parameters from both cohesive-frictional models are close to each other in all test cases.

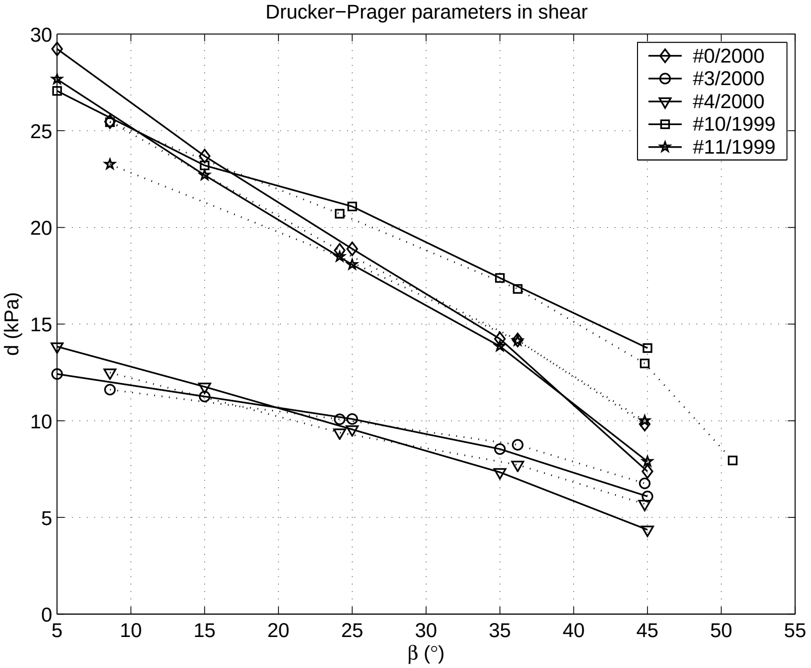

Figure 7.15. Admissible DP parameters matched in the shear meridian for DP (solid line) and MC models (dashed line).

7.3.7 Comparing shear-cap and Drucker-Prager

Before comparing cohesion and friction angles between the shear-cap model and DP model, the corresponding shear-cap parameters were replaced with physical parameters matched according to Eq. (5.31).

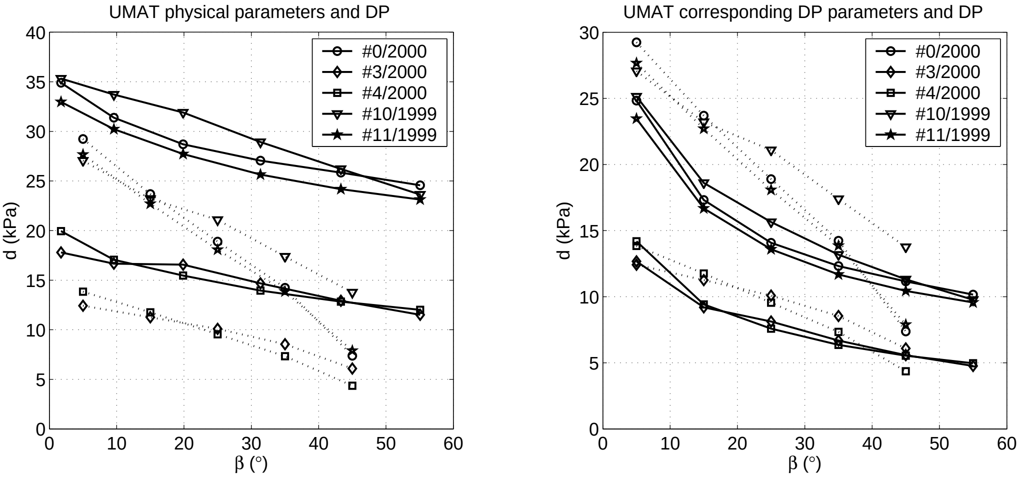

(a) (b)

Figure 7.16. Admissible parameters in the shear-cap model (a) physical parameters (b) corresponding DP parameters. Results from DP model are shown with dashed lines.

Comparing the physical parameters in the shear-cap model with the DP model shows that lower values for cohesion are needed in the DP model (Fig. 7.16a). First, cohesive softening was not included in DP model. Second, the yield surface size in the shear-cap model is always smaller than in the DP model. Yield surfaces coincide only at the point p=0; in all other stress states the shear-cap yield envelope is inside the DP. The difference in cohesion between the models becomes larger the higher the friction angle is, because the cap decreases the yield surface more by comparing with the DP model, in which the frictional strength increases without limit as the hydrostatic pressure increases.

The parameters between the models are generally closer together if corresponding DP parameters are used to describe the shear-cap model (Fig. 7.16b). However, the corresponding cohesion in the shear-cap model is lower in most points than found by the original DP model. Although the shear-cap model evaluates larger shear strength, the cap side limit balances out the difference between the models.

7.3.8 Least square approximation of admissible parameters in the shear-cap model

An exponential function was applied to fit all data from admissible parameter combination curves created by the shear-cap model. Three curves shown in Fig. 7.17, were determined: Lower and upper limits describe the fitting in the selected group of results. The average curve was fitted from all simulated data. The lower limit curve was evaluated by data from cases 3 and 4 in the year 2000, while the upper limit curve corresponds to cases 0/2000, 10/1999 and 11/1999. The region between the lower and upper limit describes the expected parameter combination well. The difference between the selected fit and the fit for all data approximates the expected deviation from the average level.

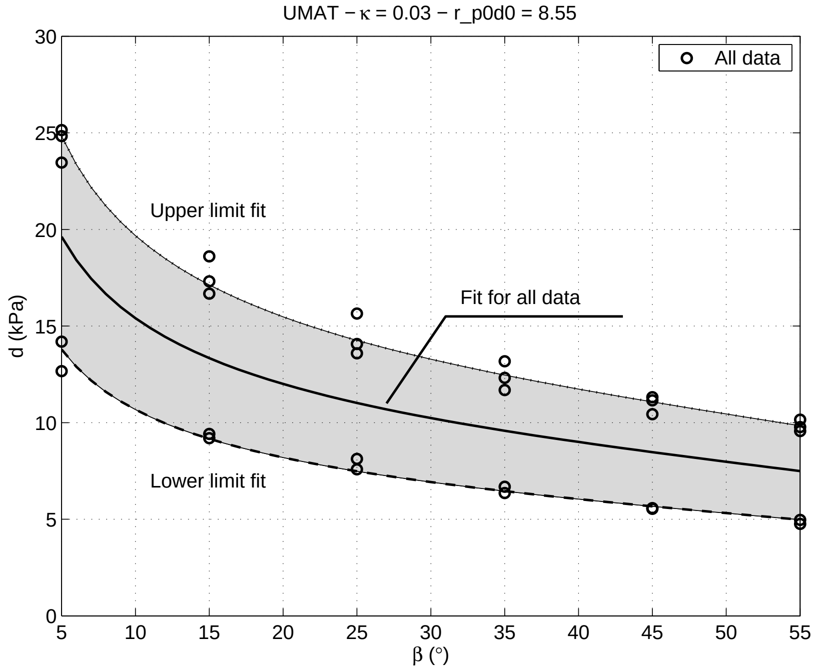

Figure 7.17. Least square approximations for admissible parameter combinations of the corresponding cohesion and the internal friction angle.

A least square fitting was made for a function expressed as

$$d(\beta) = d(45°)\exp(ax)$$
$$x = \ln(\tan\beta) \qquad \textbf{(7.5)}$$

where constants *a* and *d(45 °)* were evaluated by the least square fitting method in the logarithmic scale (Table 7.3). *d(45 °)* describes the cohesion corresponding to the friction angle equal to 45°.

Table 7.3. Parameters describing the exponential approximation for corresponding cohesion in shear-cap model as a function of friction angle.

	a	*d(45 °)* kPa
Fit for all data	-0.3447	8.471
Fit for upper limit	-0.3314	11.07
Fit for lower limit	-0.3647	5.669

7.3.9 Deformations

Rubble deformations, measured both inside and at the bottom of the keel, depend on the failure mode and therefore on the stress state characteristic as described in Chapter 7.3.4.

Comparison between measurements and simulations was made for Test 0/2000. Rubble compaction between the top of the keel and the depth 2.5 m close to the vertical center line is presented in Fig. 7.18 for friction angles from 5° to 55° as a function of the platen displacement. As observed earlier, the friction angle affects the failure mode and therefore the deformations as well. Larger friction provides more compaction. In this case $\beta \approx 20°$ would result in good approximation of the rubble compaction for whole loading period. $\beta = 15°$ predicted the compaction well until the platen displacement was 0.03 m, underestimating the compaction thereafter. $\beta = 25°$ resulted in a slight overestimation of the compaction for whole loading period. Variation of the cohesion did not have any effect.

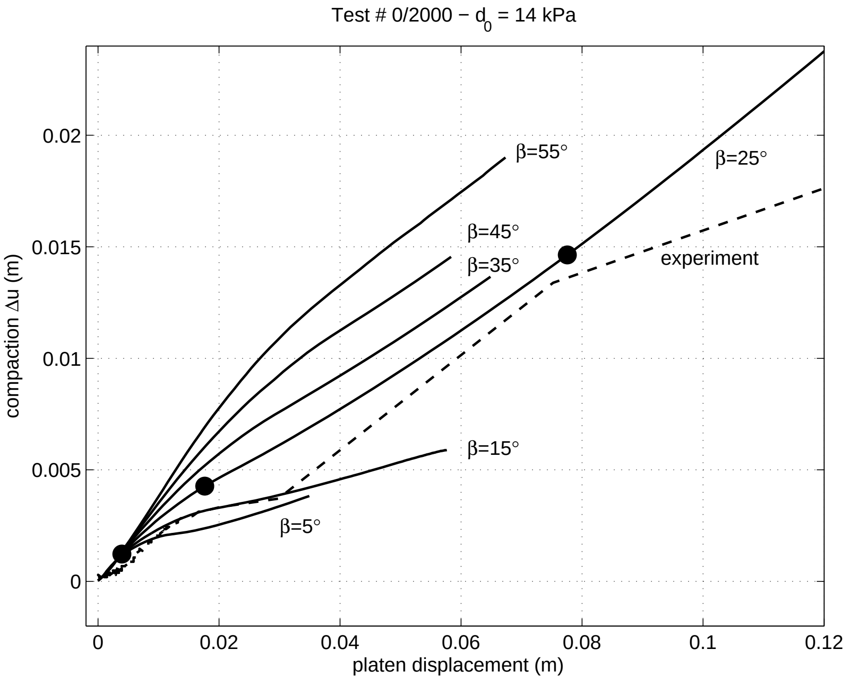

Figure 7.18. Compaction of the rubble versus platen displacement. Dots indicate the different loading phases that have been studied in Ch. 7.3.4.

The displacements at the keel bottom indicated that the simulated deformations were too small in comparison to the measured ones. The major source for this deviation was that the conical shear failure zone when using the shear-cap model, does not spread out sufficiently. The smooth yield envelope results only in slight dilatation during shear failure, if the hydrostatic pressure is positive. To model bottom part displacements accurately, one should modify the yield function in the shear failure region to account for more volumetric expansion. Or one could apply a non-associative flow rule to model the plastic deformations.

7.3.10 Effect of the hardening parameter

The effect of the hardening parameter was studied in cases 10/1999 and 0/2000. Parameter analyses were carried through for Test 0/2000 to ascertain the dependency between the admissible parameter combination (*d* and β) and the hardening parameter κ. One parameter combination was chosen for the Test 10/1999.

It was observed from the load-displacement curves that the hardening parameter affects both the maximum load and the slope in the softening phase. Diminishing the hardening parameter from 0.03 has a strong effect on the maximum load when the friction angle is fixed to 25° as shown in Fig. 7.19. However, the lower value is not reasonable in the average sense, because in that case the keel would soften too steeply in most of the test cases. Also, convergence problems arise in the numerical simulation. The increase of the hardening parameter has a weaker effect. By changing κ from 0.03 to 0.3, the relative force (simulated peak force / measured peak force) increased by 18% in Test 10/1999 and by 5% in 0/2000. Therefore, having a linear connection between the maximum force and cohesion, the corresponding cohesion needs to be smaller if the hardening parameter increases as seen from Fig. 7.20. The choice of a hardening parameter becomes less significant in the case of large friction angles.

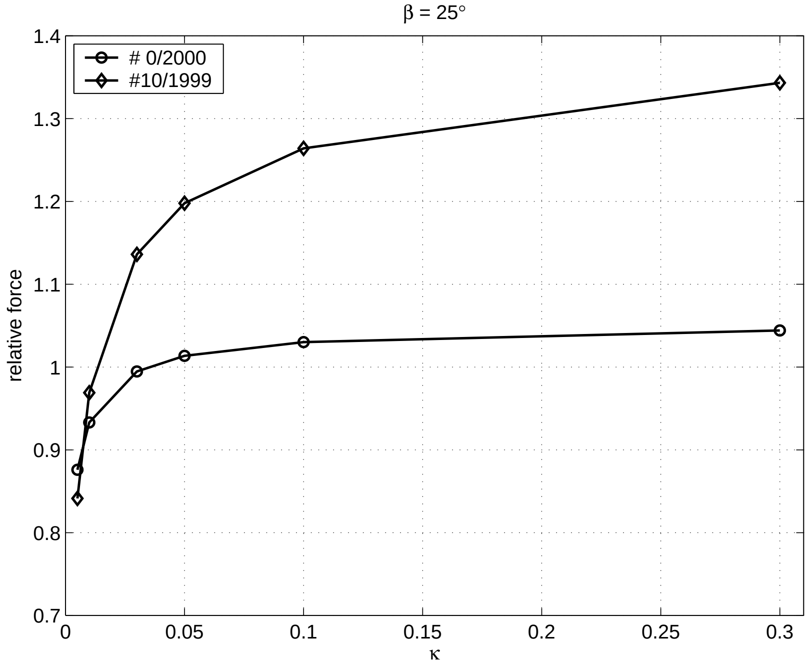

Figure 7.19. Relative force versus hardening parameter in Tests 10/1999 and 0/2000. β=25°.

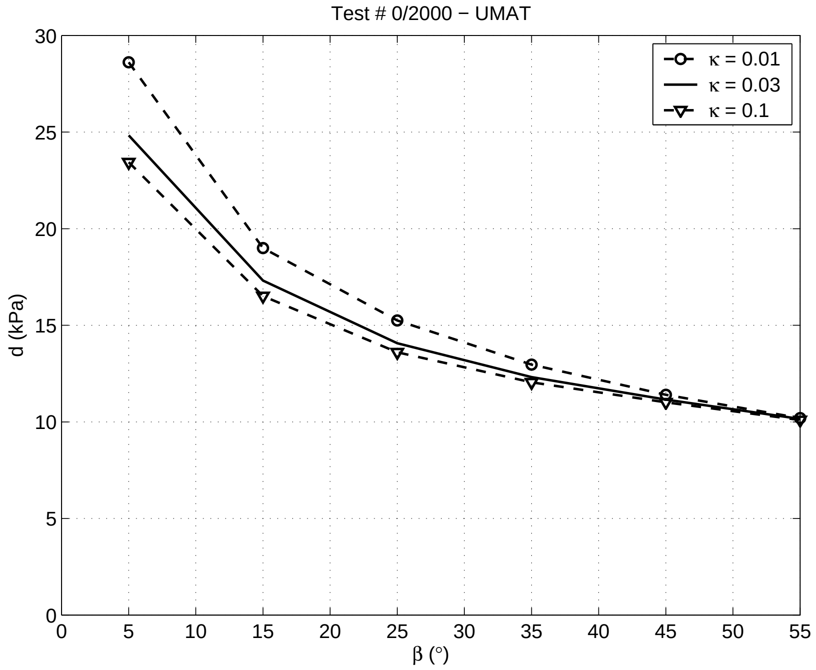

Figure 7.20. Admissible parameter combination dependency on the hardening parameter in Test 0/2000.

7.3.11 Effect of the cap shape parameter

The sensitivity of the cap shape parameter R was studied in case 0/2000. Dependency on the yield surface is shown in Fig. 7.21. The increase of R shrinks the yield surface size, resulting in a lower load capacity because the rubble fails at lower stress states. The choice of R becomes significant when the friction angle increases, as seen from the admissible parameter combination curves in Fig.7.22.

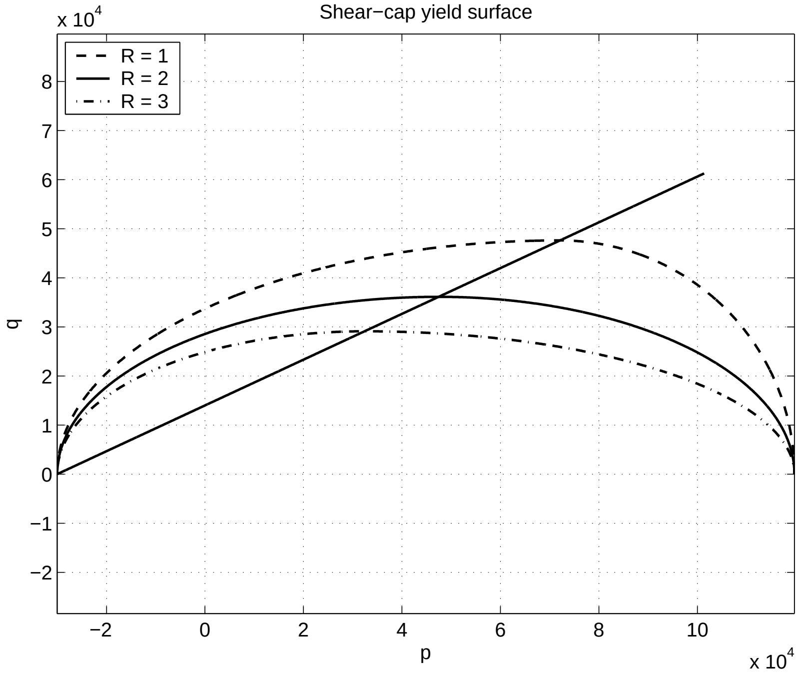

Figure 7.21. Shear-cap yield surface with different values of cap shape parameter R, which varies from 1 to 3.

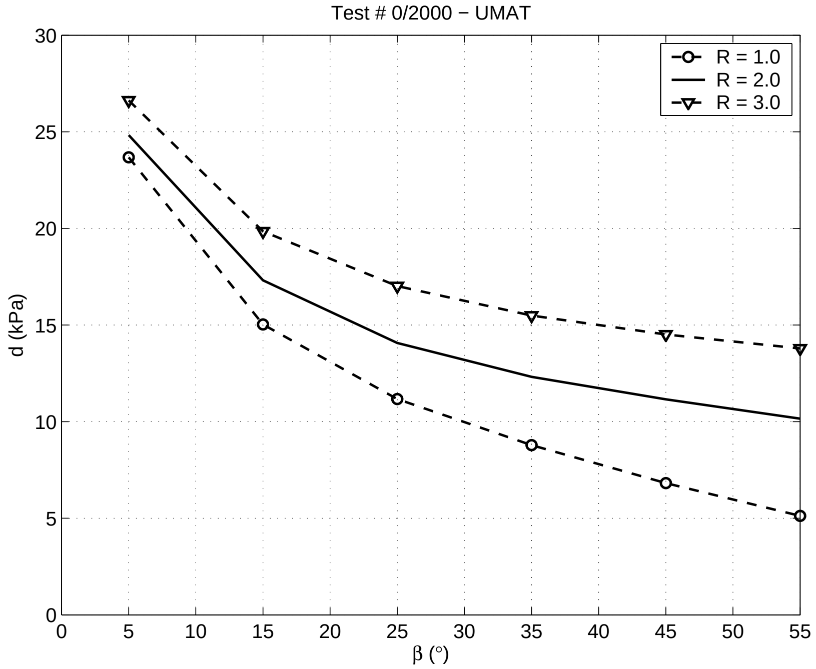

Figure 7.22. Admissible parameter combination dependency on the cap shape parameter (R) in Test 0/2000.

7.3.12 Effect of p_0/d_0 ratio

The sensitivity of the ratio between hydrostatic pressure strength and cohesion (p_0/d_0 ratio) was studied in case 0/2000. Dependency on the yield surface is presented in Fig. 7.23. The increase on the p_0/d_0 ratio expands the yield surface size, resulting in a higher load capacity because the rubble fails at higher stress states. The choice of p_0/d_0 ratio does not depend considerably on the friction angle, as seen from the admissible parameter combination curves in Fig. 7.24.

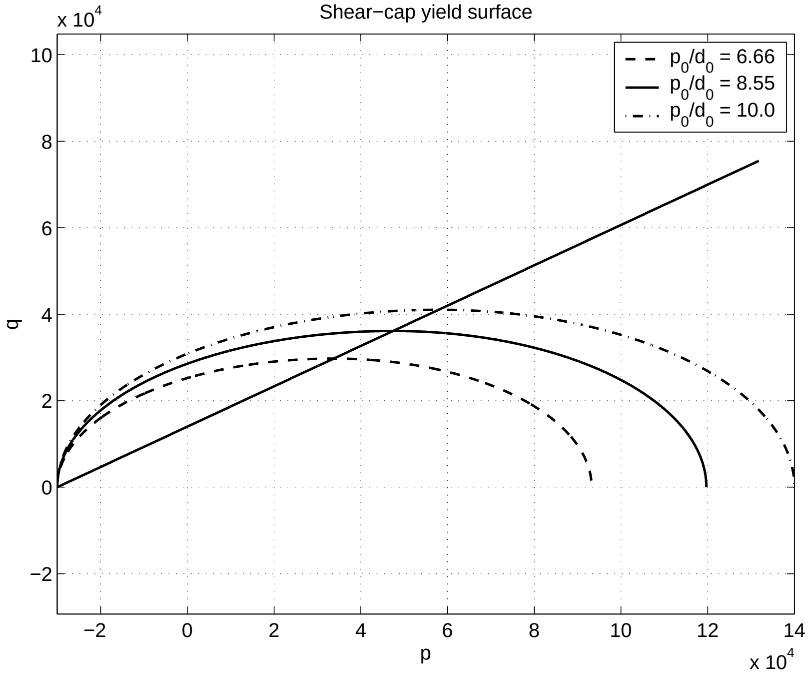

Figure 7.23. Shear-cap yield surface with different values of p_0/d_0 *ratio (6.66, 8.55 and 10.0).*

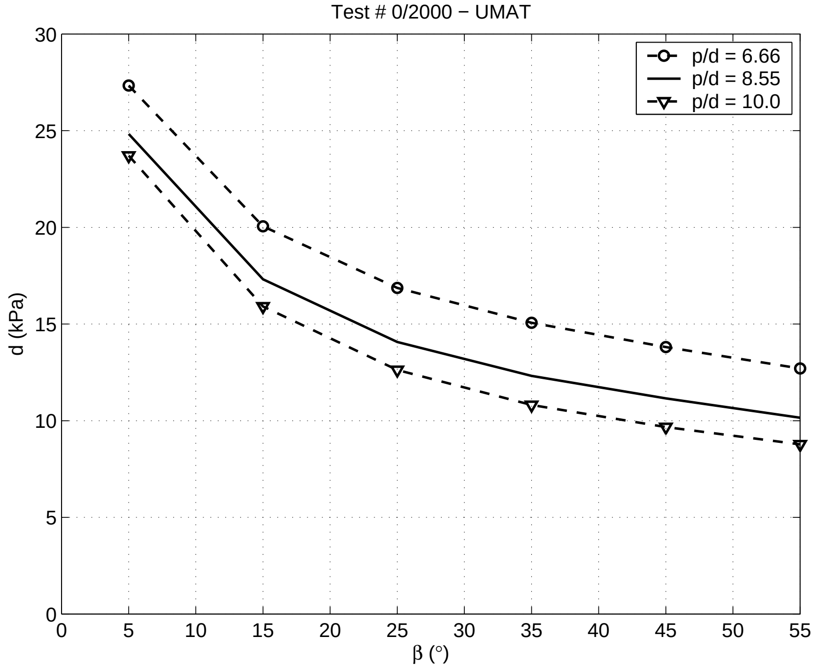

Figure 7.24. Admissible parameter combination dependency on the p_0/d_0 ratio in Test 0/2000.

7.4 Mesh dependency study

Including the strain softening phenomenon into cohesive-frictional material model, the solution depends on the element mesh (both the size and orientation of elements), because large strains accumulate in the localized strain zone (Leroy and Ortiz, 1989).

Mesh dependency studies by applying the shear-cap model were conducted for case 10/1999. Free meshing technology was applied. Therefore, the spatial distribution of nodal points was not exactly the same between each mesh. Table 7.4 shows the relation between the maximum force in a current and coarse mesh. The maximum load decreases only slightly when using the denser mesh. The maximum drop was below 4% when the dof ratio in the current and coarse mesh was 17.4. A greater difference was found in the post peak region.

Table 7.4. Maximum force dependency on the degrees of freedom. F^{c}_{max} *is the maximum force corresponding to the coarse mesh and* F_{max} *corresponds to the finer mesh.* $\Delta F = F^{c}_{max} - F_{max}$.

dof / dof in coarse mesh	F_{max} / F^{c}_{max}	$\Delta F / F^{c}_{max}$
1	1	0.0%
1.6	0.999	0.1%
3.4	0.988	1.2%
6.3	0.982	1.8%
7.3	0.971	2.9%
13.5	0.983	1.7%
17.4	0.962	3.8%

Simulations by the Mohr-Coulomb model indicated a much larger mesh effect than by the shear-cap model, even the MC material model did not undergo any softening behavior (Kjestveit, 1999). Adopting the strain softening behavior into the MC model, the width of the shear band proceeding through the keel becomes narrower, finally creating a conical plug (Heinonen, 2001). As observed in Ch. 7.3.4 the damaged areas in the keel simulated by the shear-cap model are not localized due to large areas failed by compaction.

7.5 Discussion

The calibration of material parameters resulted in good agreement in the load-displacement relationship. Admissible combination of cohesion and the friction angle was evaluated by parametric studies to simulate the measured maximum force correctly. High cohesion results in low internal friction and vice versa. Two different cohesion levels (groups) were observed from the admissible parameter combination curves. The first one contains two and the second one three test cases. Individual test cases in both groups had fairly good agreement of the admissible parameter combinations. Cohesion in the first group (0/2000, 10/1999, 11/1999) was approximately double compared to the second group (3/2000 and 4/2000). A similar trend was observed also in the calibration of the elastic modulus. The difference in ice conditions between 1999 and 2000 explains most of the variation. However, because case 0/2000 belongs to the first group whereas 3 and 4/2000 are in the second group, some variation was found between the test sites. Laboratory tests for the ice samples indicated that the strength in the consolidated layer was higher in 2000 than in 1999 (Heinonen et al., 2000(a) and 2000(b)). However, it was observed by the underwater studies in the field that the underwater rubble was softer in 2000 than in 1999. Some difference was also caused by the geometry approximation due to an axisymmetric assumption with even keel thickness. Without better knowledge of ice conditions, least squares approximation of admissible parameter combination with upper and lower limits could be used in engineering approaches.

The sensitivity of fixed parameters was also studied for one test case to glean information on how the cohesion should be modified if one of the fixed parameters is varied. When the friction angle was low, the variation of the hardening parameter was highest, while that of the cap shape parameter was lowest. Variation of the ratio between the initial hydrostatic pressure strength and cohesion did not depend on the friction angle.

Studies with different element meshes indicated only very slight mesh dependency on the maximum load. The maximum force decreased by less than 4% when the dof ratio in the current and coarse mesh increased to 17.4. A greater difference was observed at the post peak region, but the primary milestone of this study was to predict the maximum load making the post peak response less significant. The post peak region was also less accurately measured due to the dynamic effect of the energy release from steel wire ropes. Therefore, the solutions achieved with a rather coarse mesh (becoming finer under the gap) are within an acceptable range.

Rather high values were evaluated for cohesion with the shear-cap model, and also with the Drucker-Prager and the Mohr-Coulomb models, also by comparison with earlier published data. Some differences result from different analysis methods. Time history analysis in FEM observes the failure progression at each material point independently. Therefore, the global keel failure is not simultaneous.

The initial cohesion is larger than the average cohesion in the global shear failure surface at the peak force, whereas the cohesion at most of the points is smaller due to softening behavior. Also, the separation of different parameters in the pressure-dependent failure condition is undetermined when applying analytical models proposed earlier, for example by Heinonen and Määttänen (2000(c)), Jensen et al. (2000), and Azarnejad and Brown (2001). Because of complicated boundary conditions due to the consolidated layer and the redistribution of stresses during keel failure, the stress state in analytical models is only a rough estimate. The same problems arise in the analysis of previous model tests, which more or less describe only the average shear strength acting on the failure plane.

The dilatation and failure mode depended strongly on the friction angle. Increase of friction resulted in more dilation during shear failure and more compaction during cap failure. Simulated keel bottom deformations were too small in comparison to the measured ones, representing the major lack in the material model. The volumetric expansion during shear failure under hydrostatic compression ($0<p<p_a$) should be larger. That is not achieved by increasing the friction angle as in the case of classical cohesive-frictional models. Although the conical failure mode did not spread outwards far enough, both failure modes were activated successfully in the simulations.

Friction angles up to 35° indicated reasonable force-displacement simulation in the considered region. Deformations inside the keel, compaction, indicated that the friction angle should be between 15° and 25° to agree with the measurements.

Because both deformation modes are usually activated in the rubble, the material undergoes plastic deformation in the larger area than is simulated by the cohesive-frictional model. Therefore, a localized shear deformation zone is not likely in the shear-cap model. The solution with the coarse mesh is reliable. Other error sources arise from the axisymmetric geometry interpretation with even keel thickness. However, with this kind of phenomelogical average model, local differences do not play an important role. The sensitivity of keel dimensions should be studied to define the error arising from incomplete thickness determination.

If the pushdown loading process needs to be simulated further towards larger deformations, the element mesh must be updated to avoid badly distorted elements.

8 Conclusions

8.1 Testing

In-situ full-scale loading tests were conducted in the Northern Gulf of Bothnia in order to measure the ridge keel mechanical properties that are used for developing a material model for ice rubble. A versatile transportable test rig with accessories was designed and manufactured for ridge keel punch shear tests, consolidated layer bending and compression tests, and for consolidated layer sliding on top of the ridge keel tests. Altogether 33 loading tests in full-scale were conducted during five winters from 1998 to 2003, 12 of them punch shear tests. The testing procedure consisted of investigation of the ridge keel internal structure by drilling and underwater video. The consolidated layer thickness, keel depth and porosity were also measured. Ice characterization was made by measuring the ice salinity, density, crystallographic structure and uniaxial compressive strength. In all ridge loading tests the consolidated layer was cut free from the surrounding solid ice field to allow well-defined boundary conditions. In the punch shear tests, the deformations both inside and at the bottom of the keel were measured during the test in order to locate the failure surface in the keel.

This work was focused on analyzing the punch tests thoroughly to develop a constitutive model for rubble in the keel. Further studies are needed to analyze other test types.

Maximum loads in punch shear tests varied from 74 kN to 1.1 MN. The diameter of the platen varied between 2.5 and 4.7 m. The average keel depth varied from 3.0 to 6.4 m while the corresponding effective thickness of rubble under the platen varied from 2.2 to 5.0 m. The average keel porosity varied from 27% to 42%, but the corresponding porosity of the rubble was higher: from 31% to 46%. A rough estimate of the keel shear strength was made by assuming a cylindrical shear failure surface through the keel. The average of all tests was 14 kPa but a rather large variation was found between different years. Some contribution from the consolidated layer due to an improper cut increased the maximum load in some cases.

Most of the tests were successful. The pushing plate penetrated straight into the underlying rubble without significant tilting and the keel usually broke during the first trial. Some problems arose when measuring the keel displacements at the bottom and inside the rubble due to difficult fixing of the sensor or due to freezing of floating pipes. All time-history measurements of force were successful, resulting in a similar type of load pattern. However, in some displacement measurements it was impossible to interpret whether the result should be considered as individual ice block movement or as continuous rubble deformation.

8.2 Numerical simulations

An ice rubble continuum material model was developed for three-dimensional Finite Element Analysis. To decrease computation times, an axisymmetric model was applied for the punch test simulations. A commercial Finite Element code, ABAQUS/Standard, was applied in which the material model was implemented as a user material subroutine (UMAT). The constitutive law was written in a similar form to that used in the plasticity theory based on the strain decomposition into elastic and plastic parts. The shear-cap yield surface with evolution laws both for cap hardening and for cohesive softening represent both the compaction and shear failure phenomena. The pressure-dependent yield function was applied with the associative flow rule.

Originally the shear-cap model needs nine parameters, but using small-scale laboratory data and some approximations, the number can be simplified to three. One of them describes the elastic behavior (elastic modulus); the other two describe the plastic behavior (cohesion and friction). Despite these approximations, the model still represents the deformation and failure modes measured in full-scale, resulting in admissible parameter combinations for cohesion and the friction angle. Because some parameters like the relation between initial pressure strength and cohesion, were evaluated according to small-scale measurements, the validity in full-scale application is uncertain. Due to uncertain evaluation of some of the fixed parameters, parametric analyses were performed to determine the sensitivity of each parameter.

Good agreement in the load-displacement relationship was achieved by calibrating the material parameters. The admissible combination of cohesion and the friction angle was evaluated by parametric studies to simulate the measured maximum force correctly. The simulation of a post peak region was less important due to the inaccuracy of measurement caused by the dynamic energy release from steel wire ropes. High cohesion resulted in low internal friction and vice versa. An exponential function approximating the admissible parameter combination in the shear-cap model was evaluated according to the method of least square sums. An average level together with a lower and upper limit was also determined.

All tested material models resulted in high values for initial cohesion compared with earlier published small-scale data. Some differences arise due to the different analysis method. Time history analysis in FEM observes the failure progression in each material point independently. Therefore, global keel failure is not simultaneous. The initial cohesion is larger than the average cohesion in the global shear failure surface at the peak force, whereas cohesion is smaller due to the softening behavior.

The friction angle had major effect on dilatation and the failure mode. Increase of friction resulted in more dilatation during shear failure and more compaction during cap failure. Because simulated keel bottom deformations were too small compared to measured ones, the flow rule needs to be further developed to increase the dilatation in the shear failure part (in the hydrostatic pressure region between zero and p_a). Also, the conical failure mode did not spread outwards far enough in the simulations. However, both failure modes, shearing and compaction, were activated in the simulations.

Cohesive-frictional material models like Drucker-Prager and Mohr-Coulomb describe only the shearing failure with volumetric expansion. If rubble undergoes loading which causes confinement, the presence of hydrostatic pressure increases the material strength without any limit, although the material fails by shearing. For example, in ridge-structure interaction, a lot of rubble accumulates in front of the structure, causing a high degree of confinement. If the strength is not limited on the pressure side, the ridge load will be strongly overestimated. Also, the deformation field is unrealistic due to lack of compaction failure in the model.

8.3 Further development needs

The numerical convergence was admissible, both in static and dynamic simulations, which makes the numerical model applicable in three-dimensional analysis to predict the ridge loads against structures. Due to large deformations, the element mesh must be updated to avoid badly distorted elements. Admissible parameter combinations evaluated by the model calibration could be applied to determine the reasonable ridge load level.

The developed numerical procedure can be applied to validate simpler models needed in the statistical approach, because FE computation needs too much time. Also, a neural network application could be "taught" by the FE procedure.

To model the bottom part displacements accurately, one should modify the yield function in the shear failure region to account for more volumetric expansion. That could also be achieved with a non-associative flow rule. The latter one results in the unsymmetric stiffness matrix increasing computation time. Therefore, during further studies the balance between dilatation and compaction should be established. Adjustment of the deformation field would result in more accurate evaluation of the friction angle. Before that the admissible parameter combinations could be used as input values in simpler ridge load algorithms or in statistical approaches.

The spatial dependency on material parameters, especially in the vertical direction should be studied more closely both by experiments and simulations. For instance, Määttänen (1999) presented a model in which cohesion decreases in the vertical direction linearly from a top value at the consolidated layer bottom to zero at the keel bottom. The upper part is treated as partially consolidated rubble having higher cohesive strength than in the keel bottom.

The loading test was planned to provide a rather high strain rate in the rubble to avoid time-dependent deformation mechanisms. To expand the feasibility of the model, the time-dependent strain component should be added to the total strain. In that case, the dynamic simulation in the loading test could contain also the loading rig with steel wire ropes modeled by mass and stiffness.

Ridge-structure interaction simulation needs the consolidated layer bending strength which needs to be analyzed from consolidated layer beam bending tests on the underlying rubble. The simulation needs a 3D model in which parametric studies are needed to define the foundation support resulting from the underlying rubble. Horizontal compression and shearing tests on top of the rubble should also be analyzed more closely for ridge/structure interaction simulations.

References

ABAQUS Theory Manual, 2001, ver. 6.1, Hibbit, Karlsson & Sorensen, Inc.

ABAQUS/Standard User's Manual, 2001, ver. 6.2, Hibbit, Karlsson & Sorensen, Inc.

Azarnejad, A. and Brown, T.G. 2001. Ice rubble behavior in punch tests. Journal of Cold Regions Engineering, Vol. 15, No. 3, September 2001, pp. 135-153

Beltaos, S. 2002. Collapse of floating ice covers under vertical loads: test data vs. theory, Cold Regions Science and Technology 34(2002), 191-207

Belytschko, T., Liu, W.K. and Moran, B. 2000. Nonlinear finite elements for continua and structures, Chichester : Wiley, 650 p., ISBN: 0-471-98773-5

Bruneau S.E., Crocker G.B., McKenna R.F., Croasdale K.R., Metge M., Ritch R. and Weaver J.S. 1998. Development of Techniques for Measuring in situ Ice Rubble Shear Strength, Ice in Surface Waters, Vol. 2, Proc. of the 14th International Symposium on Ice (IAHR), Potsdam, USA, pp. 1001-1007.

Croasdale, K.R. 1980. Ice Forces on Fixed Rigid Structures, 1st IAHR State-of-the-Art Report on Ice Forces on Structures, pp 34-106, CRREL Special Report 80-26, Hanover, N.H., USA.

Croasdale, K.R. and Cammaert, A.B. 1993. An Improved Method for the Calculation of Ice Loads on Sloping Structures in First-Year Ice. First International Conference on Exploration of Russian Arctic Offshore, pp. 161-168, St. Petersburg, Russia.

Croasdale, K.R., Cammaert, A.B. and Metge, M. 1994. A Method for the Calculation of Sheet Ice Loads on Sloping Structures. Proceedings of the IAHR'94 Symposium on Ice, Vol. 2, pp 874-875, Trondheim, Norway.

Croasdale & Associates Ltd. 1997. In Situ Ridge Strength Measurements, Local & Global 1998, Proposal for a Joint Industry-Government Project, 24 p.

Ettema, R. and Urroz, G.E. 1989. On Internal Friction and Cohesion in Unconsolidated Ice Rubble, Cold Regions Science and Technology, 16(1989), pp. 237-247.

Dolgopolov, Y.V., Afanasev, V.A., Korenkov, V.A. and Panfilov, D.F. 1975. Effect of Hummocked Ice on Piers of Marine Hydraulic Structures, Proceedings IAHR Symposium on Ice, pp. 469-478, Hanover, NH, U.S.A.

Harr, M.E., Mechanics of Particulate Media, 1977. Mc-Graw-Hill Inc. USA, 543 p.

Heinonen, J. 1999. Simulating Ridge Keel Failure by Finite Element Method, The 15th International Conference on Port and Ocean Engineering under Arctic Conditions (POAC), Helsinki, Finland, vol 3, pp. 956-963.

Heinonen, J., Määttänen, M., Høyland, K.V. and Kjestveit, G. 2000(a). Ridge Loading Experiments, Field Experiments in Winter 1999, LOLEIF Progress Report 4, 73 p.

Heinonen, J. and Määttänen, M. 2000(b). Ridge Loading Experiments, Field Experiments in Winter 2000, LOLEIF Progress Report 10, 40 p.

Heinonen, J. and Määttänen, M. 2000(c). LOLEIF Ridge-Loading Experiments - Analysis of Rubble Strength in Ridge Keel Punch Test, Proc. of the 15th International Symposium on Ice (IAHR), Gdansk, Poland, pp. 63-72.

Heinonen J. 2001. Ridge Keel Material Model - Testing and Analysis, Thesis submitted in partial fulfilment of the requirements for the degree of Licentiate of Science in Technology, Espoo, 96 p.

Heinonen, J., Järvenpää, I., Määttänen, M. and Mantere, H. 2004. Ridge Keel Mechanical Properties - Testing, Field Experiments in Winter 2003, STRICE Deliverable No. D-5.4.1, 38 p.

Hoikkanen, J. 1984. Measurements and Analysis of Ice Pressure against a Structure in Level Ice and in Pressure Ridges. Proceedings of the 7 th International IAHR Symposium on Ice, Vol. 3, pp.151-160, Hamburg, Germany.

Hopkins, M.A., Tuhkuri J. and Lensu M. 1999. Rafting and ridging of thin ice sheets, Journal of Geophysical Research, Vol. 104, No. C6, pp. 13605-13613, June 15.

Hughes, T.J.R., and Winget, J. 1980. Finite Rotation Effects in Numerical Integration of Rate Constitutive Equations Arising in Large Deformation Analysis, International Journal for Numerical Methods in Engineering, vol.15, pp. 1862-1867.

Høyland, K.V., Kjestveit, G., Heinonen, J. and Määttänen, M. 2000. LOLEIF Ridge Experiments at Marjaniemi; The Size and Strength of the Consolidated Layer, Proc. of the 15th International Symposium on Ice (IAHR), Gdansk, Poland, pp. 45-52.

Høyland, K.V. 2002. The consolidation of first-year sea ice ridges, Journal of Geophysical Research, Vol. 107, No. C6.

Jensen, A., Høyland, K.V. and Evers, K.-U. 2000. Scaling and Measurement of Ice Rubble Properties in Laboratory Tests, Proc. of the 15th International Symposium on Ice (IAHR), Gdansk, Poland, pp. 105-112.

Jensen, A. , Løset, S., Høyland, K.V., Liferov, P., Heinonen, J. and Evers, K.-U. 2001. Physical Modelling of First-Year Ice Ridges - Part II: Mechanical Properties, The 16th International Conference on Port and Ocean Engineering under Arctic Conditions (POAC), Ottawa, Canada, pp. 1493-1502.

Kankaanpää P. 1998. Distribution, morphology and structure of sea ice pressure ridges in the Baltic Sea, Department of Geography, University of Helsinki, Fennia, Helsinki, Doctoral thesis, 101 p.

Kjestveit, G. 1999. Investigation of Mechanical Properties of Ice Ridges, Norwegian University of Science and Technology, Department of Structural Engineering, Master Thesis, 46 p.

Krankkala, T. and Määttänen, M. 1984. Methods for Determining Ice Forces Due to First- and Multi-Year Ridges. Proceedings IAHR Ice Symposium, Vol. IV, pp. 263-287, Hamburg, Germany.

Kuhl, E., D'Addetta, G.A., Herrmann, H.J. and Ramm, E. 2000. A Comparison of Discrete Granular Material Models with Continuous Microplane Formulations, Granular Matter 2, pp. 113-121, Springer-Verlag.

Kärnä, T. (Ed.) 1997. Choice of Offshore Structures for Arctic Regions (COSAR), Final report, VTT Building Technology, Report RTE38-IR-4/1997, 188 p.

Kärnä T., Rim C.W. and Shkhinek, K.N. 2001. Global Loads Due to First-Year Ice Ridges, The 16th International Conference on Port and Ocean Engineering under Arctic Conditions (POAC), Ottawa, Canada, pp. 627-638.

Lemee, E. and Brown, T. 2002. Small-scale Plane Strain Punch Tests, Proc. of the 16th International Symposium on Ice (IAHR), Dunedin, New Zealand, pp. 1-7.

Leppäranta, M. and Hakala, R. 1989. Field Measurements of the Structure and Strength of First-year Ice Ridges in the Baltic Sea, 8th International Conference on Offshore Mechanics and Arctic Engineering, Vol 4, pp. 169-174.

Leppäranta, M. and Hakala, R. 1992. The Structure and Strength of First-year Ice Ridges in the Baltic Sea, Cold Regions Science and Technology, 20(1992), pp. 295-311.

Leroy Y. and Ortiz M. 1989. Finite Element Analysis of Strain Localization in Frictional Materials, Numerical and Analytical Methods in Geomechanics, 13(1), pp. 53-74.

Lewis R.W. and Schrefler B.A. 1998. The Finite Element Method in the Static and Dynamic Deformation and Consolidation of Porous Media. J.Wiley & Sons Ltd, 2nd ed., ISBN 0-471-92809-7.

Løset, S. 1993. Discrete Element modelling of Forces Exerted on a Boom for Ice Management, Proceedings of the Third International Offshore and Polar Engineering Conference, Singapore, pp. 742-746.

Mellor, M. 1980. Ship Resistance in Thick Brash Ice. Cold Regions Science and Technology, Vol. 3, No. 4, pp. 305-321.

Määttänen, M. 1999. Discussion in Helsinki University of Technology.

NAFEMS, 1992. Introduction to Nonlinear Finite Element Analysis, Ed. By E. Hinton, Bell and Bain Ltd. Glasgow, 380 p., ISBN 1 874376 00 X.

Prodanovic, A. 1979. Model Tests of Ice Rubble Strength, Proc. of the Fifth International Conference on Port Ocean Engineering Under Arctic Conditions (POAC), Trondheim, Norway, Vol 1, pp. 89-105.

Prodanovic, A. 1981. Upper Bounds of Ridge Pressure on Structures. Proceedings POAC '81, Vol. III, pp. 1288-1302, Quebec City, P.Q., Canada.

Rogachko, S., Evdokimov, G., Melnikov, M., Kärnä, T. and Lehmus, E. 1997. The Influence of Porosity on Mechanical Strength of Hummocks, Proc. 16th Int. Conf. Offshore Mechanics and Arctic Engineering (OMAE´97&POAC´97). Yokohama, April 13-18, 1997, Vol IV, pp. 151-157.

Rogachko S.I. and Kärnä T. 1999. Experiments on the Strength of Refrozen Layers of First-Year Ice Ridges, The 15th International Conference on Port and Ocean Engineering under Arctic Conditions (POAC), Helsinki, Finland, Vol 3, pp. 1066-1075.

Runesson K. 1999. Constitutive Theory and Computational Technique for Dissipative Materials with Emphasis on Plasticity, Viscoplasticity and Damage, Part 2. Models and algorithms for geometrically linear theory, Chalmers Solid Mechanics, Publication U76, 246 p., ISSN 0349-8123.

Sanderson T.J.O. 1988. Ice Mechanics, Risks to Offshore Structures, BP Petroleum Development Ltd, London, Graham and Trotman Limited, London, p. 253.

Sayed, M., Timco, G.W. and Sun, L. 1992. Testing Model Ice Rubble under Proportional Strains, OMAE, Vol. 4, Arctic Technology, 1992, pp. 335-341.

Simo J.C. and Hughes T.J.R. 1998. Computational Inelasticity, Springer-Verlag, New York, 392 p., ISBN 0-387-97520-9.

Sinha, N.K. 1979. Grain boundary sliding in polycrystalline materials, Philosophical Magazine A, Vol. 40, No. 6, pp. 825-842.

Smirnov, V., Sheikin, I.B., Shushlebin, A., Kharitonov, V., Croasdale, K. R., Metge, M., Ritch, R., Polomoshnov, A., Surkov, G., Wang, A., Beketsky, S., and Weaver, J.S. 1999. Large Scale Strength Measurements of Ice Ridges: Sakhalin 1998, RAO Conference, St. Petersburg.

Timco, G.W. and Burden, R.P. 1997. An analysis of the shapes of sea ice ridges. Cold Regions Science and Technology, Vol. 25(1997), pp. 65-77.

Timco, G.W., Frederking, R., Kamesaki, K. and Tada, H. 1999. Comparison of Ice Load Calculation Algorithms for First-year Ridges, Proceedings International Workshop on Rational Evaluation of Ice Forces on Structures, REIFS99, pp 88-102, Mombetsu, Japan, February 2-4, 1999.

Timco, G.W., Croasdale, K. and Wright, B. 2000. An Overview of First-Year Sea Ice Ridges, Technical Report HYD-TR-047, PERD/CHC Report 5-112, August 2000, 157 p.

Tuhkuri J., Lensu M. and Saarinen S. 1999. Laboratory and Field Studies on the Mechanics of Ice Ridge Formation, The 15th International Conference on Port and Ocean Engineering under Arctic Conditions (POAC), Helsinki, Finland, Vol 3, pp. 1118-1129.

Weiss, R.T., Prodanovic, A. and Wood, K.N. 1981. Determination of Ice Rubble Shear Properties, Proc. of the International Symposium on Ice (IAHR), Quebec, Canada, Vol 2, pp. 860-872.

Wong, T.T., Morgenstern, N.R. and Sego, D.C. 1990. A Constitutive Model for Broken Ice, Cold Regions Science and Technology, 17(1990) 241-252.

Wright B. and Timco, G.W. 2001. First-Year ridge interaction with the Molikpaq in the Beaufort Sea, Cold Regions Science and Technology, 32(2001) 27-44.

Yasunaga, Y., Kioka, S., Matsuo, Y. and Saeki, H. 2001. Tests on Strength of Consolidated Parts of Consolidated Parts of Hummock Ice Model, The 16th International Conference on Port and Ocean Engineering under Arctic Conditions (POAC), Ottawa, Canada, pp. 1503 - 1511.

Yasunaga, Y., Kioka, S., Matsuo, Y. and Furuya, A. 2002. The Strength of the Unconsolidated Layer Model of Ice Ridge, Proc. of the 16th International Symposium on Ice (IAHR), Dunedin, New Zealand, pp. 62- 68.

Published by

Series title, number and report code of publication

VTT Publications 536
VTT–PUBS–536

Author(s)
Heinonen, Jaakko

Title

Constitutive Modeling of Ice Rubble in First-Year Ridge Keel

Abstract

In-situ full scale loading tests were conducted in the Northern Gulf of Bothnia in order to measure the ridge keel mechanical properties. Altogether 33 loading tests in full scale were conducted during five winters (1998-2003). 12 of them were punch shear tests, in which a circular plate of the consolidated layer was punched downwards to break the rubble underneath. In all ridge loading tests, the sail was first removed and the consolidated layer was cut free from the surrounding solid ice field to allow well defined boundary conditions. Maximum loads in the punch shear tests varied from 74 kN to 1.1 MN. The diameter of the platen varied between 2.5 and 4.7 m. The average keel depth varied from 3.0 to 6.4 m while the corresponding effective thickness of rubble under the platen varied from 2.2 to 5.0 m.

A continuum material model for ice rubble was developed and implemented into commercial finite element software ABAQUS/Standard. The constitutive law was written in similar form to that used in the plasticity theory based on the strain decomposition into elastic and plastic parts. The shear cap yield surface with evolution laws both for cap hardening and cohesive softening describe also the compaction phenomenon in addition to shear failure.

An axisymmetric finite element model was created to simulate punch shear tests. Time history analysis in finite element method observes progressive failure through the keel occurring non-simultaneous global keel failure. Good agreement in the load-displacement relationship was achieved by calibrating the material parameters to fit the full-scale measurements. The admissible combination of cohesion and the friction angle was evaluated by parametric studies to simulate the measured maximum force correctly. The failure progression in the keel and the relation between the failure modes (compaction and shear) depended strongly on the friction angle. Increased friction resulted in more dilatation at the region of shear failure and more compaction at the region of cap failure. Due to the volumetric expansion during shear failure, a slightly inclined shear failure zone created finally a conical plug punched through the keel.

Keywords
sea ice, ice ridges, ice rubbles, ridge keels, loading tests, punch shear tests, modeling, material models

Activity unit
VTT Building and Transport, Kemistintie 3, P.O.Box 1805, FIN–02044 VTT, Finland

ISBN	Project number
951–38–6390–5 (soft back ed.) 951–38–6391–3 (URL:http://www.inf.vtt.fi/pdf/)	

Date	Language	Pages	Price
June 2004	English	142 p.	C

Name of project	Commissioned by

Series title and ISSN	Sold by
VTT Publications 1235–0621 (soft back ed.) 1455–0849 (URL: http://www.vtt.fi/inf/pdf/)	VTT Information Service P.O.Box 2000, FIN–02044 VTT, Finland Phone internat. +358 9 456 4404 Fax +358 9 456 4374

In-situ full-scale loading tests were conducted in the Northern Gulf of Bothnia in order to measure the ridge keel mechanical properties. In punch shear tests, a circular plate of the consolidated layer was punched downwards to break the rubble underneath. The sail was first removed and the consolidated layer was cut free from the surrounding solid ice field.

A continuum material model for ice rubble was developed and implemented into finite element software ABAQUS/Standard. The constitutive law was based on the strain decomposition into elastic and plastic parts. The shear-cap yield surface with evolution laws for cap hardening and cohesive softening describe both the compaction and shear failure phenomenon.

Time history analysis of punch shear tests in finite element method observes progressive failure through the keel occurring non-simultaneous global keel failure. The admissible combination of cohesion and the friction angle was evaluated by parametric studies to simulate the measured maximum force correctly. The failure progression in the keel and the relation between the failure modes (compaction and shear) depended strongly on the friction angle.

The developed material model can be applied in a three-dimensional finite element simulation of a ridge-structure interaction by applying true geometry for both the ridge and the structure.

Tätä julkaisua myy	Denna publikation säljs av	This publication is available from
VTT TIETOPALVELU PL 2000 02044 VTT Puh. (09) 456 4404 Faksi (09) 456 4374	VTT INFORMATIONSTJÄNST PB 2000 02044 VTT Tel. (09) 456 4404 Fax (09) 456 4374	VTT INFORMATION SERVICE P.O.Box 2000 FIN–02044 VTT, Finland Phone internat. +358 9 456 4404 Fax +358 9 456 4374

ISBN 951–38–6390–5 (soft back ed.)
ISSN 1235–0621 (soft back ed.)

ISBN 951–38–6391–3 (URL: http://www.vtt.fi/inf/pdf/)
ISSN 1455–0849 (URL: http://www.vtt.fi/inf/pdf/)